

**INVESTIGATION OF OZONE INITIATED ETHYLENE
OXIDATION AT ROOM TEMPERATURE:
CHEMISTRY AND FLAME DYNAMICS**

A Dissertation
Presented to
The Academic Faculty

by

Bin Wu

In Partial Fulfillment
of the Requirements for the Degree
Doctor of Philosophy in the
School of Aerospace Engineering

Georgia Institute of Technology
December 2021

Copyright © 2021 by Bin Wu

**INVESTIGATION OF OZONE INITIATED ETHYLENE
OXIDATION AT ROOM TEMPERATURE:
CHEMISTRY AND FLAME DYNAMICS**

Approved by:

Dr. Wenting Sun, Advisor
School of Aerospace Engineering
Georgia Institute of Technology

Dr. Ellen Yi Chen Mazumdar
School of Mechanical Engineering
Georgia Institute of Technology

Dr. Jechiel Jagoda
School of Aerospace Engineering
Georgia Institute of Technology

Dr. Adam Steinberg
School of Aerospace Engineering
Georgia Institute of Technology

Dr. Lakshmi N Sankar
School of Aerospace Engineering
Georgia Institute of Technology

Dr. Timothy Ombrello
Aerospace Systems Directorate
Air Force Research Laboratory

Date Approved: August 20, 2021

To my wife, my parents, and my friends.

“I have fought the good fight, I have finished the race, I have kept the faith.”

2 Timothy 4:7

ACKNOWLEDGEMENTS

When I look back, this is indeed a long and hard journey, but full of blessing, grace, and joy. First of all, I would like to express my sincere gratitude to my teacher and advisor, Prof. Wenting Sun, who offered me the opportunity to start this Ph.D. program in Fall 2016, and then introduced me to the interesting ozone assisted combustion. I am truly thankful to his guidance and patience especially at the beginning of my research, and his continuous support to allow me to explore many possibilities. The time is not easy after 2018 from which I could not go back to Atlanta due to force majeure, but Prof. Sun never gives me up and always believes I could return. His insistence is one of the major reasons I could finally finish this program at Georgia Tech.

I would also like to appreciate Prof. Lakshmi Sankar, who was my academic advisor during Master's program since 2015. He allowed me to take the tough but beneficial Qualifying Examination at AE and also rendered me the freedom to pursue my own interest after passing the exam. I will never forget his kindness and generosity to me all the time. Thanks to my thesis committee members, Prof. Jagoda, Prof. Mazumdar, Prof. Steinberg, and Dr. Ombrello, who is a great co-author to our group for a long time. Thank them for their time and help to me to improve the quality of this dissertation.

Thanks to my labmates and friends, Michael Barnett, Anant Girdhar, Martin Morrow, Zefang Liu, Jinhoon Choe, Dr. Miad Karimi and Dr. Chong Zhou, for the memorable conversations and times at Georgia Tech. It is my great honor to know them and be friend with them all. Special thanks to Dr. Xiang Gao, who kindly helped, guided, and taught me when I first entered the lab. I did learn a lot from him.

To my wife, Chenyu, and my parents, this journey could never be finished without their steadfast love and faith, which supported and will always support me through any difficulty. I am also grateful to my dear roommates as well as my brothers, Dr. Yixing Li and Mengzhen Chen (who will soon receive his doctorate), for the precious memories of daily life in Atlanta and also the generous helps they gave to Chenyu when I could not be there for nearly two years. My deep gratitude to my brother and sister, Jason Yu Chen, and Jasmine Weili Shi, for their endless encouragements, loves and prayers. I am so blessed to meet them and know them at the place far away from home.

Last but not least, may the glory be to the Lord my God. “Surely goodness and mercy shall follow me all the days of my life, and I shall dwell in the house of the Lord forever.” – Psalm 23:6.

TABLE OF CONTENTS

ACKNOWLEDGEMENTS	iv
LIST OF TABLES	ix
LIST OF FIGURES	xi
LIST OF SYMBOLS AND ABBREVIATIONS	xviii
SUMMARY	xix
CHAPTER 1. Introduction	1
1.1 Background and Motivation	1
1.2 Problem Statements	5
1.3 Objectives	6
1.4 Dissertation Outline	8
CHAPTER 2. State-of-the-Art of Ethylene Ozonolysis Chemistry	9
2.1 General Mechanism of Ozonolysis Reaction	9
2.2 C ₂ H ₄ Ozonolysis Reaction with Advanced Approaches	11
2.2.1 Primary Ozonide (POZ)	13
2.2.2 Criegee Intermediate (CI)	14
2.2.3 Secondary Ozonide (SOZ)	19
2.3 Latest Outreach to Ozone Initiated Low-Temperature Oxidation of C ₂ H ₄	20
2.4 Effect of Ozone Addition on Flame Speed	22
2.4.1 Saturated Fuels	22
2.4.2 Unsaturated Fuels	26
CHAPTER 3. Experimental Approaches	31
3.1 Overview	31
3.2 Fast-Mixing Flow Reactor System	32
3.2.1 Early Reactor Design (before 2018)	32
3.2.2 Mixing Optimization	36
3.2.3 Latest Reactor Design (after 2018)	39
3.2.4 Brief Notes on Designed Flow Reactor Systems	45
3.3 Gas Chromatography	46
3.4 UV LED Absorption Measurement	49
3.4.1 Introduction and Set-up	49
3.4.2 System Calibration	53
3.5 Synchrotron Radiative Photoionization Molecular Beam Mass Spectrometry (SRPI-MBMS)	56
3.6 Laminar Jet Flame Burner	59

CHAPTER 4. Measurement of Global Reaction Rate Constant Between Ethylene and Ozone at Ambient Conditions	62
4.1 Pseudo 1 st Order Kinetics	62
4.2 Experimental Boundary Conditions	63
4.3 Global Reaction Rate Constant Measurement	64
CHAPTER 5. Investigation of Product Composition in Ozone Initiated Ethylene Oxidation Using GC at Room Temperature	68
5.1 Experimental Boundary Conditions	68
5.2 Chromatographs and Product Identification	69
5.3 Quantitative Analysis	73
CHAPTER 6. Comprehensive Product Characterization in Ozone Initiated Ethylene Oxidation Using SRPI-MBMS at Room Temperature	77
6.1 Experimental Boundary Conditions	77
6.2 Species Characterization	78
6.3 Alcohol	80
6.4 Aldehyde	84
6.5 Hydroperoxide	86
6.5.1 sCI Insertion and Oligomerization	86
6.5.2 Ozonolysis Mechanism	89
6.5.3 Low-Temperature Oxidation Mechanism	91
CHAPTER 7. Direct Detection of Organic Peroxy Radicals in Ozone Initiated Ethylene Oxidation at Room Temperature	94
7.1 Experimental Boundary Conditions	94
7.2 Electronic Structure Calculations	95
7.3 CH ₃ OO and C ₂ H ₅ OO	96
7.4 CH ₂ =CHOO and HOCH ₂ CH ₂ OO	100
7.5 Experiments with n-C ₄ H ₁₀ Addition	103
7.6 Peroxy Radicals Derived from sCI Reaction	106
CHAPTER 8. Dynamics of Laminar Ethylene Lifted Flame with Ozone Addition 109	
8.1 Computational Framework	109
8.1.1 Numerical Set-up	109
8.1.2 Chemical Kinetic Model	111
8.2 Steady Lifted Flames Without O ₃ Addition	112
8.2.1 The Establishment of Steady C ₂ H ₄ Lifted Flames	112
8.2.2 Effect of Co-flow Conditions on Flame Liftoff	114
8.3 Effect of O ₃ Addition on C ₂ H ₄ Lifted Flame	116
8.3.1 Flame Liftoff Height, H _L	116
8.3.2 CH ₂ O PLIF Measurement	118
8.4 Numerical Simulation and Analysis	120
8.4.1 Effect of O ₃ Addition on S _{tri}	120
8.4.2 Effect of Fluid Composition on u _{st}	122
8.4.3 2-D Reacting Flow Simulations using ANSYS Fluent	123

CHAPTER 9. Conclusions and Future Recommendations	128
9.1 Kinetic Study on O ₃ Initiated C ₂ H ₄ Oxidation at Room Temperature	128
9.2 Effect of O ₃ Addition on C ₂ H ₄ Laminar Flame Dynamics	129
9.3 Future Recommendations	130
APPENDIX A. Dimensional Drawings of Components in the Fast-Mixing Flow Reactor System	132
REFERENCES	135

LIST OF TABLES

Table 1	Description of installed modules in the INFICON Micro GC Fusion® Gas Analyzer.	47
Table 2	Specifications of Thorlabs LED255J.	50
Table 3	Initial reactant mole fractions and volumetric flow rates in the 255 nm absorption experiments at room temperature and pressure. Both C ₂ H ₄ and O ₂ are measured by the GC, and O ₃ is given by the O ₃ monitor.	63
Table 4	Designed reactant mole fractions for the three cases in the GC experiments at room temperature and atmospheric pressure.	68
Table 5	Measured species relative concentrations (in ppmv) by GC in O ₃ initiated C ₂ H ₄ oxidation at room temperature and atmospheric pressure, under flow residence time ~ 1 s.	74
Table 6	Product yields in O ₃ initiated C ₂ H ₄ oxidation at room temperature and atmospheric pressure, under flow residence time ~ 1 s.	74
Table 7	Summary of identified alcohols in O ₃ initiated C ₂ H ₄ oxidation at room temperature.	80
Table 8	Summary of identified aldehydes in O ₃ initiated C ₂ H ₄ oxidation at room temperature.	84
Table 9	Summary of identified hydroperoxides produced by sCI bimolecular reactions in O ₃ initiated C ₂ H ₄ oxidation at room temperature.	87
Table 10	Summary of identified hydroperoxides produced by ozonolysis channels in O ₃ initiated C ₂ H ₄ oxidation at room temperature.	89
Table 11	Summary of identified hydroperoxides produced via the tradition low-temperature fuel oxidation mechanism in O ₃ initiated C ₂ H ₄ oxidation at room temperature.	91
Table 12	DLPNO-CCSD(T)/cc-pVQZ//B2PLYP-D3/cc-pVTZ energies of characterized RO ₂ radicals in O ₃ initiated C ₂ H ₄ oxidation at T = 298 K.	96
Table 13	Bond distances (Å) and angles (deg) optimized at the B2PLYP-D3/cc-pVTZ Level of Theory.	96

Table 14	Summary of reaction rate constants of C ₂ H ₄ and n-C ₄ H ₁₀ with respect to selected free radicals and O ₃ at T = 300 K, in the unit of cm ³ /mole s.	104
Table 15	Summary of identified RO \dot{O} radicals possibly produced from bimolecular reaction of sCI at room temperature. All listed AIEs are calculated at DLPNO-CCSD(T)/cc-pVQZ//B2PLYP-D3/cc-pVTZ level of theory.	106
Table 16	Summary of O ₃ elementary reactions from Ref. [10] and 4-channel C ₂ H ₄ +O ₃ model.	112

LIST OF FIGURES

Figure 1.1	Example of combustion at extreme conditions: the schematic of scramjet and some typical challenges in operation. (from Ref. [1])	1
Figure 1.2	The images of filtered (centered at 430 nm) chemiluminescence of autoignition at room temperature and atmospheric pressure, with C ₂ H ₄ jet and O ₂ /O ₃ /N ₂ co-flow. (from Ref. [16])	3
Figure 1.3	The images of broadband chemiluminescence of the formation of multiple ignition kernels at room temperature and atmospheric pressure, with C ₂ H ₄ jet and O ₂ /O ₃ /N ₂ co-flow. (from Ref. [17])	4
Figure 1.4	Threefold influence of O ₃ addition on unsaturated fuel combustion.	5
Figure 2.1	The formation and concerted decomposition of POZ in general Criegee mechanism. (from Ref. [2])	9
Figure 2.2	The formation and stepwise decomposition of POZ into biradical, as proposed by O' Neal and Blumstein. (from Ref. [38])	10
Figure 2.3	Summarized detail mechanism of C ₂ H ₄ +O ₃ . Intrinsic ozonolysis products are framed in black boxes. Minor channels are noted by dashed arrows.	12
Figure 2.4	The calculated energy distribution of vibrationally excited CH ₂ OO* in C ₂ H ₄ +O ₃ at T = 300 K and P = 760 torr. (from Ref. [42])	18
Figure 2.5	The measured mole fractions of (a) C ₂ H ₄ , (b) O ₃ and (c) CH ₂ O from T = 300 K to 1100 K and P = 700 torr, with initially 2% C ₂ H ₄ , 12% O ₂ , 1000 ppmv O ₃ and residence time of 1.3 s in the JSR. (from Ref. [65])	20
Figure 2.6	The mole fractions of (a) some oxygenated species and (b) hydroperoxides from T = 300 K to 1000 K and P = 700 torr, with initially 2% C ₂ H ₄ , 12% O ₂ , 1000 ppmv O ₃ and residence time of 1.2 s in the JSR. (from Ref. [65])	22
Figure 2.7	Laminar flame speeds of CH ₄ at (a) different ϕ with ranging O ₃ concentrations, and (b) different O ₃ additions with ranging ϕ . Measurements were conducted using a premixed heat flux burner at atmospheric pressure. (from Ref. [10])	23

Figure 2.8	The flame speed enhancements of syngas and air with O ₃ additions. Measurements were conducted using a premixed heat flux burner at atmospheric pressure. (from Ref. [11])	24
Figure 2.9	The change in liftoff heights of non-premixed laminar C ₃ H ₈ lifted flame with O ₃ addition at atmospheric pressure. (from Ref. [8])	25
Figure 2.10	Flame speeds and enhancements with O ₃ addition of laminar C ₃ H ₈ lifted flame as function of mixture fraction gradient. (from Ref. [8])	26
Figure 2.11	Effect of O ₃ addition on flame speed of C ₂ H ₄ in air at room temperature and atmospheric pressure. (from Ref. [12])	27
Figure 2.12	Effect of O ₃ addition on flame speed of C ₂ H ₄ in air at unburned gas mixture T ₀ = 200 K and atmospheric pressure. (from Ref. [12])	28
Figure 2.13	Premixed Bunsen burner flames of C ₂ H ₂ +air at atmospheric pressure. The air was partially ozonized in the upper flame. (from Ref. [19])	28
Figure 2.14	PIV measurements of premixed C ₂ H ₄ and synthetic air (a) without and (b) with 11000 ppmv O ₃ addition at P = 80.3 torr and $\phi = 1$. (from Ref. [20])	29
Figure 3.1	The geometry and dimensions of the very first flow reactor design.	33
Figure 3.2	The assembly of the very first fast-mixing flow reactor system. The picture of compact 304 stainless-steel muffler as fuel injector is inserted.	33
Figure 3.3	Numerical examination of the very first flow reactor system design. Non-reacting laminar flow results of (a) mole fraction of C ₂ H ₄ , (b) mole fraction of O ₂ , (c) mole fraction of O ₃ and (d) velocity magnitude.	34
Figure 3.4	Schematic of revised fuel injector and flow reactor assembly, the photograph of modified fuel injector in position is inserted.	35
Figure 3.5	Numerical examination of revised flow reactor system. (a) Velocity field and streamlines using modified fuel injector, (b) velocity field and streamlines using original muffler with blunt head as fuel injector, (c) non-reacting C ₂ H ₄ distribution and (d) mixing time estimation, time interval 5 ms between each dot.	36

Figure 3.6	Mixing between fuel and oxidizer in laminar cross-jet configuration.	37
Figure 3.7	Comparison of GC measured mole fractions of C ₂ H ₄ and O ₂ along the flow reactor centerline before (solid symbols) and after (open symbols) mixing optimization. No O ₃ is added.	38
Figure 3.8	Demonstration to the newly designed 20-outlets fuel injector assembly of (a) perspective view and (b) the flow paths of fuel and oxidizer streams.	40
Figure 3.9	The latest design of fast-mixing flow reactor system with 20-outlets fuel injector of (a) schematic and (b) direct photograph.	41
Figure 3.10	Computational domain and mesh in numerical simulation of the latest designed fast-mixing flow reactor system.	42
Figure 3.11	Simulated non-reacting mole fraction distributions of C ₂ H ₄ (XY plane) and O ₃ (YZ plane) of the latest designed flow reactor system	43
Figure 3.12	Simulated non-reacting mole fraction distributions of (a) C ₂ H ₄ and (b) O ₃ on Y cross-section 1 mm downstream of the fuel injector nosecone.	44
Figure 3.13	Non-reacting laminar flow field and streamlines by simulation of the latest designed flow reactor system.	45
Figure 3.14	Schematic of experimental set-up of kinetic study using fast-mixing flow reactor system and gas chromatography.	46
Figure 3.15	Direct photograph of coupling between INFICON GC and flow reactor system.	47
Figure 3.16	Summary of measured O ₃ absorption cross-sections at room temperature. (from Ref. [73])	49
Figure 3.17	Measured cross-sections in Hartley band of O ₃ absorption at room temperature. (from Ref. [73])	50
Figure 3.18	Collimated 255 nm UV light beam with diameter around 10 mm.	51
Figure 3.19	Schematic of experimental set-up of O ₃ measurement using UV LED absorption.	52
Figure 3.20	Direct photograph of coupling between UV LED absorption system and quartz flow reactor.	52

Figure 3.21	Linear regression between the measured O ₃ concentrations (in ppmv) by 255 nm UV absorption (x axis) and the authentic values given by the O ₃ monitor (y axis). The correction factor is given by the slope.	54
Figure 3.22	Overview of HLS-II at NSRL, Hefei, China, with energy of 800 MeV and constant beam current 400 mA.	56
Figure 3.23	Undulator beamline BL03U at HLS-II.	57
Figure 3.24	Schematic of coupling between SRPI-MBMS and the fast-mixing flow reactor system.	58
Figure 3.25	Direct photograph of fast-mixing flow reactor system being coupled to SRPI-MBMS at Combustion and Flame endstation, HLS-II, NSRL.	58
Figure 3.26	Structure of steady laminar lifted flame, direct photograph taken by SLR camera.	59
Figure 3.27	Schematic of laminar jet flame burner experimental set-up.	60
Figure 4.1	The measured O ₃ concentrations using 255 nm UV LED absorption along flow reactor without C ₂ H ₄ addition at room temperature and pressure.	64
Figure 4.2	Measured O ₃ decays in flow reactor with $(C_2H_4)_0/(O_3)_0 \approx 190$ at room temperature and atmospheric pressure. Linear regression of raw data given in the red line.	65
Figure 4.3	Comparison between the newly measured rate constant k of C ₂ H ₄ +O ₃ in this study at ambient conditions, and the selected results from past literatures in NIST Chemical Kinetics Database. Applied diagnostic methods and temperature conditions are given in boxes.	6671
Figure 5.1	Chromatographs without O ₃ addition of excessive C ₂ H ₄ (red), excessive O ₃ (blue) and C ₂ H ₄ :O ₃ ≈ 1 (black) cases.	69
Figure 5.2	Chromatograph by module A with O ₃ addition of excessive C ₂ H ₄ (red), excessive O ₃ (blue) and C ₂ H ₄ :O ₃ ≈ 1 (black) cases, with retention time 35 s to 140 s.	70
Figure 5.3	Chromatograph by module B with O ₃ addition of excessive C ₂ H ₄ (red), excessive O ₃ (blue) and C ₂ H ₄ :O ₃ ≈ 1 (black) cases, with retention time (a) 15 s to 55 s and (b) 55 s to 145 s.	71

Figure 5.4	Chromatograph by module C with O ₃ addition of excessive C ₂ H ₄ (red), excessive O ₃ (blue) and C ₂ H ₄ :O ₃ ≈ 1 (black) case, with retention time (a) 55 s to 78 s and (b) 78 s to 140 s.	72
Figure 6.1	The mass spectrum of O ₃ initiated C ₂ H ₄ oxidation at room temperature and atmospheric pressure, from m/z = 15 to 30 with fixed photon energy of 14.49 eV.	78
Figure 6.2	The PIE curves of (a) m/z = 26, C ₂ H ₂ and (b) m/z = 46. The evaluated ionization energies from NIST are illustrated by shaded columns and measured PICS curves from Ref. [97] are overlapped.	79
Figure 6.3	The PIE curve of m/z = 44. Measured PICS curves of ethenol (red) and acetaldehyde (blue) from Ref. [101] are given. Fitted PICS (green) with combined ethenol and acetaldehyde is superimposed on experimental data.	81
Figure 6.4	The PIE curves of (a) m/z = 58, C ₃ H ₆ O, and (b) m/z = 60, C ₂ H ₄ O ₂ . Measured PICS curve (red) of 2-propen-1-ol from Ref. [104] overlapped.	83
Figure 6.5	The PIE curves of (a) m/z = 56, C ₃ H ₄ O, and (b) m/z = 58, C ₂ H ₂ O ₂ . Estimated PICS curve of acrolein is superimposed.	85
Figure 6.6	Direct photographs of (a) highly viscous liquid accumulated on the inner wall of the flow reactor and (b) liquid sample collected with pungent odor and faint yellow color.	88
Figure 6.7	The PIE curves of (a) m/z = 76, C ₂ H ₄ O ₃ and (b) m/z = 90, C ₃ H ₆ O ₃ . Ref. IEs are given in shaded columns for SOZ (grey), keto-hydroperoxide (yellow) and ester (blue), adopted from Rousso et al. [65, 66].	89
Figure 6.8	The PIE curves of (a) m/z = 48, CH ₄ O ₂ , (b) m/z = 62, C ₂ H ₆ O ₂ and (c) m/z = 78, C ₂ H ₆ O ₃ . The AIEs of ROOH are calculated at DLPNO-CCSD(T)/cc-pVQZ//B2PLYP-D3/cc-pVTZ level of theory and marked by the vertical lines.	92
Figure 7.1	Experimental PIE curves of (a) m/z = 47, CH ₃ O ₂ , and (b) m/z = 61, C ₂ H ₅ O ₂ , with inset of C ₂ H ₅ , recorded at both P = 30 torr with 0.025 eV/step, and P = 760 torr with 0.02 eV/step. Calculated AIEs are marked by vertical lines in red.	97
Figure 7.2	Experimental PIE curves of (a) m/z = 59, C ₂ H ₃ O ₂ , and (b) m/z = 77, C ₂ H ₅ O ₃ , recorded at P = 760 torr with 0.02 eV/step. Calculated AIEs are marked by vertical lines in red.	101

Figure 7.3	Mass spectrums with (in red) and without (in black) scavenger at ambient conditions, recorded with photon energy 10.5 eV. The added n-C ₄ H ₁₀ concentration is 10 times the initial C ₂ H ₄ concentration.	103
Figure 7.4	The PIE curves of (a) m/z = 73, C ₃ H ₅ O ₂ , (b) m/z = 89, C ₃ H ₅ O ₃ , (c) m/z = 93, C ₂ H ₅ O ₄ and (d) m/z = 123, C ₃ H ₇ O ₅ . The calculated AIE at DLPNO-CCSD(T)/cc-pVQZ//B2PLYP-D3/cc-pVTZ level of theory is designated in red vertical line.	107
Figure 8.1	Schematic of the 2-D axisymmetric computation domain of the jet flame burner and the structured meshes.	110
Figure 8.2	Direct photographs of steady lifted flames in series with different C ₂ H ₄ jet velocities start from $u_f = 2.98$ m/s, and 12.7% O ₂ +87.3% N ₂ co-flow with constant velocity of $U_{CO} = 0.013$ m/s.	113
Figure 8.3	Comparison of numerical simulations of stoichiometric contours (solid line) in non-reacting jet and the triple point positions (solid point) of lifted flames measured experimentally. Different u_f distinguished by colors.	114
Figure 8.4	Experimentally measured H _L with different co-flow conditions of (a) constant $U_{CO} = 0.016$ m/s with different O ₂ concentrations and (b) constant 11.5% O ₂ with different U_{CO} .	115
Figure 8.5	The change in measured H _L with (a) increasing O ₃ addition in co-flow at different u_f and (b) ranging u_f of constant O ₃ in co-flow	117
Figure 8.6	CH ₂ O PLIF (blue) and broadband chemiluminescence (red) of lifted flames with different O ₃ concentrations at (a) $u_f = 3.10$ m/s and (b) $u_f = 3.57$ m/s.	118
Figure 8.7	Comparison between the CH ₂ O distributions at $u_f = 3.24$ m/s and 1300 ppmv O ₃ addition in the co-flow. Left: simulated reacting co-flow jet (no flame) using Fluent. Right: the CH ₂ O PLIF by experiments	119
Figure 8.8	Calculated S_L with different amounts of O ₃ addition using PFR + Laminar Flame Speed model in CHEMKIN.	121
Figure 8.9	Simulated CH ₂ O distributions of C ₂ H ₄ lifted flames before and after O ₃ addition. (a) H _L decrease (b) H _L increase and (c) blow-out. The stoichiometric contour $Y_F = Y_{F, st}$ is marked with the red line.	123

Figure 8.10	Numerical results along the $Y_F = Y_{F,st}$ contour of C ₂ H ₄ lifted flames with (dashed lines) and without (solid lines) O ₃ addition. (a) Mole fraction of CH ₂ O and (b) u_{st} .	124
Figure 8.11	Simulated temperature fields of C ₂ H ₄ lifted flames before and after O ₃ addition. (a) H _L decrease and (b) H _L increase. The stoichiometric contour $Y_F = Y_{F,st}$ is marked with the red line.	125
Figure 8.12	The numerical results of (a) temperature along $Y_F = Y_{F,st}$ contour of C ₂ H ₄ lifted flames with (dashed lines) and without (solid lines) O ₃ addition, and (b) relative enhancement in S_L of C ₂ H ₄ in air with increasing unburned gas temperature from 300 K to 330 K.	126
Figure A.1	The nosecone welded to the muffler fuel injector (unit in inch).	132
Figure A.2	Alternative fuel injector design of single row fuel outlets (unit in inch).	132
Figure A.3	Quartz flow reactor with C-D section design (unit in mm).	133
Figure A.4	The design of 20-outlets fuel injector, head part (unit in mm).	133
Figure A.5	The design of 20-outlets fuel injector, support ring (unit in mm).	134
Figure A.6	The design of 20-outlets fuel injector, fuel inlet (unit in mm).	134

LIST OF SYMBOLS AND ABBREVIATIONS

S_L	Laminar flame speed (cm/s)
k	Reaction rate constant ($\text{cm}^3/\text{mole s}$ for second order reaction)
u_f	Velocity of fuel jet (m/s)
H_L	Flame liftoff height (cm)
S	Coefficient of variation
N_A	Avogadro constant, 6.02×10^{23} /mole
Y_F	Fuel mass fraction
$Y_{F, st}$	Fuel mass fraction at unity stoichiometry
S_{tri}	Propagation speed of triple flame
u_{st}	Axial flow velocity along stoichiometric contour
E_a	Activation energy (kJ/mole or kcal/mole)
U_{CO}	Co-flow velocity (m/s)

SUMMARY

Ozone (O_3) addition has been proved to be efficient and effective in combustion enhancement and control. For saturated fuels, it is recognized that the O_3 decomposition at elevated temperatures dominantly contributes to the improvement. However, for unsaturated fuels, the knowledge is still quite limited, due to the significantly more complicated kinetic pathways induced by direct reaction between fuel and O_3 , i.e., the ozonolysis reaction.

In this dissertation, the O_3 initiated ethylene (C_2H_4) oxidation is experimentally investigated at room temperature using multiple diagnostic methods. To accommodate the rapid reaction between C_2H_4 and O_3 , a novel flow reactor system with online fast-mixing feature is designed, manufactured, and deployed in experiments. By coupling the flow reactor system to 255 nm UV LED absorption technique, the global reaction rate constant of $C_2H_4+O_3$ is measured at ambient conditions. Being supplementary to the results in previous studies, many new products and intermediates are rigorously identified in this chemical system of room-temperature C_2H_4 oxidation, using both gas chromatography and tunable photoionization mass spectrometry. Based on determined molecular structures, the detected species can be mainly categorized into alcohol, aldehyde, and peroxide, while many of them have been widely considered as key intermediates in low-temperature oxidation chemistry. Moreover, direct probing and characterization of multiple highly reactive organic peroxy radicals are succeeded, which are proposed to be generated via either classic low-temperature oxidation mechanism or possible bimolecular reaction between radicals and stabilized Criegee Intermediate.

Additionally, the effect of ozonolysis reaction on laminar flame dynamics is studied. Stable C_2H_4 lifted flames are established with oxygen/nitrogen co-flow at reduced oxygen content conditions. By adding certain amounts of O_3 into the oxidizer co-flow, non-monotonic flame dynamic behaviors are recorded. Depending on the initial value of the flame liftoff height before O_3 is added, it is observed that the flame liftoff height could either increase or decrease. Formaldehyde (CH_2O) planar laser-induced fluorescence (PLIF) measurement shows that prompt ozonolysis reaction between C_2H_4 and O_3 produces large amounts of CH_2O upstream of the flame. In contrast to previous studies of O_3 addition on lifted flames—with saturated fuels in which O_3 decomposition dominates—the ozonolysis reaction between C_2H_4 and O_3 considerably changes the chemical composition of fuel jet even at room temperature. Such chemical reaction causes the simultaneous increase of both triple flame propagation speed of lifted flame and axial jet velocity along the stoichiometric contour, which also therefore changes the dynamic balance between these two values to stabilize the flame. While the increase of triple flame propagation speed tends to decrease the flame liftoff height, the increase of axial jet velocity along the stoichiometric contour tends to have the opposite effect. A competing kinetic-dynamic process forms, and the final location of the flame depends on the degree of ozonolysis reaction, which is determined by the initial flame position before O_3 is added.

In summary, this dissertation experimentally presents that the regular temperature window for fuel oxidation is dramatically lowered to room temperature by the help of ozonolysis reaction, which greatly alters the reaction pathways and affects the flame dynamic behavior. The results could contribute to the general O_3 assisted combustion of unsaturated fuels in practical applications in the future

CHAPTER 1. INTRODUCTION

1.1 Background and Motivation

Nowadays, with the aim of higher energy efficiency and performance, as well as lower emission, demands on fossil fuel combustion at near-limiting conditions are ever-increasing. For example, in the circumstance of ultra-high-speed airbreathing propulsion of supersonic combustion ramjets (scramjets), many challenges in practical operation exist as demonstrated in Figure 1.1. With hypersonic air intake, the averaged residence time in the engine is approximately in the order of 1~3 milliseconds [1], which could be much smaller than the ignition delay of fuels in conventional combustion scheme, causing great difficulty in both ignition and flame stabilization. To confront such issue, one solution is the development of innovative combustion concepts. By possibly enhancing the reactivity of chemical system between fuel and oxidizer, the parameters of combustion at extreme conditions might be consequently improved.

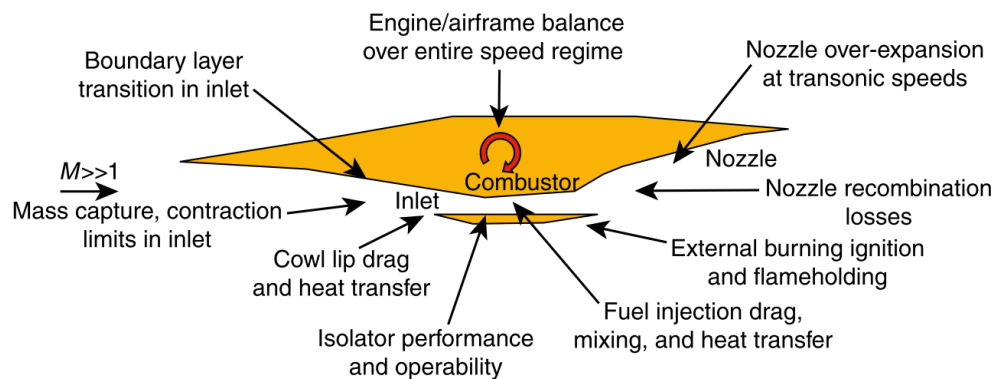


Figure 1.1. Example of combustion at extreme conditions: the schematic of scramjet and some typical challenges in operation. (from Ref. [1])

Among many new concepts, ozone (O_3) addition [2] has been proven a promising strategy to improve ignition [3-7], laminar flame speed (S_L) [8-12] and flame stabilization [13-15] of saturated fuels. It has been recognized that such enhancements are principally from the production of \dot{O} radicals through O_3 decomposition at elevated temperatures near the flame front, $O_3(+M) \rightarrow O_2+\dot{O}(+M)$, which kinetically speeds up the overall chain-propagating process. The direct reaction between O_3 and saturated fuel is virtually negligible. However, for unsaturated fuels, because of the nearly barrierless, exothermic reaction between fuel molecule and O_3 , namely, the ozonolysis reaction, the scenario is entirely changed. In general, the difference between reaction rate constants of alkene (unsaturated hydrocarbons) and alkane (saturated hydrocarbons) with O_3 respectively could be in the order of $k_{alkene,O_3}/k_{alkane,O_3} \sim 10^6$ [16]. Although considerable studies have been remarked on the O_3 assisted combustion of alkanes, investigations on alkenes are sparse, partially due to the much higher complexity in chemistry induced by the ozonolysis reaction.

Not long ago, in our lab, autoignition was surprisingly observed by Gao et al. [16] in a non-premixed jet of ethylene (C_2H_4), O_3 and O_2 at room temperature and atmospheric pressure (i.e., $T \approx 298$ K and $P \approx 760$ torr), without any additional energy input externally. Such observation is shown in Figure 1.2, where the velocity of C_2H_4 jet was set as $U_{jet} = 13.6$ m/s, and the velocity of $O_2/O_3/N_2$ co-flow was $U_{co-flow} = 2.6$ m/s. The overall concentration of O_3 addition was 3.7% among the reactants. By utilizing a high-speed camera, dramatic increase in flame propagation speed was measured, owing to the continuous formation of multiple autoignition kernels upstream as shown in Figure 1.3. The equivalent flame front propagation speed could be as high as one hundred times faster

than the conventional S_L at corresponding conditions. Further experiments indicated that the phenomenon could not be reproduced if C_2H_4 was replaced by saturated fuels, e.g., methane (CH_4), which clearly implied the necessity of ozonolysis reaction in such an autoignitive process. This unique observation not only vividly depicts a prospective scheme for active combustion enhancement and control at low-temperature conditions, but also bridges the long studied atmospheric chemistry with novel combustion concepts.

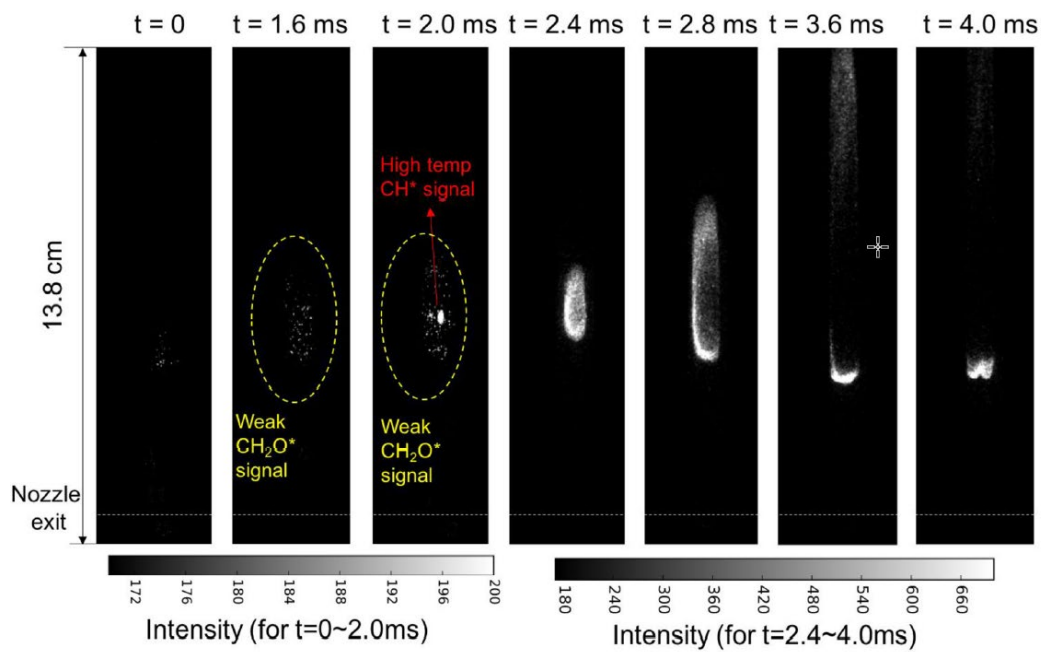


Figure 1.2. The images of filtered (centered at 430 nm) chemiluminescence of autoignition at room temperature and atmospheric pressure, with C_2H_4 jet and $O_2/O_3/N_2$ co-flow. (from Ref. [16])

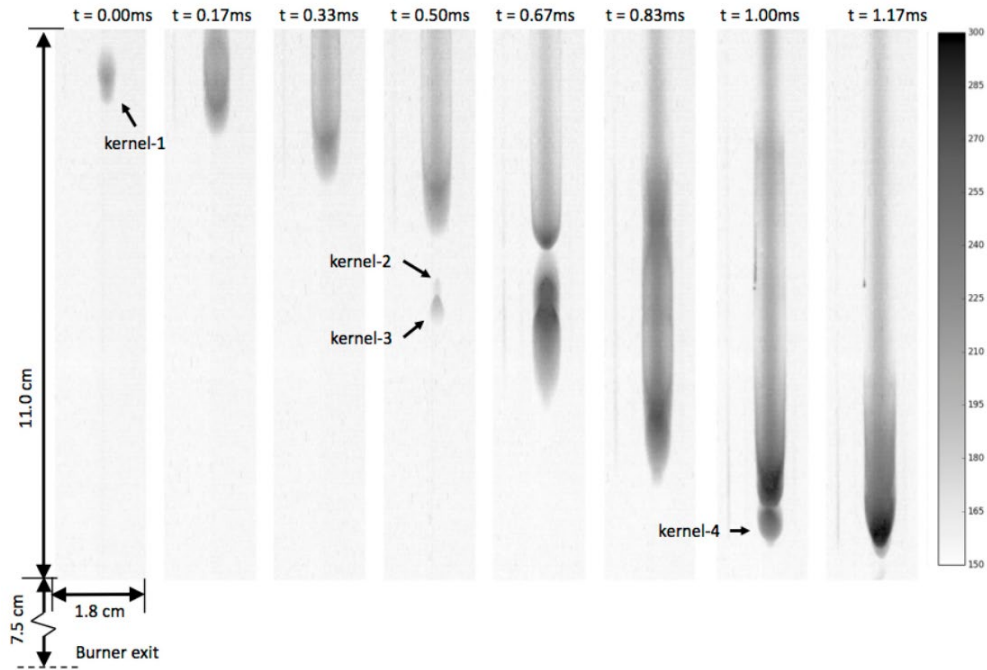


Figure 1.3. The images of broadband chemiluminescence of the formation of multiple ignition kernels at room temperature and atmospheric pressure, with C_2H_4 jet and $O_2/O_3/N_2$ co-flow. (from Ref. [17])

Similar to the widely studied plasma assisted combustion [18], the influences delivered by O_3 addition to unsaturated fuel combustion are believed to be threefold, as summarized in Figure 1.4. First, being a highly exothermic reaction, the ozonolysis of fuel results in abundant heat release, which would in turn accelerate the global reaction rate. Second, great amounts of ozonolysis products, including reactive species and fuel fragments such as formaldehyde (CH_2O), hydrogen (H_2) and carbon monoxide (CO), are rendered into the chemical system, and therefore increase the global reactivity. Moreover, based on the mechanism, small free radicals, such as hydroxyl radical ($\dot{O}H$), formyl radical ($H\dot{C}O$) and hydrogen atom (\dot{H}) are natively produced with relatively high yields from the ozonolysis reaction. Kinetically, all these radicals could either initiate or propagate chain-reactions in the oxidation of fuel molecule, and consequently enhances the combustion

process. Third, the change in gas composition from the diverse ozonolysis products would surely affect the transportation properties and modify the physical fields in combustion, making impact on the dynamic characteristics of flame.

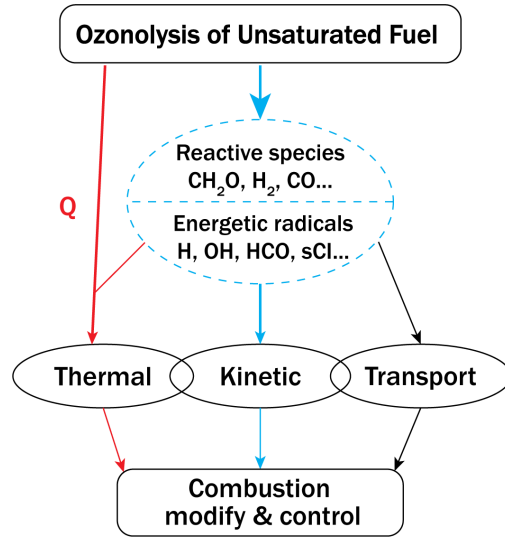


Figure 1.4. Threefold influence of O₃ addition on unsaturated fuel combustion.

1.2 Problem Statements

Being one of the most prevalent reactions in the troposphere, the ozonolysis reaction has a profound history among atmospheric chemists, however, it is quite a fresh concept to the combustion society until recently. Unlike the conditions in the atmosphere, where the concentrations of reactants, i.e., unsaturated volatile organic compounds (VOCs) and O₃, are merely in the level of part per billion by volume (ppbv), the characteristic reaction time scale might be hours or even days. However, in practical O₃ assisted combustion, the concentration of added O₃ could be easily higher than 1000 part per million by volume (ppmv), resulting in a much smaller reaction time scale. Furthermore, with high concentrations in both fuel and oxidizer, the complex secondary reactions induced by the ozonolysis products with high reactivity can no longer be neglected and may greatly

contribute to the overall fuel oxidation in combustion. In the current case of C₂H₄, even though the reaction of C₂H₄+O₃ has been extensively studied for decades, the knowledge gap between ozonolysis and combustion exists, or specifically, the detail chemistry leading to the room-temperature autoignition in C₂H₄ with O₂/O₃/N₂ co-flow remains unclear.

Different from conventional fuel oxidation, which is confined in the flame zone, the high reactivity between unsaturated fuel and O₃ renders immediate reaction and heat release far upstream upon mixing. Such a feature (combustion region) has not been studied before. The influence of O₃ addition on S_L of C₂H₄ was previously investigated in premixed configurations [12, 19, 20]. It was reported that at atmospheric pressure, adding O₃ would decrease S_L , while at sub-atmospheric pressure, enhancement in S_L was measured. Based on kinetic simulations, Gao et al. [12] concluded that the reaction of C₂H₄+O₃ has a positive effect on S_L by providing reactive species such as CH₂O and H₂. Meanwhile, the premixed configuration induces heat loss to the burner wall which decreases the total enthalpy of the reaction system, thus lowering S_L . At low pressures, the ozonolysis reaction is weakened given a limited residence time upstream of the flame zone. Therefore, S_L would be increased via O₃ decomposition, which is similar to the result with saturated hydrocarbons. Nevertheless, the effect of the ozonolysis reaction on flame dynamics has not been studied in detail.

1.3 Objectives

As the follow-up work to Gao et al. [16, 17, 21-24], the first objective of this dissertation is to further investigate the complex chemistry of the C₂H₄ oxidation initiated by O₃ at room temperature, under which the fuel conversion starts and finally translates to

the observed autoignition. Specifically, there are two questions attempted to be answered: 1) What is the global rate constant of reaction $C_2H_4+O_3$, 2) What are the products and intermediates in this room-temperature oxidation of C_2H_4 and the secondary reactions following the initial ozonolysis. To address these questions, a novel flow reactor system with online fast-mixing feature is designed, manufactured, and deployed in experiments. In the corresponding chemical kinetic studies, multiple diagnostic methods are coupled to the flow reactor, including light-emitting diode (LED) absorption, gas chromatography (GC), and tunable photoionization mass spectrometry. If not specifically mentioned, the kinetic experiments are carried out at room temperature and atmospheric pressure, which are also referred as the ambient conditions. The precise values of the conditions would strongly depend on the physical locations of labs, and nearly consistent $T \approx 298$ K and $P \approx 740$ to 760 torr are recorded in the experimental environment.

The second objective of this dissertation is to expand our knowledge on the influence of ozonolysis reaction on flame dynamics. In detail, the effect of O_3 addition on C_2H_4 flame dynamics is studied using a non-premixed jet flame burner, where the oxidizer mixture is given as the co-flow. By tuning the co-flow composition without O_3 , stable C_2H_4 lifted flames are obtained in the laminar regime at atmospheric pressure. With quantitative amounts of O_3 added into the oxidizer co-flow, different from the monotonic appearance in similar experiments using saturated fuel, two-way flame dynamic behaviors are observed as a function of fuel jet velocity (u_f). Planar laser-induced fluorescence of CH_2O is undertaken to confirm the existence and visualize the spatial distribution of C_2H_4 ozonolysis reaction. Numerical simulations are also performed to understand the highly coupled kinetic and dynamic process.

1.4 Dissertation Outline

The dissertation is structured in nine chapters. In Chapter 2, literature review is presented on the detail chemistry of both general ozonolysis mechanism and the specific reaction of $C_2H_4+O_3$. Regarding the flame, previous works on effect of O_3 addition on the flame speed are summarized for both saturated and unsaturated fuels. In Chapter 3, the designs of the fast-mixing flow reactor system are demonstrated chronologically, together with all experimental diagnostic methods applied in this dissertation. Using the absorption method at 255 nm, the newly obtained reaction rate constant of $C_2H_4+O_3$ is demonstrated in Chapter 4, and the result is compared with the reference values found in NIST Chemical Kinetics Database. Chapter 5 covers the kinetic experiment by GC and some species are identified as major products from the room-temperature oxidation of C_2H_4 initiated by O_3 . The relative concentrations of identified species are measured as well as their production yields in terms of the C_2H_4 consumption. Then in Chapter 6 and 7, comprehensive species characterization using tunable photoionization mass spectrometry and quantum chemistry calculation is presented. The possible kinetic pathways initiated by the ozonolysis reaction are proposed. The effect of O_3 addition on C_2H_4 flame dynamics is investigated in Chapter 8 using non-premixed laminar lifted flame. Finally, in Chapter 9, the conclusions to this dissertation and recommendations to future work are given.

CHAPTER 2. STATE-OF-THE-ART OF ETHYLENE

OZONOLYSIS CHEMISTRY

2.1 General Mechanism of Ozonolysis Reaction

In 1847, Christian Friedrich Schönbein firstly reported the reaction between gaseous C_2H_4 and O_3 [25]. He noticed that this specific reaction would not lead to carbon dioxide (CO_2) as the highest oxidation state of organic substances, but rather aldehyde and carboxylic acids, which were determined as CH_2O , acetic acid (CH_3COOH) and formic acid ($HCOOH$) later in 1868 [26]. Although Schönbein's discover was qualitative, it laid a foundation and gave great insights for future studies.

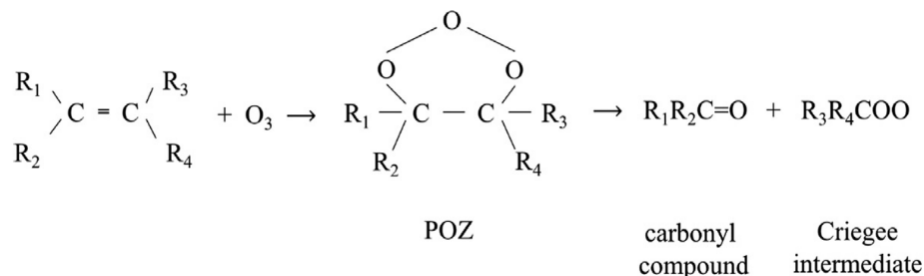
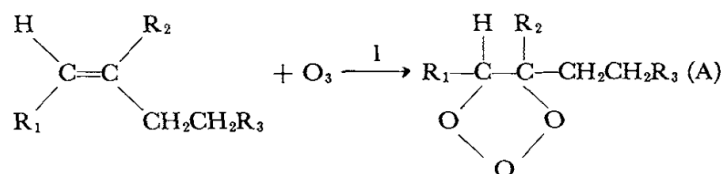


Figure 2.1. The formation and concerted decomposition of POZ in general Criegee mechanism. (from Ref. [2])

The well-accepted mechanism of ozonolysis reactions was proposed by Rudolf Criegee in 1949 as a three-step mechanism [27], which is now named after him. It was suggested by him that most ozonolysis reactions are initiated by a highly exothermic 1,3 dipolar cycloaddition [28] of O_3 onto carbon double bond, i.e., $C=C$, making a weak van der Waals π complex O_3 -alkene [29-31] and immediately followed by the formation of a 1,2,3-trioxy cyclic primary ozonide (POZ). The second step is POZ decomposing into a

carbonyl compound and carbonyl oxide, which is also known as the famous Criegee intermediate (CI), via homolytic cleavage of C-C and C-O σ bonds. Such mechanism is termed as concerted decomposition of POZ and is demonstrated as Figure 2.1. In condensed-phase reaction, the carbonyl compound and CI would then recombine into a 1,2,4-trioxy cyclic secondary ozonide (SOZ) via cycloaddition. By adding ketones and aldehydes into the solution where alkene ozonolysis reactions occur, different SOZs were observed [32] and serves as convincing proof to the proposed CI in Criegee mechanism. Meanwhile, the formation of both POZ and SOZ were detected using IR spectrum at extremely low temperature in condensed-phase experiments [33-36] and the proposed 1,2,3-trioxy cyclic structure of POZ was also confirmed by NMR spectrum [37].

Initial Reaction (Molozonide Formation):



Molozonide—biradical equilibria:

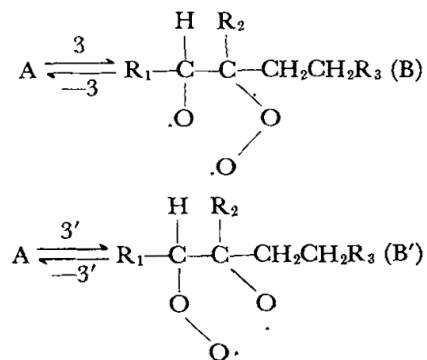


Figure 2.2. The formation and stepwise decomposition of POZ into biradical, as proposed by O' Neal and Blumstein. (from Ref. [38])

As a complement to the concerted cycloreversion of POZ suggested by Criegee, O'Neal and Blumstein [38] proposed an alternative pathway that the weakest O-O bond

could split singly and render to a POZ biradical, namely, the stepwise decomposition of POZ. The pathway is shown in Figure 2.2. This alternative mechanism has successfully explained some abnormal observations in gas-phase experiments, compared to the ones in condensed-phase [38] as mentioned above. Harding and Goddard [39] suggested in all gas-phase ozonolysis reactions, the slower quenching process of highly active intermediates allows many kinetic channels accessible and the formation of SOZ may no longer be dominant as recommended by Criegee, which makes the detail reaction pathways much more complicated.

2.2 C₂H₄ Ozonolysis Reaction with Advanced Approaches

Being the simplest case among all, the reaction of C₂H₄+O₃ has been extensively investigated for decades. Because of its kinetic representativeness, this reaction has been considered as the benchmark of corresponding ozonolysis of all terminal alkenes. Recently, with significant advancement in quantum chemistry calculation, as well as theory and computing power, some long-existed obscurities in gas-phased ozonolysis reaction are now being disclosed. Based on theoretical results suggested by high-level quantum calculations, the mechanism of C₂H₄+O₃ with detail kinetic pathways and channels is summarized in Figure 2.3.

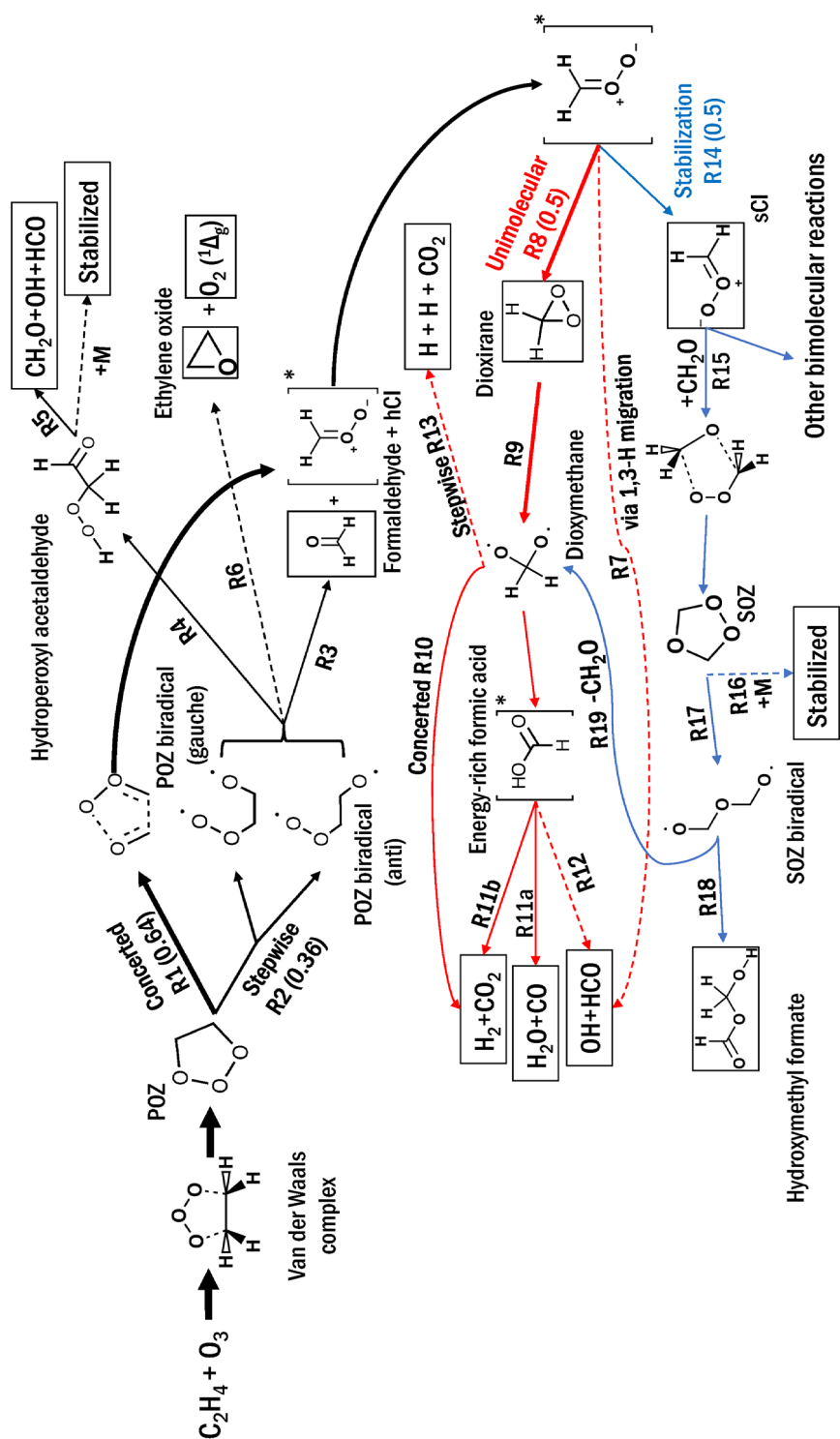
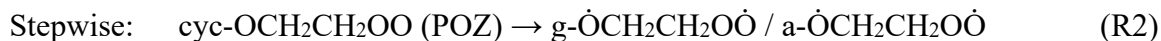


Figure 2.3. Summarized detail mechanism of $C_2H_4+O_3$. Intrinsic ozonolysis products are framed in black boxes. Minor channels are noted by dashed arrows.

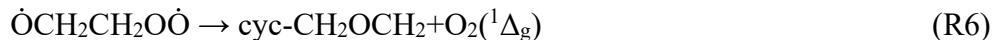
2.2.1 Primary Ozonide (POZ)

The initiation of C₂H₄ ozonolysis reaction, i.e., POZ formation, was calculated with an averaged activation energy of no more than 5.0 kcal/mole [40-43]. Theoretical calculations suggested both the concerted mechanism as proposed by Criegee, and the stepwise mechanism as proposed by O'Neal and Blumstein, are feasible in corresponding POZ (cyc-OCH₂CH₂OO) decomposition. The abundant internal energy over 50 kcal/mole in the nascent POZ results in comparable kinetic significance of both pathways. For the concerted POZ decomposition, a pair of carbonyl compound and "hot" CI, i.e., CH₂O+CH₂OO*, arises from homolytic O-O and C-C cleavage (R1). For the stepwise POZ decomposition, the sole scission of loosely bonded O-O forms a singlet biradical $\dot{O}CH_2CH_2O\dot{O}$ (R2), of which both the gauche and anti-conformations are theoretically accessible [40, 41] with similar potential energies. Based on calculation, the overall energy barrier for concerted route R1 is lower than the stepwise route R2, giving R1 more favorable with theoretical branching ratio of R1:R2 = 0.64:0.36, at T = 300 K and P = 760 torr [40].



It has been further revealed that the POZ biradical $\dot{O}CH_2CH_2O\dot{O}$ may either decompose into CH₂O+CH₂OO* through scission of C-C bond (R3) or isomerize into the hydroperoxyl acetaldehyde (HCOCH₂OOH) via a 1,4-H migration (R4). With the high exothermicity from the isomerization, rapid breakdown of HCOCH₂OOH could occur and

end up with the production of fragments $\text{CH}_2\text{O}+\dot{\text{H}}\dot{\text{C}}\text{O}+\dot{\text{O}}\text{H}$ (R5) [40-42]. The close activation energies in theory indicated channel R3 and R4 are indeed competitive. Additional to R3 and R4, Anglada et al. [41] described a third channel by which the POZ biradical could directly decompose into ethylene oxide (cyc- CH_2OCH_2) and singlet oxygen, i.e., $\text{O}_2(^1\Delta_g)$ (R6). However, this channel would not be preferred due to a large 38 kcal/mole energy barrier to overcome, around 30 kcal/mole higher than the barriers for R3 and R4 relatively.



2.2.2 Criegee Intermediate (CI)

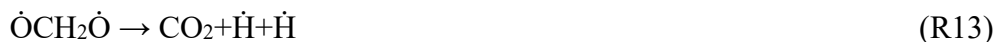
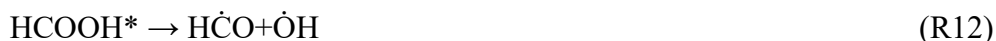
With abundant energy release from the POZ decomposition, the corresponding fragment, CH_2OO^* , namely, nascent CI or hCI, would be highly unstable. Theoretically two further unimolecular channels are feasible, along with the dethermalization pathway via third-body collision. The first unimolecular pathway for hCI is the direct breakdown into $\dot{\text{H}}\dot{\text{C}}\text{O}+\dot{\text{O}}\text{H}$ (R7) through 1,3-H shift and C-O bond rupture. However, it has been suggested that this trajectory is nearly negligible for its high energy barrier to overcome [40, 42, 44]. The second unimolecular pathway for hCI is the isomerization into vibrationally excited dioxirane (cyc- OCH_2O) (R8), followed by a prompt ring opening through O-O rupture, which finally producing the dioxymethane ($\dot{\text{O}}\text{CH}_2\dot{\text{O}}$) biradical (R9).

It was reported that the intermediate cyc-OCH₂O was detected in the gas-phase C₂H₄ ozonolysis reaction at T = 77 K with both intrusive [45] and non-intrusive [46] techniques, while no observation ever succeeded at elevated temperatures for its extremely short lifespan.



Being still highly energetic, the biradical $\dot{\text{O}}\text{CH}_2\dot{\text{O}}$ from R9 would have three further dissociation channels and produce several groups of products. The first channel is the production of H₂+CO₂ via the concerted scission of two C-H bonds with synchronous formation of H-H bond (R10). The second channel is through a transient excited formic acid (HCOOH*) midbody, both syn and anti-conformers are allowed [41]. The isomerizing trajectory from $\dot{\text{O}}\text{CH}_2\dot{\text{O}}$ to HCOOH* is almost 100 kcal/mole exothermic, and as a result, the syn-HCOOH* would promptly dissociate into CO+H₂O (R11a), while the anti-HCOOH* would break into H₂+CO₂ (R11b). As a supplement, the excited midbody can also dissociate into H $\dot{\text{C}}\text{O} + \dot{\text{O}}\text{H}$ (R12) via the direct C-O bond rupture, however, this is considered a minor pathway only for its higher relative potential energy [40] compared to R11a and R11b. The calculation implied that at T = 300 K and P = 760 torr, the dethermalization of HCOOH* into HCOOH is not competitive to the breakdown process. Therefore, the experimentally probed HCOOH by many should mainly originate from other sources, for instance, the bimolecular reaction of CH₂OO+H₂O [47]. The third

channel of $\dot{\text{O}}\text{CH}_2\dot{\text{O}}$ dissociation produces $\text{CO}_2+\dot{\text{H}}+\dot{\text{H}}$ (R13), though different trajectories had been proposed by Anglada et al. [41] and Nguyen et al. [42], no preference can be referred here. Noting that if the concerted Criegee mechanism R1 is the sole POZ decomposition route as supported by many, then the $\dot{\text{O}}\text{H}$ radical formation could only be through R7 and R12, delivering the yield of $Y_{\dot{\text{O}}\text{H}} \leq 5\%$ in theory [42, 44]. This prediction greatly deviates from the $Y_{\dot{\text{O}}\text{H}} = 12\sim 20\%$ [48-51] obtained by experiments. It was demonstrated that an extra 11% of $\dot{\text{O}}\text{H}$ can be provided if the stepwise POZ decomposition was included as the following sequence, $\text{POZ} \rightarrow \dot{\text{O}}\text{CH}_2\text{CH}_2\text{O}\dot{\text{O}} \rightarrow \text{HCOCH}_2\text{OOH} \rightarrow \text{CH}_2\text{O}+\text{H}\dot{\text{C}}\text{O}+\dot{\text{O}}\text{H}$ [42]. Such theoretical outcome further rationalizes the co-existence of R1 and R2 pathways in gas-phase C_2H_4 ozonolysis reaction.



Besides the described unimolecular reactions above, the hCI could also undergo dethermalization by a third-body collision and produce a stabilized zwitterion, i.e., CH_2OO (sCI) (R14), which is widely considered as one of the most important ozonolysis products.



Despite the theoretically predicted lifespan of sCI as long as couple seconds even at $T = 300$ K and $P = 760$ torr [42, 52], no direct observation of this species in a native ozonolysis system has been succeeded for decades. In 2012, with photolysis of $\text{CH}_2\text{I} + \text{O}_2$ at 248 nm, the artificial synthesis of CH_2OO allowed unambiguous probing of sCI for the first time ever and was measured to have lifespan no longer than 5 ms by Welz et al. [53]. In their experiment, the pressure was intentionally kept as $P = 4$ torr to ensure the high CH_2OO yield, however, the low pressure may greatly enhance the wall termination as well. Another study with identical photolysis scheme but different set-up at $P = 1300$ torr recorded a much longer lifespan of sCI up to around 1 s [52] instead. Therefore, the difficulty in direct sCI observation mainly arises from the depletion by prompt secondary reactions, giving it an extremely low equilibrium abundance in the ozonolysis system. In 2015, Womack et al. [54] firstly reported a weak signal in microwave spectrum that should correspond to sCI by experiment, with high initial reactant concentrations of $\text{C}_2\text{H}_4 + \text{O}_3$ at ambient conditions. Later in 2017, Berndt et al. [55] also announced the detection of sCI in a native C_2H_4 ozonolysis system by chemical ionization mass spectrometry (CIMS) at $T = 295 \pm 2$ K and $P = 760$ torr, where the reagent ions can selectively combine with sCI according to its proton affinity.

Many investigations have been conducted trying to learn the yield of sCI (Y_{sCI}) in C_2H_4 ozonolysis reaction. Due to the great difficulty in sCI probing, the commonly used experimental strategy has been indirect by adding excessive sCI scavengers and measuring the yields of relevant products. Being one of the strongest oxidizers in the atmosphere, sCI is capable to react with both organic and inorganic compounds [56, 57], which makes many scavenger candidates available. The results obtained by different scavengers such as CO

[48], HCOOH [58, 59], sulfur dioxide (SO₂) [60, 61] and also the total products yield analysis [62] have presented a relatively narrow span of $Y_{\text{sCl}} = 40\% \sim 50\%$. The reasonable consistency between experiment and theory has also been reported [40, 42]. Calculations with different models [40, 42] agreed on strong pressure dependency of Y_{sCl} in the C₂H₄ ozonolysis reaction, and a nearly doubled Y_{sCl} was predicted due to multiplied collisional frequency with pressure change from $P = 0.75$ torr to $P = 75000$ torr. Interestingly, it was shown that even at very low pressures, the theoretical Y_{sCl} could be as high as $Y_{\text{sCl}} = 36\%$ instead of approaching zero at $T = 300$ K [40, 42]. This could be explained by the intrinsic energy distribution of CH₂OO* as shown in Figure 2.4, that about 34% of total hCl contains energy insufficient to overcome the energy barrier of the isomerization channel R8, and would be stabilized consequentially regardless the rate of third-body collision [42]. On the contrary, a weak temperature dependency of Y_{sCl} in C₂H₄+O₃ reaction was found, as the ozonolysis reaction system is naturally low energy-barriered and highly exothermic.

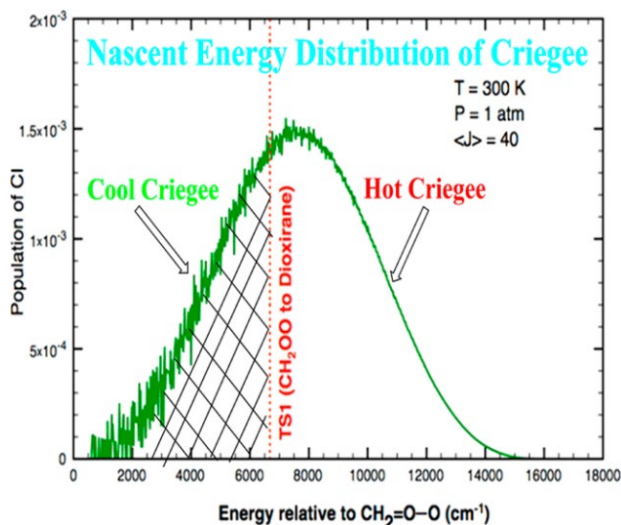
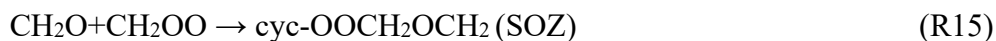


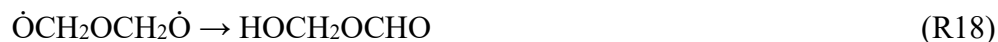
Figure 2.4. The calculated energy distribution of vibrationally excited CH₂OO* in C₂H₄+O₃ at $T = 300$ K and $P = 760$ torr. (from Ref. [42])

2.2.3 Secondary Ozonide (SOZ)

Deduced from Criegee's proposal, in C₂H₄ ozonolysis reaction, the produced sCI could in turn recombine with CH₂O through a 2,4-cycloaddition and yield 1,2,4-trioxolane, or the SOZ (cyc-OOCH₂OCH₂) (R15). Theoretical calculations clearly illustrated that this cycloaddition to SOZ is barrierless as the corresponding van der Waals transition state has even lower energy than the reactants of CH₂OO+CH₂O, and the overall reaction of R15 is highly exothermic by 46.0 kcal/mole [41, 63]. Accordingly, in the gas-phase ozonolysis of C₂H₄, most produced SOZ via R15 would go through further dissociation but only a small fraction can be finally stabilized (R16).



The SOZ dissociation starts with the rupture of O-O bond, though a 24.1 kcal/mole endothermicity [41] was suggested, a symmetric SOZ biradical $\dot{\text{O}}\text{CH}_2\text{OCH}_2\dot{\text{O}}$ (R17) could be formed. Parallel to the POZ biradical isomerization, the $\dot{\text{O}}\text{CH}_2\text{OCH}_2\dot{\text{O}}$ could also proceed via a 1,4-H migration and then yield the hydroxymethyl formate (HOCH₂OHCO) (R18) [60, 64]. Another follow-up pathway of $\dot{\text{O}}\text{CH}_2\text{OCH}_2\dot{\text{O}}$ is the cleavage of C-O bond on the central O atom, producing CH₂O and a new biradical $\dot{\text{O}}\text{CH}_2\dot{\text{O}}$ (R19), whose fate has been described in R10 to R13 above. The calculations indicated that R18 should be the favored pathway of SOZ biradical over R19 for its 72.2 kcal/mole exothermicity, while R19 is 33.3 kcal/mole endothermic instead [41].



2.3 Latest Outreach to Ozone Initiated Low-Temperature Oxidation of C₂H₄

Very recently, investigations on O₃ initiated C₂H₄ oxidation at low temperatures using a jet-stirred reactor (JSR) were reported by Roussos et al. [65, 66]. In their kinetic experiments, the approximate concentrations of reactants were chosen to be 2% C₂H₄, 12% O₂ and 86% Ar with 1000 ppmv O₃ addition. The residence time in the JSR was 1.3 s and the reactor pressure P = 700 torr. By coupling the JSR with the photoionization mass spectrometry on Chemical Dynamics Beamline of the Advanced Light Source (ALS) at Lawrence Berkeley National Laboratory, the mole fractions of the reactants C₂H₄ and O₃, together with the major ozonolysis products CH₂O were quantified and demonstrated in Figure 2.5.

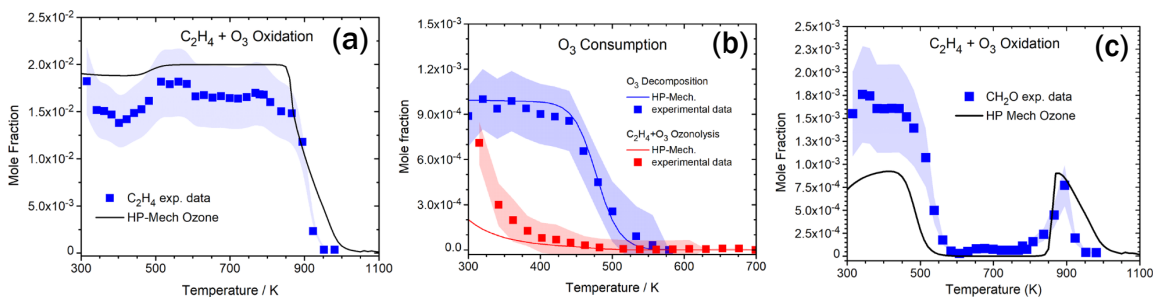


Figure 2.5. The measured mole fractions of (a) C₂H₄, (b) O₃ and (c) CH₂O from T = 300 K to 1100 K and P = 700 torr, with initially 2% C₂H₄, 12% O₂, 1000 ppmv O₃ and residence time of 1.3 s in the JSR. (from Ref. [65])

The HP-Mech [67, 68] was used as the base kinetic model for simulation and the numerical results were overlaid in Figure 2.5. Due to the complexity and uncertainty of ozonolysis reaction as described in Chapter 2.2, the reaction of $C_2H_4+O_3$ was described by a highly simplified 4-channel global reaction model from R20a to R20d as following,



Nevertheless, the apparent discrepancies can be seen in Figure 2.5 for all three measure species between experiment and simulation, at low to intermediate temperature range below $T = 700$ K. This outcome strongly indicates the inaccuracy in the kinetic model regarding O_3 initiated C_2H_4 oxidation especially at these temperatures. On the other hand, reasonable agreements were reached at intermediate to high temperature range, where most reactant O_3 was decomposed upstream of the reactor in the gas line and the ozonolysis reaction was greatly weakened.

In addition to the well-recognized ozonolysis products of C_2H_4 , some new species such as methyl hydroperoxide (CH_3OOH), ethyl hydroperoxide (C_2H_5OOH), acetaldehyde (CH_3CHO) etc., were experimentally characterized in such a low-temperature oxidation system. The corresponding mole fraction profiles with temperature were shown in Figure 2.6. Although no further information was given regarding the potential formation pathways

of those newly detected species, it should be reasonably proposed that they are generated by secondary reactions following the $C_2H_4+O_3$.

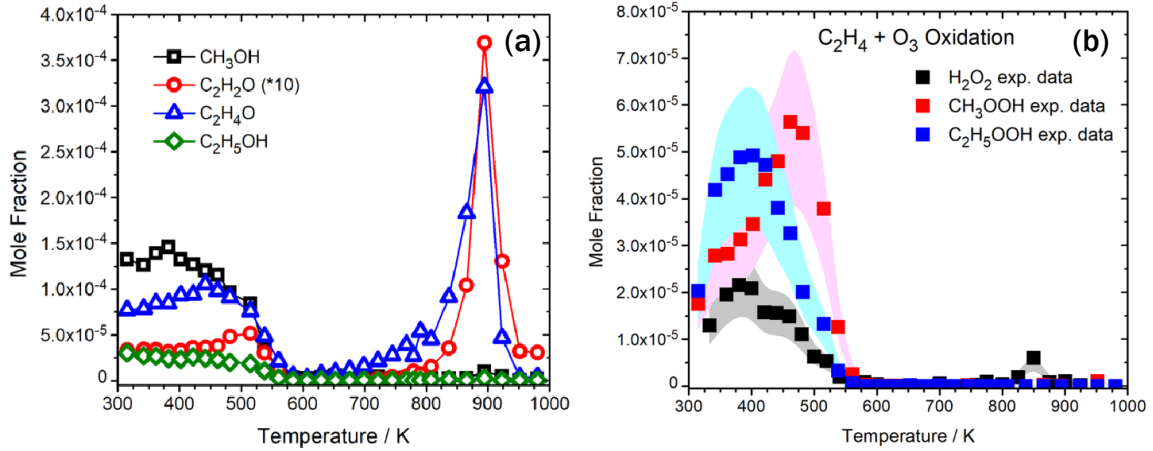


Figure 2.6. The mole fractions of (a) some oxygenated species and (b) hydroperoxides from $T = 300$ K to 1000 K and $P = 700$ torr, with initially 2% C_2H_4 , 12% O_2 , 1000 ppmv O_3 and residence time of 1.2 s in the JSR. (from Ref. [65])

2.4 Effect of Ozone Addition on Flame Speed

2.4.1 Saturated Fuels

With experiments using both premixed and non-premixed flame configurations, considerable increases in S_L of saturated fuels have been observed consistently with O_3 addition. In a study regarding CH_4 by Wang et al. [10], the improvement in S_L by O_3 was accurately quantified using a premixed heat flux burner at atmospheric pressure. The results are presented in Figure 2.7(a) and (b) at ranging equivalence ratios and O_3 addition levels. The burning velocity enhancement was plotted against concentrations of added O_3 in Figure 2.7(a), where the enhancement was defined as

$$\eta = \left(\frac{S_L^{O_3} - S_L^0}{S_L^0} \right) \times 100 \%$$

It is clearly demonstrated that more noticeable enhancement appears for fuel lean than the fuel rich case, as well as the off-stoichiometric than the stoichiometric case. Besides, a linear dependency could be observed between the flame speed enhancements and the amounts of seeded O_3 . With approximately 7000 ppmv O_3 addition in the mixture, the enhancement in S_L at equivalence ratio of $\phi = 0.65$ was measured around 16%.

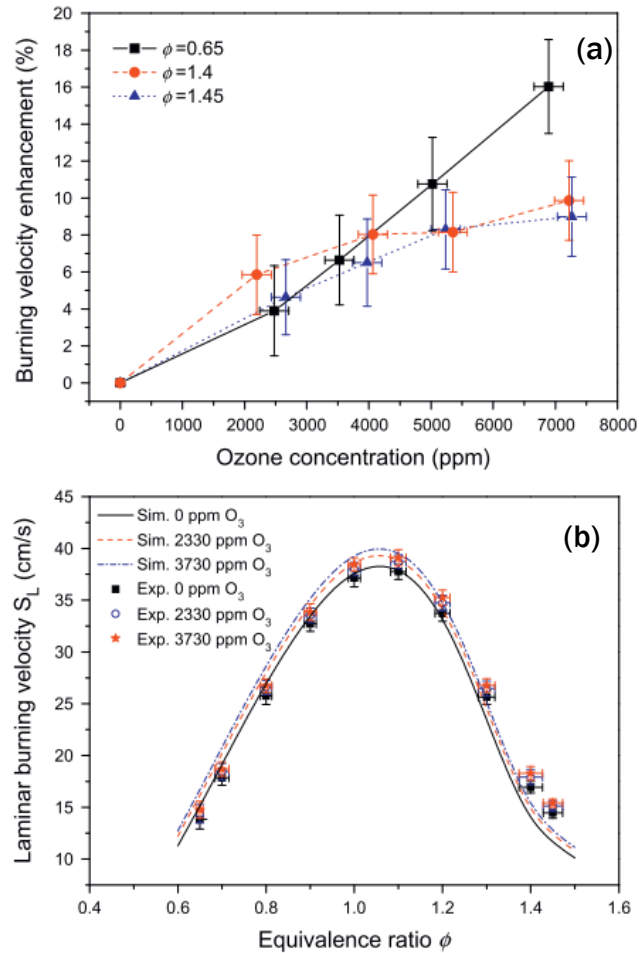


Figure 2.7. Laminar flame speeds of CH_4 at (a) different ϕ with ranging O_3 concentrations, and (b) different O_3 additions with ranging ϕ . Measurements were conducted using a premixed heat flux burner at atmospheric pressure. (from Ref. [10])

The GRI-Mech 3.0 [69] was used and combined with the O_3 related sub-mechanism for simulations. As shown in Figure 2.7(b), agreements were achieved between numerical

and experimental results at all O_3 levels and stoichiometries, indicating reasonable accuracy in the kinetic model. It was concluded that by adding O_3 into the mixture, its decomposition in the preheat zone of the flame directly brings extra \dot{O} radicals, which would not only initiate chain propagating reactions from CH_4 , but also help the production of other radicals such as \dot{H} and \dot{OH} in chain branching process. All these free radicals could kinetically accelerate the chain reactions and therefore increase the burning velocity.

As one of the most promising alternative fuels, study regarding the effect of O_3 addition on syngas flame [11] has been reported. The S_L enhancement was measured using the mixture of 15% H_2 , 15% CO and 70% N_2 as fuel at atmospheric pressure in a premixed heat flux burner. Similar results like CH_4 were obtained and shown in Figure 2.8. Simulations were performed with GRI-Mech 3.0 [69] and O_3 sub-mechanism.

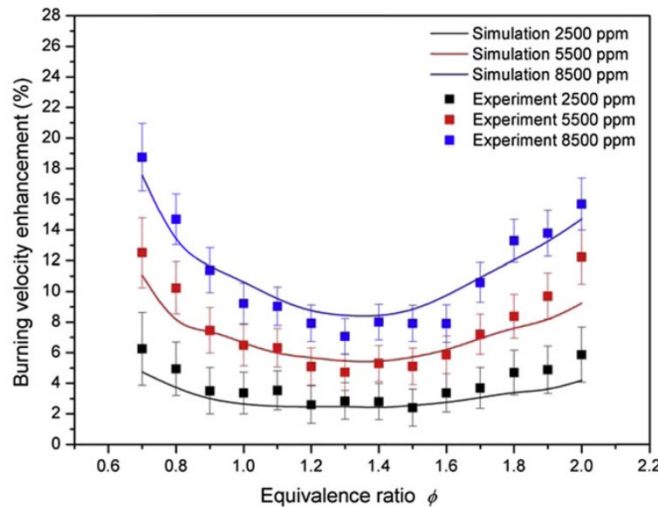


Figure 2.8. The flame speed enhancements of syngas and air with O_3 additions. Measurements were conducted using a premixed heat flux burner at atmospheric pressure. (from Ref. [11])

The largest enhancement in S_L of 18.74% was observed at equivalence ratio $\phi = 0.7$ with 8500 ppmv O_3 addition. The \dot{O} radical production via O_3 decomposition as well as the

corresponding radical density increase were recognized as the major reason for the enhancement in burning velocity.

Another example was reported by Ombrello et al. [8]. The effect of O_3 addition on flame speed of propane (C_3H_8) was investigated in a non-premixed configuration at atmospheric pressure. In their study, steady non-premixed lifted jet flames of C_3H_8 were established with 18% O_2 +82% N_2 as the co-flow in laminar regime. The dynamic balance between the lifted flame propagation and cold jet upstream makes the liftoff height (H_L) a sensitive indicator to any change in the flame speed. The results with and without O_3 addition in co-flow are shown in Figure 2.9.

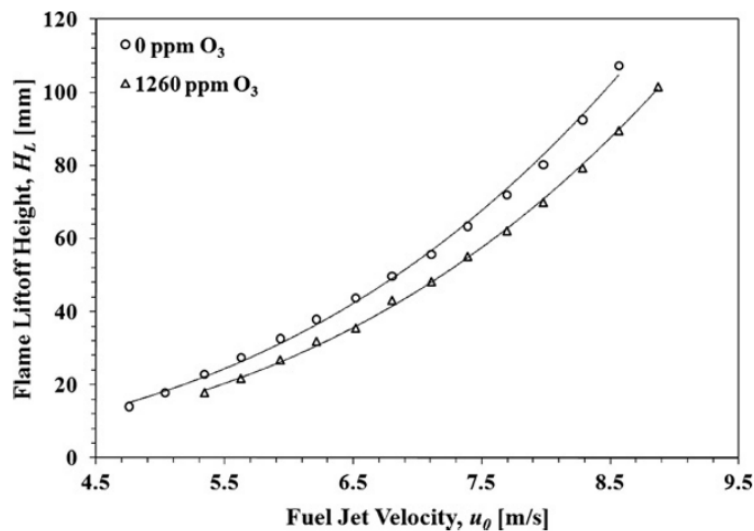


Figure 2.9. The change in liftoff heights of non-premixed laminar C_3H_8 lifted flame with O_3 addition at atmospheric pressure. (from Ref. [8])

The largest overall enhancement in flame speed was recorded around 8% with 1260 ppmv of O_3 addition. In addition to the kinetic enhancement caused by O_3 decomposition and other chain branching reactions involving O_3 as shown in premixed cases, the authors further proposed that the coupled enhancement in hydrodynamics at the triple flame front

would contribute to the observed H_L decrease as well. By plotting the results with different fuel jet velocities as shown in Figure 2.10, it was demonstrated that the higher the mixture fraction gradient, or the flow stretch, the higher the increase in flame speed enhanced by O_3 addition. Strong entanglement between chemical kinetics and transportation was presented in the flame liftoff and stabilization.

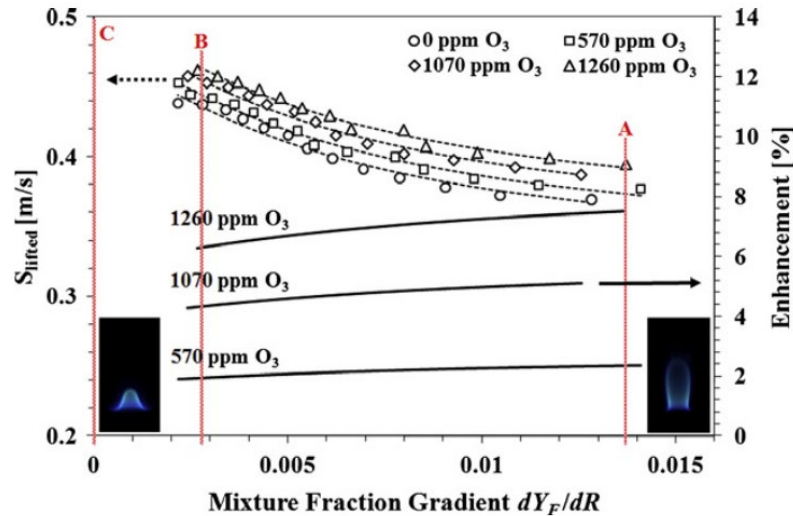


Figure 2.10. Flame speeds and enhancements with O_3 addition of laminar C_3H_8 lifted flame as function of mixture fraction gradient. (from Ref. [8])

2.4.2 Unsaturated Fuels

Unlike the consistency in flame speed enhancement by O_3 addition for saturated fuels, the corresponding outcomes for unsaturated fuels are diverse and show strong dependency on experimental conditions. In a premixed Bunsen burner configuration, Gao et al. [12] reported both detrimental and beneficial effects of O_3 addition on the flame speed of C_2H_4 in air. At room temperature and atmospheric pressure, decrease in S_L were measured with 6334 ppmv of O_3 added into the mixture of C_2H_4 +air for all equivalence ratios, as shown in Figure 2.11.

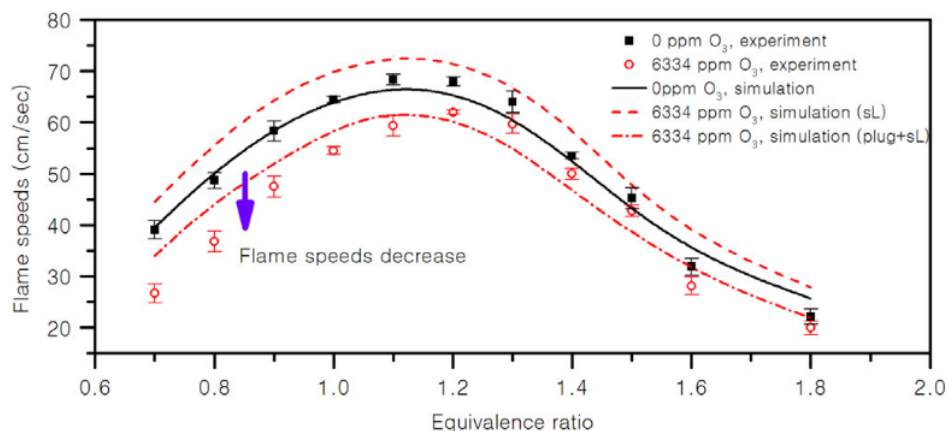


Figure 2.11. Effect of O₃ addition on flame speed of C₂H₄ in air at room temperature and atmospheric pressure. (from Ref. [12])

To explain this phenomenon, simulations were performed using USC Mech II [70] and O₃ sub-mechanism [10] as the kinetic model, where the ozonolysis of C₂H₄ was modelled by the reactions of R20a to R20d. It was rationalized that the decrease in flame speed with O₃ addition was really caused by the energy dissipation to burner wall within the mixing section, due to the highly exothermic reaction of C₂H₄+O₃. Such detrimental effect from O₃ addition could be qualitatively reproduced by simulations of an isothermal flow reactor connected upstream of the flame speed calculator. By cooling the unburned gas mixture down to T₀ = 200 K in a liquid N₂ bath, the ozonolysis reaction was strongly suppressed at given residence time. Consequently, flame speed enhancement was observed with O₃ addition as presented in Figure 2.12. The simulations indicated that the enhancement in S_L was given by the O₃ decomposition in preheat zone of flame, which was aligned with the cases of saturated fuels. The released \dot{O} radical from O₃ would attack C₂H₄ via the chain branching reaction $C_2H_4 + \dot{O} \rightarrow \dot{C}H_3 + \dot{H}C\dot{O}$, and therefore the flame speed was accelerated.

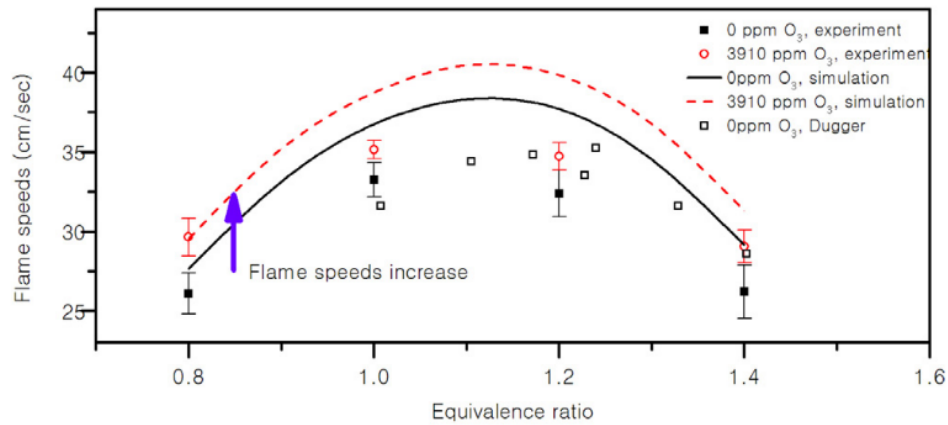


Figure 2.12. Effect of O₃ addition on flame speed of C₂H₄ in air at unburned gas mixture T₀ = 200 K and atmospheric pressure. (from Ref. [12])

In a similar research [19] using premixed Bunsen burner, reduction in flame speeds were observed for both C₂H₄ and acetylene (C₂H₂) by partially ozonizing the combustor air at atmospheric pressure. The direct photographs of laminar premixed flames of C₂H₂+air with and without O₃ addition are shown in Figure 2.13.

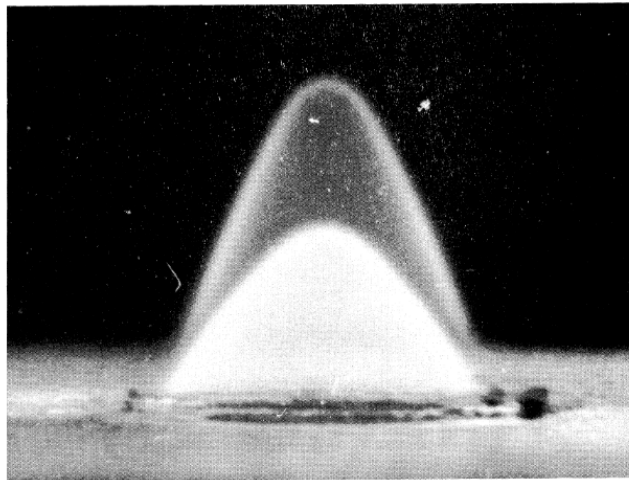


Figure 2.13. Premixed Bunsen burner flames of C₂H₂+air at atmospheric pressure. The air was partially ozonized in the upper flame. (from Ref. [19])

The comparison between pictures of two flames clearly showed that with around 1% O₃ added into the combustor air, the flame immediately became longer with steeper

slope, which suggested the reduction in S_L . It was proposed by the authors that the decrease in flame speed with added O_3 for both C_2H_4 and C_2H_2 cases was caused by the heat loss from ozonolysis reaction during non-adiabatic mixing process. Furthermore, they argued that the mixture with added O_3 would be shifted from pure fuel and air into a combination of fuel and partially oxidized products, which may further lower the overall burning velocity.

In contrast to the two examples above where the flame speed of C_2H_4 decreased with O_3 addition at atmospheric pressure, Pinchak et al. [20] reported enhancement in flame speed using premixed Hencken burner as the platform at $P = 80.3$ torr and $\phi = 1$. The PIV measurements with and without O_3 addition are demonstrated in Figure 2.14.

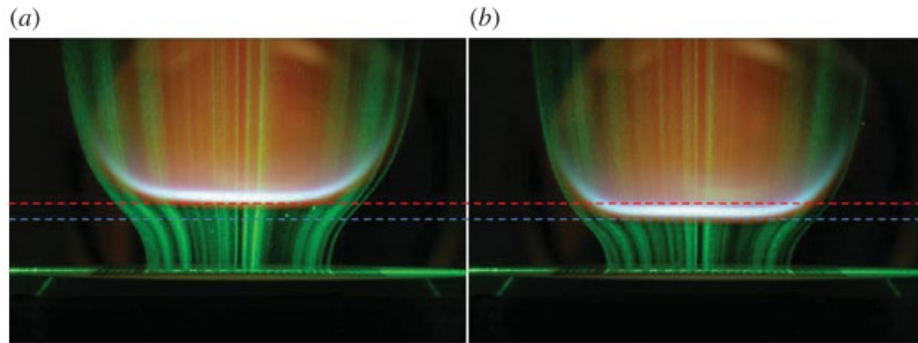


Figure 2.14. PIV measurements of premixed C_2H_4 and synthetic air (a) without and (b) with 11000 ppmv O_3 addition at $P = 80.3$ torr and $\phi = 1$. (from Ref. [20])

It was pointed out that the lowered pressure would dramatically increase diffusivity and result in small gradient and even distribution at the burner exit, so that the nearly 1-D flame could be stabilized at considerable H_L . It was also reported that being similar to the non-premixed lifted flame study of C_3H_8 by Ombrello et al. [8], greater flame speed enhancements were observed at higher axial stretch rate. With 11000 ppmv O_3 addition, an

averaged 7% increase in flame speed was recorded under moderate stretch rate. From the chemical kinetic point of view, the sub-atmospheric pressure gave brief residence time upstream of the flame, under which the ozonolysis of C₂H₄ could be virtually negligible. However, instead of the O₃ decomposition giving \dot{O} radicals, the simulations implied that at P = 80.3 torr, the chain propagating reaction between O₃ and \dot{H} in the flame preheat zone, $O_3 + \dot{H} \rightarrow \dot{O}H + H_2O$, contributes dominantly to the flame speed enhancement via abundant heat release.

CHAPTER 3. EXPERIMENTAL APPROACHES

3.1 Overview

In this chapter, the experimental methods and corresponding set-ups applied in this dissertation are presented. All chemical kinetic experiments are conducted based on a flow reactor scheme but coupling with different diagnostic techniques. At the early stage of the kinetic study regarding O_3 initiated C_2H_4 oxidation at room temperature, the experiments are mainly focused on exploratory purpose. The simple online sampling using a compact gas chromatography provides general information on the major products in the reaction system. These preliminary results lay the foundation for later detailed kinetic study using advanced synchrotron radiative photoionization molecular beam mass spectrometry (SRPI-MBMS), by which the detection of many reactive intermediates is possible. In addition to the intrusive methods, non-intrusive optical techniques are also used. To measure the global reaction rate constant of $C_2H_4+O_3$, an ultraviolet (UV) LED absorption system is built and tested. The effect of O_3 addition on C_2H_4 flame dynamics is investigated on a non-premixed jet flame platform, where series of stable C_2H_4 lifted flames are established in laminar regime with and without O_3 addition. The distribution of C_2H_4 ozonolysis reaction is visualized by using a low-frequency CH_2O planar laser induced fluorescence (PLIF) system.

3.2 Fast-Mixing Flow Reactor System

Being the core of the experimental kinetic study in this dissertation, the effort to improve the design of the flow reactor system has never ceased since 2017. Chronologically, two different versions of the flow reactor systems have ever been developed, which are differentiated by their fuel nozzle designs and the geometries of the reactor. Unlike traditional low-temperature fuel oxidation studies, where minor reaction would happen until the mixture of fuel and oxidizer being raised to a certain temperature, the rapid ozonolysis reaction under high reactant concentration necessitates prompt mixing, in order that the reaction times [71] could be well defined and reasonable spatial resolution may be obtained. For such a purpose, the new flow reactor system must run at non-premixed mode and achieve prompt mixing within the inlet region of the reactor. Numerically, ANSYS Fluent [72] is employed to aid the design of the flow reactor's geometry, and model the flow field and distribution of the reactants after mixing. Dimensional drawings of the components in designed flow reactor systems in this dissertation are provided in Appendix A for future reference.

3.2.1 Early Reactor Design (before 2018)

The very first design of the system is built based on a flow reactor with diverging section, whose drawing is given in Figure 3.1. The reactor itself is fabricated with fused-silica material so that any heterogeneous reaction on the wall could be efficiently prevented. In regard to the geometry, the flow reactor is 432.3 mm in total length with a 400 mm long test section, where most ozonolysis reactions are expected to happen. The inner diameter of the flow reactor is 12 mm and outer diameter is 14 mm. Upstream to the

test section, a diverging area with half angle of 5 degrees and 32.3 mm in length is designed to slow down the fuel and oxidizer mixture, which may ensure a steady and non-recirculated flow field in the test section. To enhance the mixing between fuel and oxidizer at ambient conditions, a commercialized, compact muffler in 304 stainless-steel is applied as the fuel injector and located at the mixing section of the system. From the muffler, the fuel species premixed with diluent would be released into the premixed oxidizer and diluent co-flow. The multiple outlets around the muffler body could greatly improve the uniformity of fuel injection in the radial direction. The assembly of the very first fast-mixing flow reactor system is demonstrated in Figure 3.2, in which both test and mixing sections are marked.

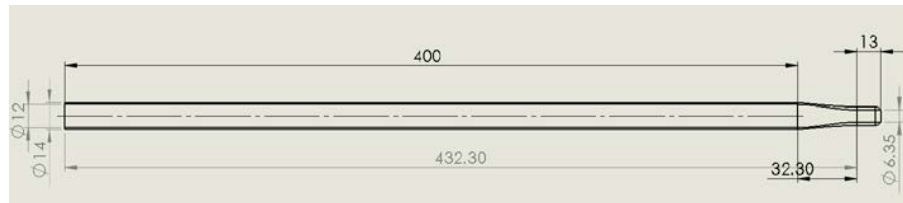


Figure 3.1. The geometry and dimensions of the very first flow reactor design.

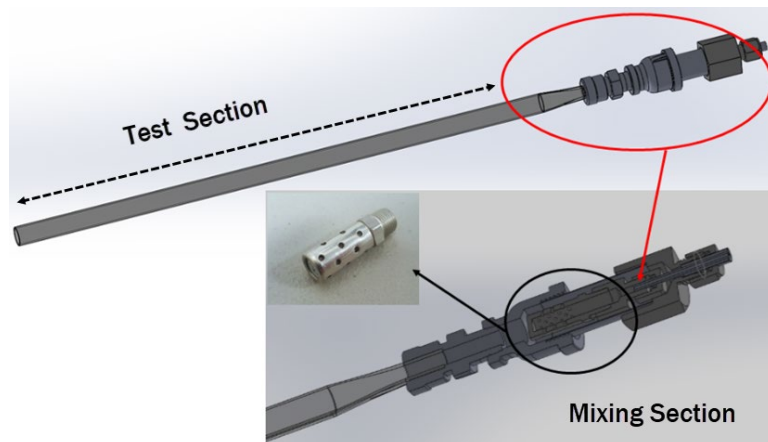


Figure 3.2. The assembly of the very first fast-mixing flow reactor system. The picture of compact 304 stainless-steel muffler as fuel injector is inserted.

This design is examined with 3-D non-reacting laminar flow simulation using Fluent [72]. The results are presented in Figure 3.3. It can be noticed that all three reactants, C_2H_4 , O_2 and O_3 are evenly distributed in the test section.

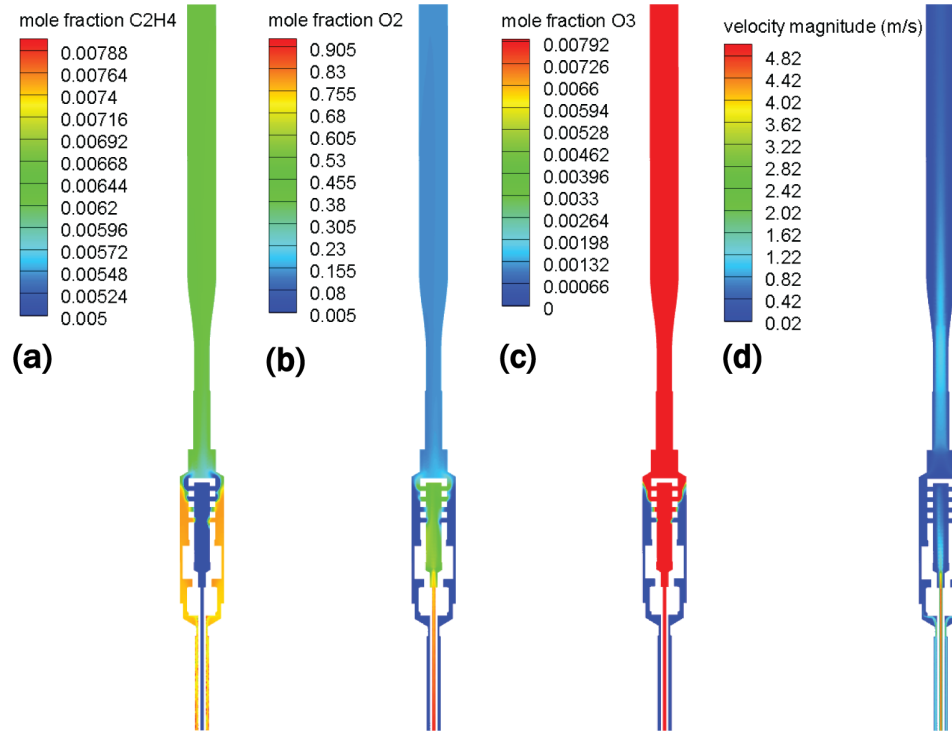


Figure 3.3. Numerical examination of the very first flow reactor system design. Non-reacting laminar flow results of (a) mole fraction of C_2H_4 , (b) mole fraction of O_2 , (c) mole fraction of O_3 and (d) velocity magnitude.

Although the simulation has shown reasonably mixing between fuel and oxidizer, however, in this design, the long diverging area between mixing and test section would result in too long residence time before sampling. Besides, a more severe problem is that the non-streamlined body of the muffler would cause a major recirculation zone being attached to the blunt head, which may sabotage the products measurement. Therefore, revisions are required for both reactor and fuel injector design.

First, to eliminate the undesired recirculation zone caused by the blunt body, a stainless-steel nosecone with half angle of 22 degrees is directly welded at the end of muffler. Second, to reduce the residence time between mixing and sampling, the flow reactor is redesigned, and a converging-diverging (C-D) section is added. The modified fuel injector is placed specifically at the contracted region to ensure a fully contact between fuel and oxidizer streams. In addition to the modification in shape, a larger diameter is adopted for the flow reactor, which the inner diameter is increased to 22 mm and the outer diameter is increased to 25 mm. With such revisions in both reactor and fuel injector, sampling is now capable immediately downstream of the muffle nosecone, which is equivalent to a further reduction in the mixing time. The schematic of the revised flow reactor system assembly together with the photo of modified fuel injector are shown in Figure 3.4.

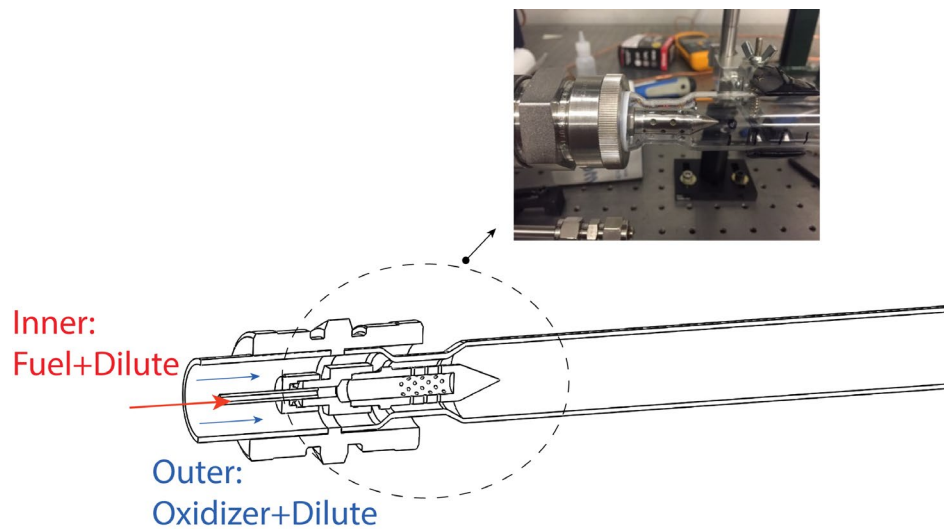


Figure 3.4. Schematic of revised fuel injector and flow reactor assembly, the photograph of modified fuel injector in position is inserted.

The numerical results of examination on this revised design are shown in Figure 3.5. It is clearly demonstrated in Figure 3.5(a) and (b) that the addition of nosecone to the

original muffler successfully removes the recirculation zone and delivers a much more uniform flow field downstream in the test section. Additionally, Figure 3.5(d) shows an example that at a given flow rate, the possible minimum mixing time could be less than 20 ms if samples are taken immediately downstream of the injector nosecone, where reasonable mixing between fuel and oxidizer has been completed.

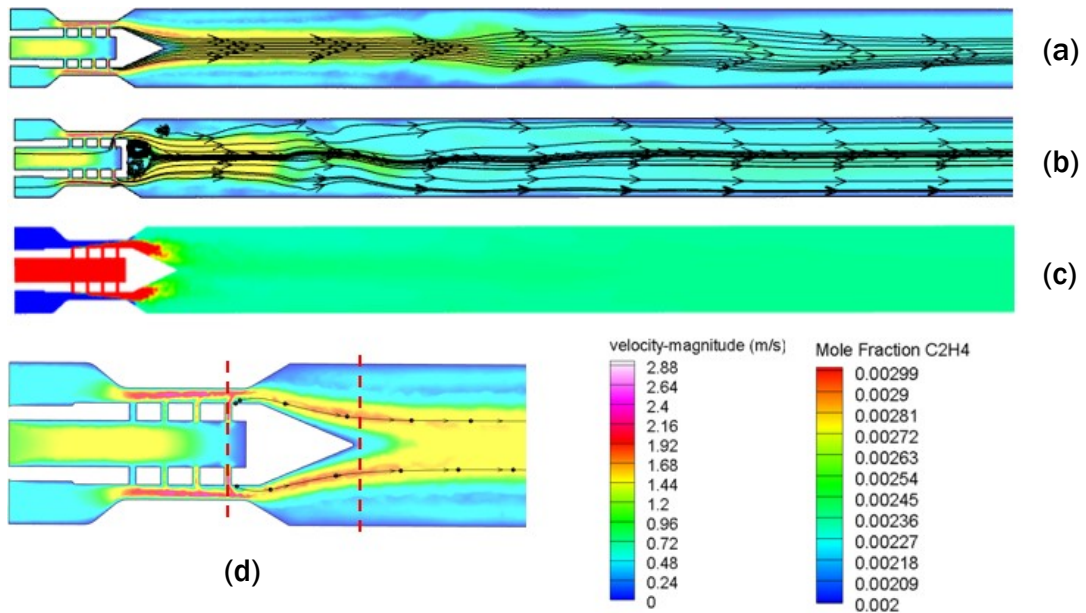


Figure 3.5. Numerical examination of revised flow reactor system. (a) Velocity field and streamlines using modified fuel injector, (b) velocity field and streamlines using original muffler with blunt head as fuel injector, (c) non-reacting C₂H₄ distribution and (d) mixing time estimation, time interval 5 ms between each dot.

3.2.2 Mixing Optimization

As stated previously, the primary goal of this new flow reactor system is to realize online fast mixing at ambient conditions. Based on the design as shown in Figure 3.4, the fuel and oxidizer species are mixed in laminar cross-jet configuration. The concept is illustrated in Figure 3.6. Under such scenario, the penetration of injected fuel stream into the oxidizer crossflow predominantly controls the degree of mixing. Therefore, by

intentionally spreading uneven amounts of diluent in both fuel and oxidizer streams, the mixing between fuel and oxidizer can be optimized.

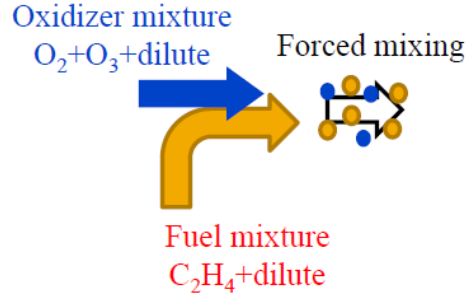


Figure 3.6. Mixing between fuel and oxidizer in laminar cross-jet configuration.

With the help of GC, the mixing between reactants can be evaluated experimentally under non-reacting condition, i.e., without O_3 addition. Here, a case with desired reactant mole fractions, $C_2H_4/O_2/O_3/N_2 = 2.2\%/9.4\%/0.2\%/balance$, is given as an example, using the revised flow reactor system in Figure 3.4. In order to determine the spreading ratio of diluent N_2 for optimized mixing, the GC first performs sampling at the outlet of the flow reactor to measure the mole fractions of C_2H_4 and O_2 , denoted as $\chi(C_2H_4)_{homogeneous}$ and $\chi(O_2)_{homogeneous}$, respectively. At this location, the mixture is undoubtedly homogeneous already. Next, the same measurement is performed right downstream to the fuel injector nosecone, where the mole fractions of C_2H_4 and O_2 are denoted to be $\chi(C_2H_4)_{injector}$ and $\chi(O_2)_{injector}$, respectively. By comparing the two measurements, if $\chi(C_2H_4)_{injector} > \chi(C_2H_4)_{homogeneous}$, then more N_2 is given in the fuel stream meanwhile less in the oxidizer stream, and vice versa. Once $\chi(C_2H_4)_{homogeneous} \approx \chi(C_2H_4)_{injector}$ (or O_2 equivalently) is achieved, the mixing in the flow reactor is optimized. With the seeded O_3 much less than O_2 during kinetic experiments, the impact of O_3 addition on global mixing

should be expected quite limited. In Figure 3.7 the measured mole fractions of C_2H_4 and O_2 along the flow reactor centerline, before and after optimization process, are plotted respectively. The zero position corresponds to the nosecone of the modified fuel injector.

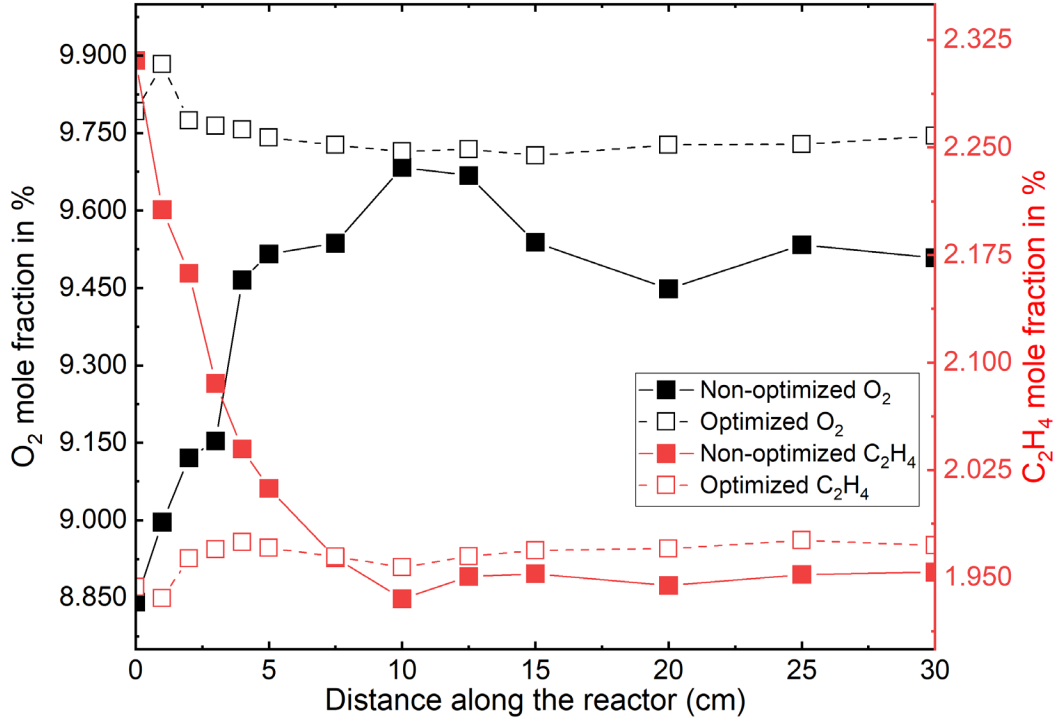


Figure 3.7. Comparison of GC measured mole fractions of C_2H_4 and O_2 along the flow reactor centerline before (solid symbols) and after (open symbols) mixing optimization. No O_3 is added.

The measurements above clearly illustrate a much more uniform distribution along the flow reactor is obtained for both C_2H_4 and O_2 after the optimization, which indicates reasonable online mixing can be successfully achieved by this revised design. Before the kinetic experiments are carried out, as part of the inlet boundary determination, such mixing optimization would be performed numerically using Fluent [72] at each given condition. The spreading ratios of diluent between fuel and oxidizer streams obtained numerically would be later applied in the reacting experiments.

3.2.3 Latest Reactor Design (after 2018)

However, one minor issue on the revised design in Figure 3.4 is the inconvenience in flow residence time adjustment within the reactor. Since the fuel injector is restricted at the C-D section for best mixing performance, to modify the flow residence time, one could only either change the length of the reactor or use a different set of flow rates of fuel and oxidizer streams. Therefore, another new reactor system built on flow tube with constant diameter is proposed.

Being similar to previous designs in concept, the new flow reactor system comprises two major components. The first one is a straight fused-silica tube with constant inner diameter of 12 mm as the flow reactor. The second component is a specifically designed fuel injector assembly with 20 outlets (injector outer diameter 10 mm, outlet diameter 0.5 mm each) evenly distributed throughout the circular positions. A nosecone with half-angle of 11 degrees is attached at the end of the injector to ensure a uniform flow field downstream. The support ring (outer diameter 12 mm) with 20 thorough holes (diameter 0.5 mm each), each of them is perpendicularly paired with the outlet on the injector body, so that 20 small cross-jets of fuel and oxidizer are established, which consequently enhance the mixing. During experimental operations, premixed C_2H_4 /diluent is radially sprayed into the oxidizer crossflow of premixed O_2/O_3 /diluent. The existence of the support ring secures the coaxiality of fuel injector and the flow tube. By simply moving the injector assembly along axial direction, the flow residence time can be easily adjusted without changing the flow rates. A detail demonstration to the 20-outlets fuel injector assembly in perspective view, and the flow paths of fuel and oxidizer streams are shown in Figure 3.8(a) and (b), respectively.

(a)



(b)

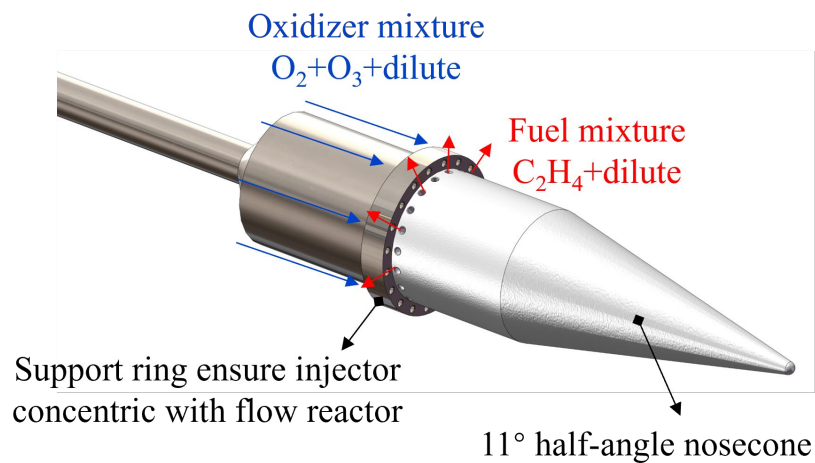


Figure 3.8. Demonstration to the newly designed 20-outlets fuel injector assembly of (a) perspective view and (b) the flow paths of fuel and oxidizer streams.

The schematic of the latest designed flow reactor system, together with direct photograph are presented as Figure 3.9(a) and (b) respectively. The head part of the fuel injector, i.e., the fuel outlets and nosecone, is made with polytetrafluoroethylene (PTFE)

to allow flexible manufacturability meanwhile to ensure strong chemical-resistance during O_3 experiments.

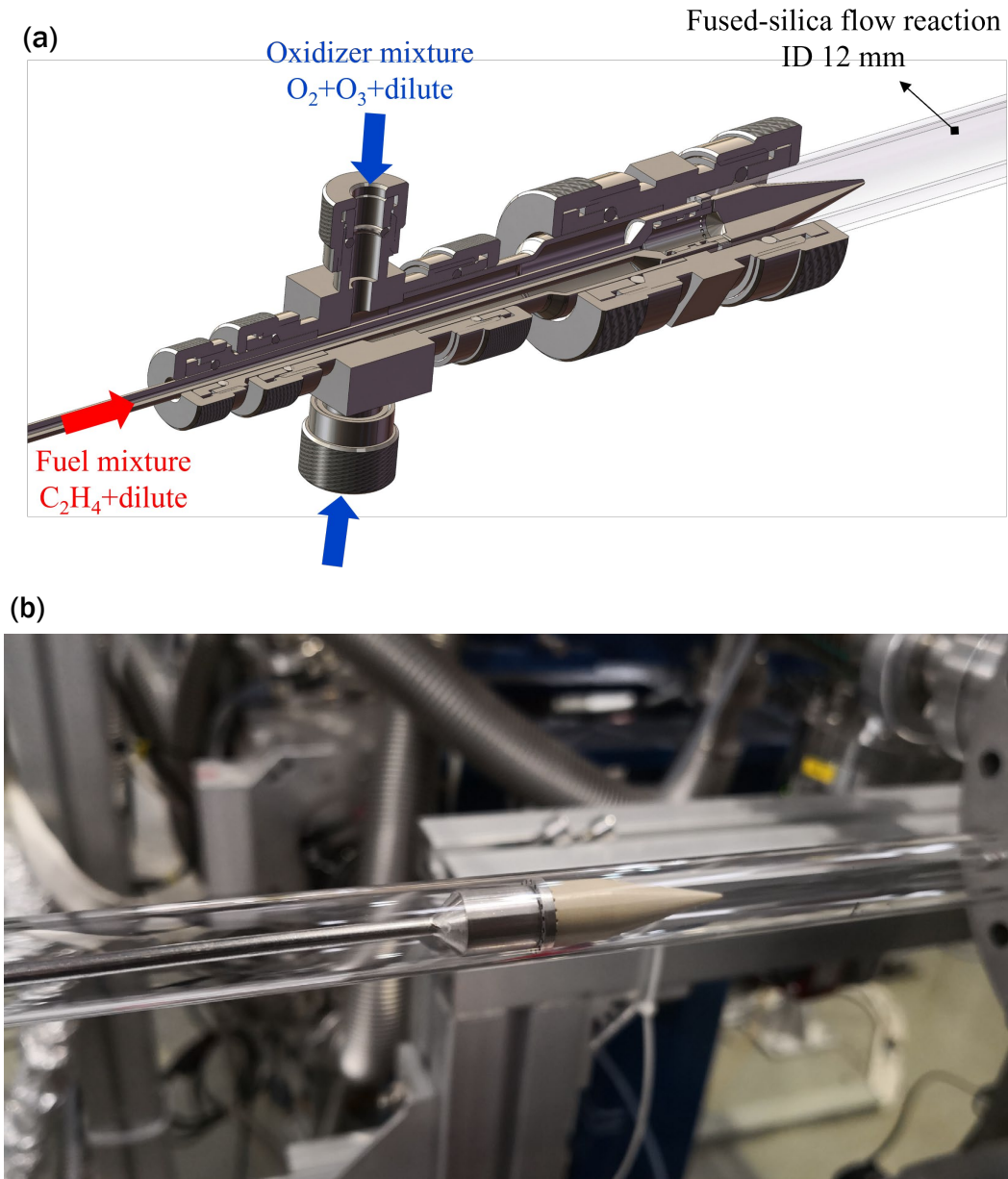


Figure 3.9. The latest design of fast-mixing flow reactor system with 20-outlets fuel injector of (a) schematic and (b) direct photograph.

With steady, non-reacting, 3-D numerical simulations using Fluent [72], this latest designed flow reactor system is assessed in regard to both flow field and degree of mixing.

An example is given here with the target mole fractions of $C_2H_4/O_2/O_3/argon(Ar) = 1.8\%/9.4\%/0.2\%/balance$, and the volumetric flow rates at the inlet of $C_2H_4/O_2/O_3/Ar = 40/206/4/1936$ standard cubic centimeters per minute (sccm). The computational domain and unstructured mesh are presented in Figure 3.10, in which both the inlets for fuel and oxidizer streams are velocity type, while the outlet of the reactor is set to have constant pressure of $P = 760$ torr.

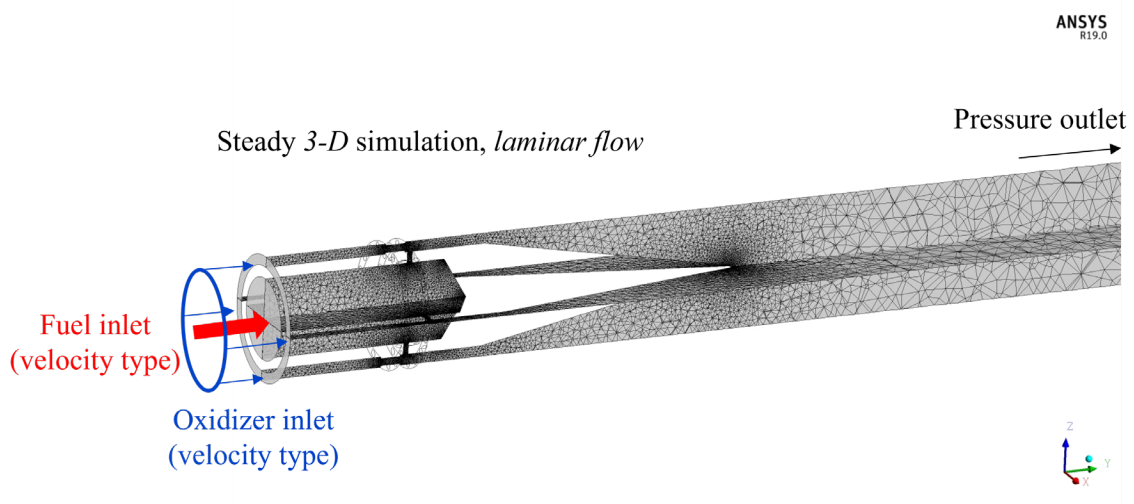


Figure 3.10. Computational domain and mesh in numerical simulation of the latest designed fast-mixing flow reactor system.

At $T = 300$ K and $P = 760$ torr, by spreading 37% of total diluent Ar into the fuel stream and the rest 63% into the oxidizer stream, the mixing between C_2H_4 and O_2/O_3 is optimized numerically. The spatial distributions of C_2H_4 and O_3 by non-reacting simulation are shown in Figure 3.11. The mole fraction distribution of C_2H_4 is given in the XY plane, and the distribution of O_3 is given in the YZ plane. It is obviously demonstrated that the two reactants are well-mixed already downstream of the nosecone of the fuel injector assembly.

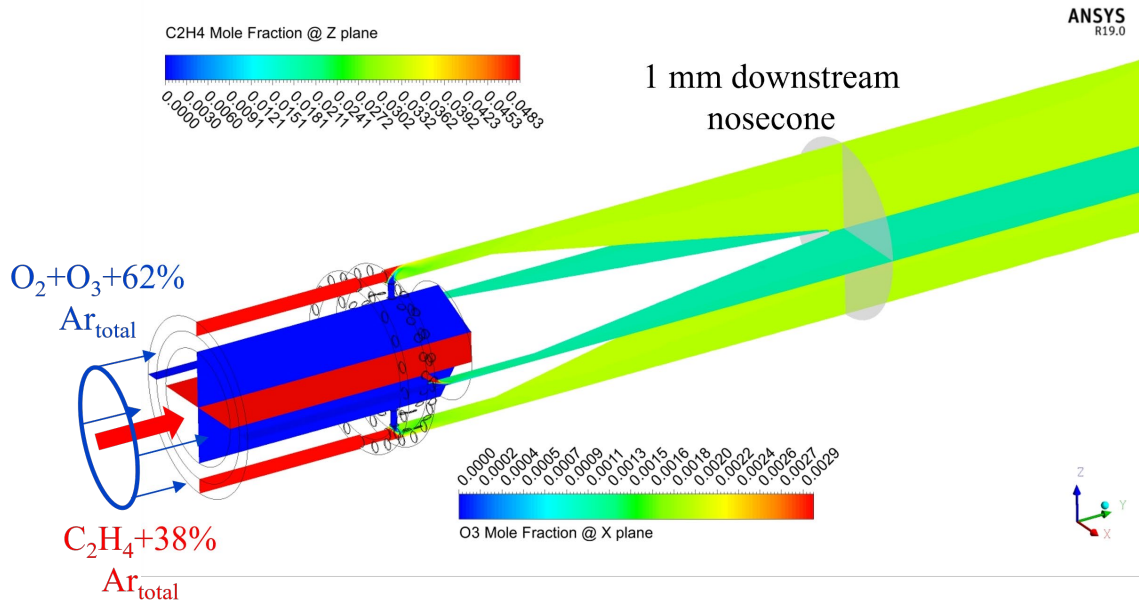


Figure 3.11. Simulated non-reacting mole fraction distributions of C₂H₄ (XY plane) and O₃ (YZ plane) of the latest designed flow reactor system, T = 300 K and P = 760 torr.

To better illustrate the degree of mixing quantitatively from the numerical results, the coefficient of variation, S , is calculated regarding species mole fraction, which is defined as

$$S = \frac{\sqrt{\sum_{i=1}^n \frac{(\chi_i - \bar{\chi})^2}{n - 1}}}{\bar{\chi}}$$

In the equation of S above, χ_i is the mole fraction of target species on a single computation node or element, and $\bar{\chi}$ is the mean value of groups of nodes or elements. By sampling on the Y cross-section 1 mm downstream of the fuel injector nosecone as noted in Figure 3.11, the theoretical mole fractions of C₂H₄ and O₃ without reaction are shown in Figure 3.12(a) and (b) respectively.

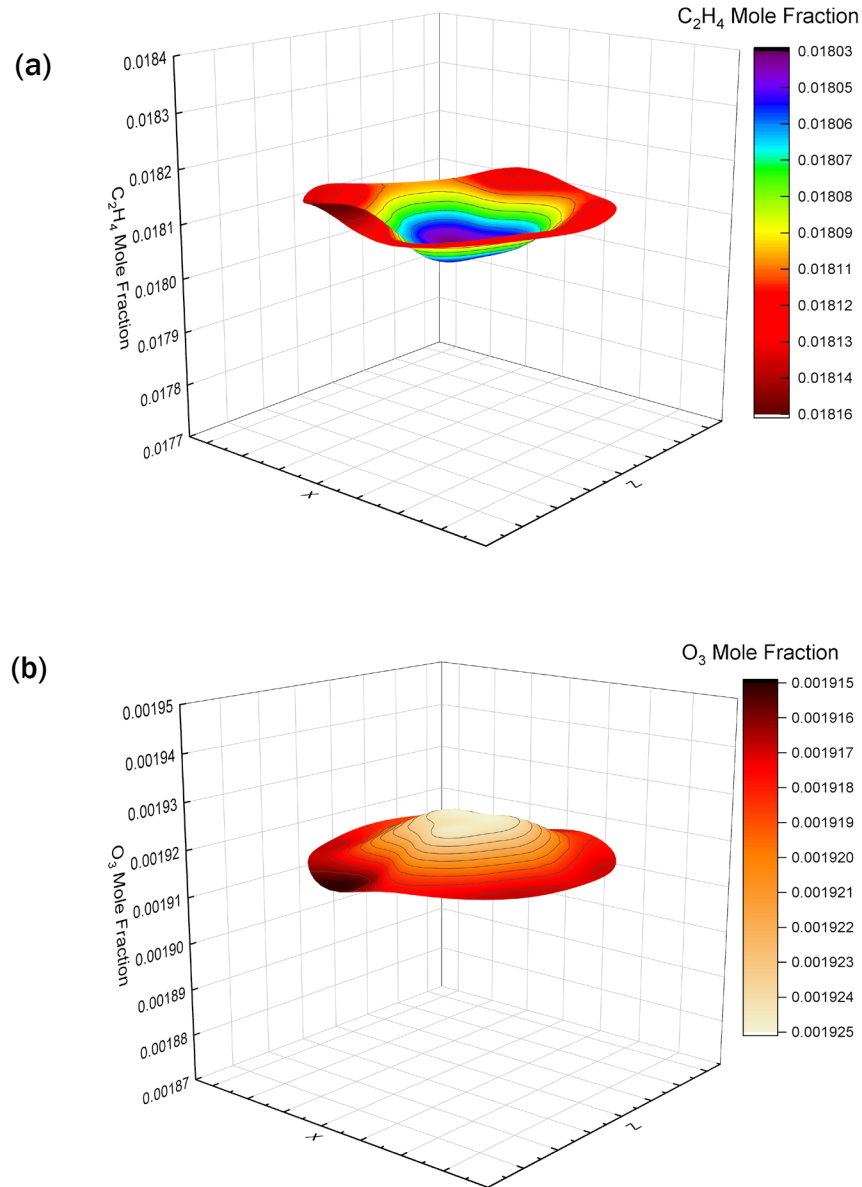


Figure 3.12. Simulated non-reacting mole fraction distributions of (a) C₂H₄ and (b) O₃ on Y cross-section 1 mm downstream of the fuel injector nosecone.

The calculated coefficients of variation are $S_{C_2H_4} \approx 2.73 \times 10^{-3}$ and $S_{O_3} \approx 1.74 \times 10^{-3}$ for the mole fractions of C₂H₄ and O₃ respectively on this cross-section. Generally, a mixture can be considered homogeneous if $S < 0.05$ is achieved. Therefore, it could be concluded that the latest designed flow reactor system is capable in online mixing. Regarding the flow field in the reactor, the result is shown in Figure 3.13 as following.

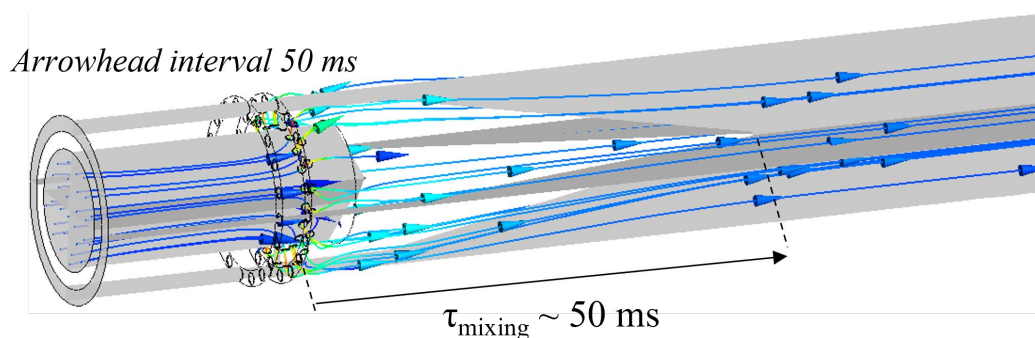


Figure 3.13. Non-reacting laminar flow field and streamlines by simulation of the latest designed flow reactor system.

From the simulated 3-D streamlines, no major recirculation is observed in the flow reactor and a uniform flow field is delivered downstream to the online fast mixing at the fuel injector assembly. At the given flow rates of $C_2H_4/O_2/O_3/Ar = 40/206/4/1936$ sccm, the mixing time from the fuel outlets to the injector nosecone is estimated in the order of 50 ms with averaged velocity magnitude of $U_{avg} = 0.352$ m/s in the test section.

3.2.4 Brief Notes on Designed Flow Reactor Systems

In this dissertation, both flow reactor systems in Figure 3.4 and Figure 3.9 have been deployed in the kinetic studies, but with different diagnostic methods applied. The choice of the reactor system can be made based on practical experimental conditions. For example, if the experiment is desired to be conducted under sub-atmospheric pressures, a reactor with larger diameter should be used to reduce wall quenching effect on transient intermediates, meanwhile, the mixing between fuel and oxidizer could be further enhanced by the lowered pressure. In fact, not only the kinetic studies relevant to the ozonolysis reaction, these fast-mixing flow reactor systems are eligible to be the platform for other gas-phase chemical kinetic studies as well. It is believed that by adding a heating jacket onto the flow tube (either quartz or metal), such reactor system could be used to investigate

the kinetics in traditional hydrocarbon oxidation at elevated temperatures as well. The suitable boundary conditions can be determined using numerical simulations with the mixing optimization procedure described in Chapter 3.1.2.

3.3 Gas Chromatography

To gain a general knowledge on the composition of major products in the O_3 initiated C_2H_4 oxidation at room temperature, the flow reactor system is directly coupled to a compact gas chromatography, model INFICON Micro GC Fusion® Gas Analyzer (sensitivity down to 1 ppm). The schematic of the GC experimental set-up is shown in Figure 3.14 and the direct photograph is shown in Figure 3.15.

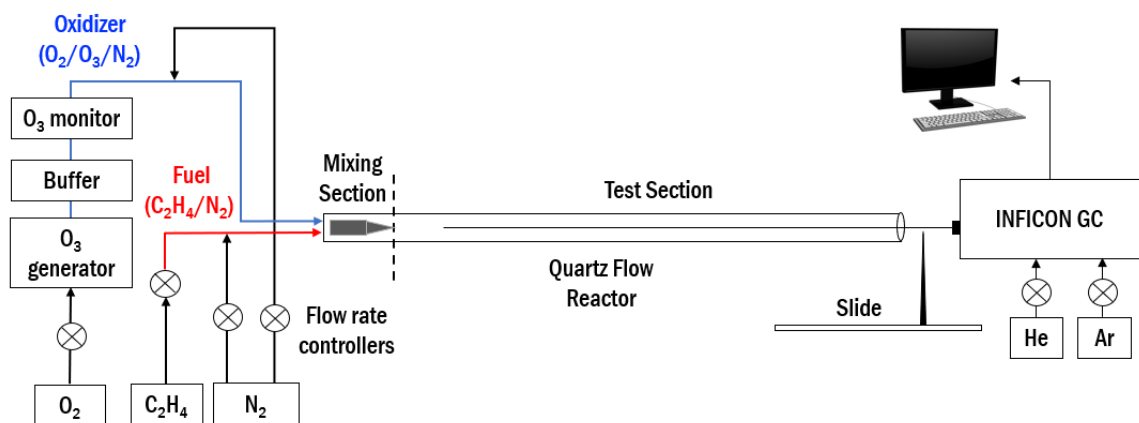


Figure 3.14. Schematic of experimental set-up of kinetic study using fast-mixing flow reactor system and gas chromatography.

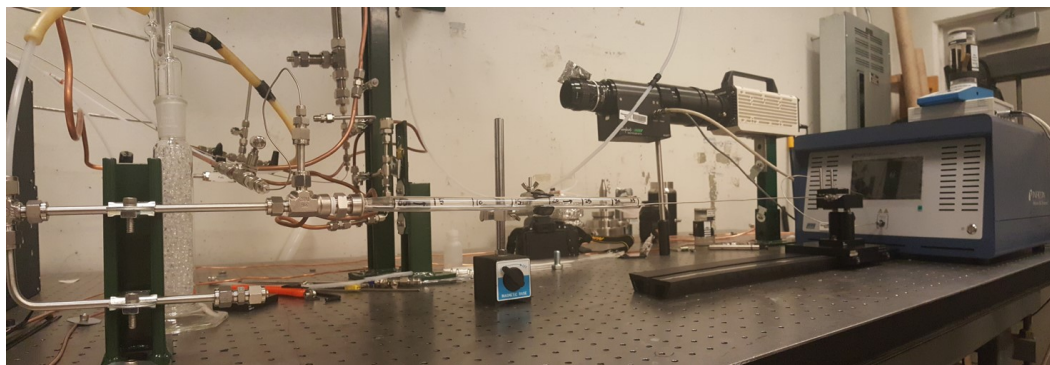


Figure 3.15. Direct photograph of coupling between INFICON GC and flow reactor system.

As presented in the schematic of Figure 3.14, the premixed fuel (C_2H_4/N_2) and oxidizer ($O_2/O_3/N_2$) streams are supplied separately by two gas lines. Ultra-high purity (UHP, 99.994% purity, Airgas) O_2 is provided to an ozone generator (Ozone solution model TG-40) for O_3 production, while an ozone monitor (Teledyne Instruments, Model 454, accuracy $\pm 1\%$ of full scale) is installed downstream to monitor the mass fraction of O_3 in O_2/O_3 mixture. An inline buffer with glass beads is inserted between the generator and the monitor to damp possible fluctuations in O_3 production. The volumetric flow rates of all gas supplies are regulated by precise orifices from O’Keefe Control in different sizes, which are routinely calibrated using the bubble flowmeter to ensure accuracy (around $\pm 5\%$ at supply pressure of 25 psig).

Table 1. Description of installed modules in the INFICON Micro GC Fusion® Gas Analyzer.

Module	Column	Detector	Carrier Gas
A	Rt-molecular sieve diameter 0.25 mm, length 10 m	TCD	Ar
B	Rt-Q-Bond diameter 0.25 mm, length 12 m	TCD	He
C	Rxi-1ms diameter 0.15 mm, length 20 m	TCD	He

A pre-cleaned 316 stainless-steel tubing with outer diameter of 1.59 mm (1/16 inch) is used for in-situ sampling at the test section in the flow reactor. The stainless-steel probe is secured on a slide so that sampling along the flow reactor at different axial positions is possible. The INFICON GC requires UHP Ar and helium (He) as carrier gases for three different modules, whose descriptions are listed in Table 1. During experiments, the gas taken through the sampling probe would flush all three GC modules simultaneously for detection and analyzing.

For those common gaseous species at ambient conditions, the GC is calibrated using commercial calibration standards provided by Cal Gas Direct. However, for those species who have low saturated vapor pressure or in liquid-phase at room temperature, such as HCOOH or methanol (CH₃OH), the calibrations are performed by evaporating small amount of known purity liquid standards. With the feed rate of liquid standard being accurately controlled by a syringe pump (Harvard Apparatus PHD ULTRA), together with given volumetric flow rate of inert gas, which is heated up above the boiling point of that substance, a gaseous calibration standard can be prepared online quantitatively. Although negative effect from the formation of dimer, for instance, formic acid dimer ([HCOOH]₂), has been reported on GC calibration, here it would be just neglected.

3.4 UV LED Absorption Measurement

3.4.1 Introduction and Set-up

To measure the global rate constant of reaction $C_2H_4+O_3$ at room temperature and atmospheric pressure, a LED based UV absorption system is built for non-intrusive O_3 measurement along the flow reactor. Summarized by Gorshelev et al. [73] from different literatures, the measured cross-sections of O_3 absorption at room temperature are shown in Figure 3.16.

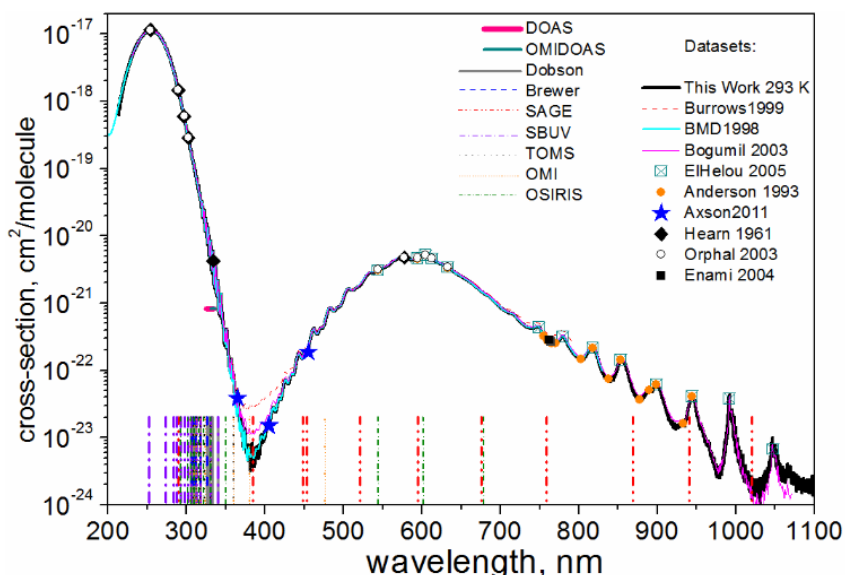


Figure 3.16. Summary of measured O_3 absorption cross-sections at room temperature. (from Ref. [73])

In the wavelength range of 200 nm to 1100 nm, it is obvious that the strongest absorption occurs in between 200 nm and 300 nm, which is known as the Hartley band of O_3 absorption and has been widely adopted in O_3 detection and monitor. Meanwhile, the major products from C_2H_4 ozonolysis reaction, i.e., CH_2O [74], CO_2 [75, 76], CO , H_2O and H_2 , together with C_2H_4 itself, have been experimentally determined transparent within

200 and 1100 nm. A more detailed demonstration to the cross-sections of O₃ absorption in Hartley band at room temperature is given in Figure 3.17. It plainly shows that the peak of absorption locates near 255 nm, which is therefore implemented for O₃ measurement in this work.

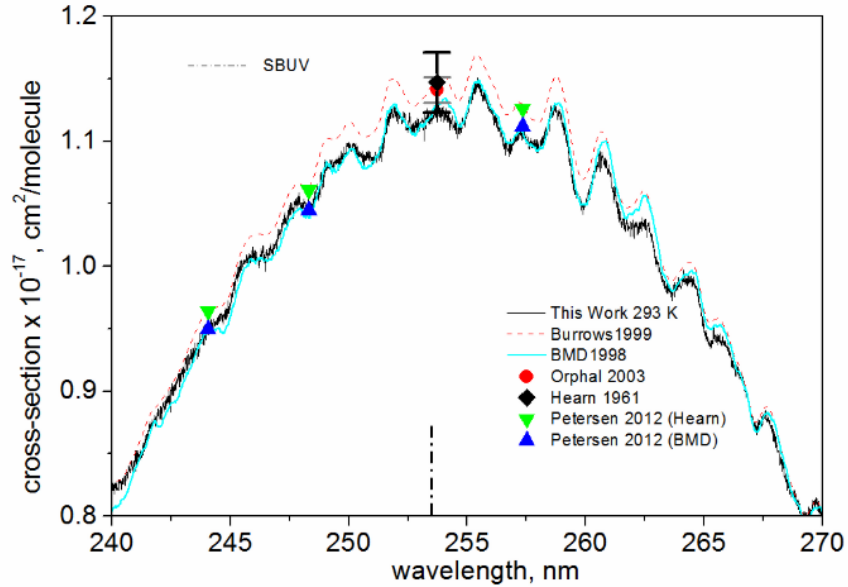


Figure 3.17. Measured cross-sections in Hartley band of O₃ absorption at room temperature. (from Ref. [73])

A simple UV LED (model LED255J, Thorlabs) at 255 nm with built-in ball lens is used as the light source, whose specifications can be found in Table 2.

Table 2. Specifications of Thorlabs LED255J.

Peak Wavelength	255 nm
Bandwidth (FWHM)	12 nm
Viewing Half Angle	7.5 degrees
Operating Current	100 mA
Optical Output Power @ 100 mA	1 mW

To minimize the output fluctuation during experiments, the power supply to the LED is controlled by a LED driver (T-Cube LED Driver, Thorlabs) at constant 100 mA, and a multimeter is connected in tandem between the driver and the LED to monitor the instantaneous current value. The built-in ball lens on the LED provides a light beam with half-angle of 7.5 degrees, which is further collimated by passing through a combination of UV-coated lenses. As a result, a 255 nm light beam with diameter around 10 mm could be obtained, which is shown in Figure 3.18.

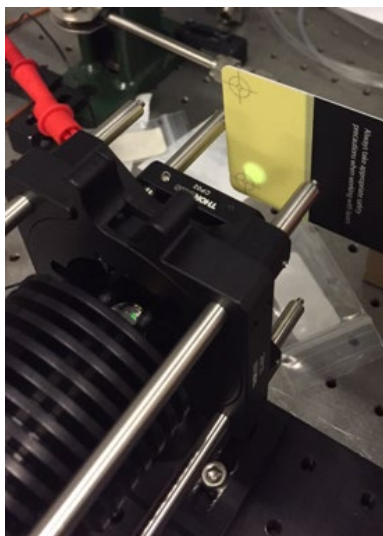


Figure 3.18. Collimated 255 nm UV light beam with diameter around 10 mm.

The detection of the UV light passing through the quartz flow reactor is accomplished by a 150~500 nm GaP Amplified Photodetector with switchable gains (model PDA25K, Thorlabs), which is directly connected to a high-definition oscilloscope (HDO6000, Teledyne Lecroy) for data acquisition. A bandpass filter of 240~395 nm is placed before the GaP detector to suppress the disturbance from scattered light. To maintain the orthogonality of the UV light beam to the flow reactor, both the LED and the amplified detector are mounted on a single cage system, which can be freely moved along

the flow reactor for O_3 measurement at different axial positions. Identical gas supplies and flow reactor system in Figure 3.14 are adopted in this work. The schematic of experimental set-up of non-intrusive O_3 measurement is shown in Figure 3.19, and the direct photograph of coupling between UV LED absorption system and the quartz flow reactor is shown in Figure 3.20.

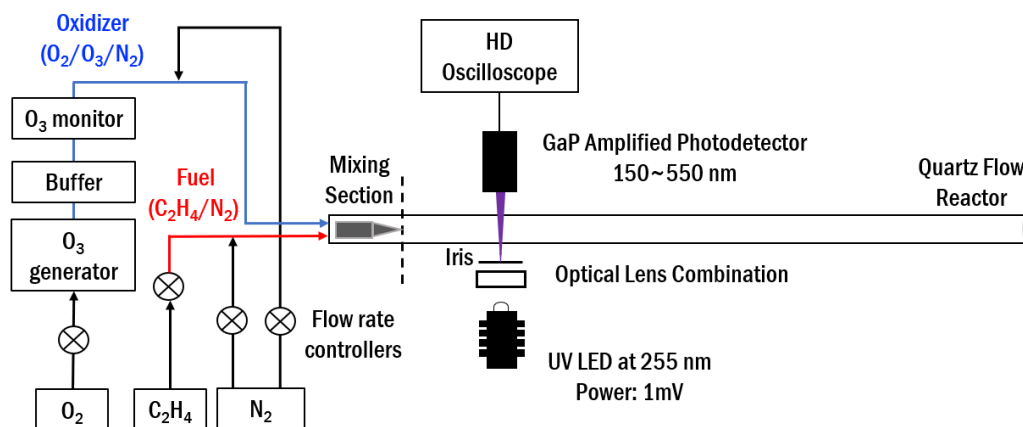


Figure 3.19. Schematic of experimental set-up of O_3 measurement using UV LED absorption.

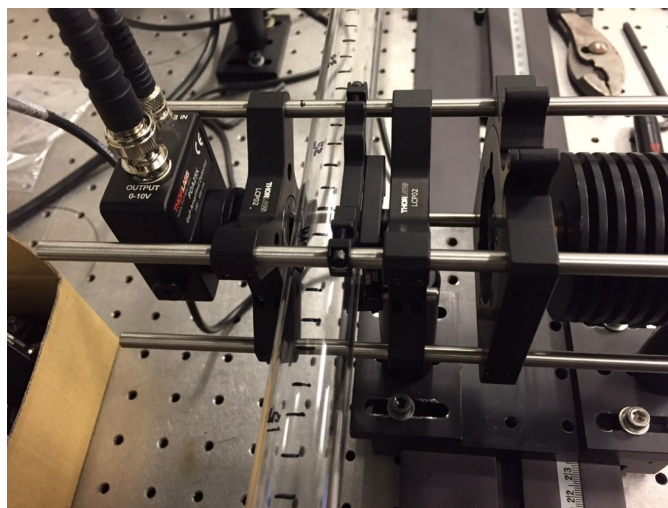


Figure 3.20. Direct photograph of coupling between UV LED absorption system and quartz flow reactor.

3.4.2 System Calibration

Based on the Beer-Lambert's Law for absorption, the relation between UV light intensity and O₃ concentration is given by

$$I/I_0 = \exp \left[-\sigma(\lambda) \times l \times N_A \times \frac{n_{O_3}}{C} \right]$$

where I_0 and I are the UV light intensity before and after absorption by O₃ respectively; $\sigma(\lambda)$ is the absorption cross-section at given wavelength and temperature; l is the optical length which is the inner diameter of the flow reactor as $l = 22$ mm; N_A is the Avogadro constant, $N_A = 6.02 \times 10^{23}$ /mole, and n_{O_3} is the molar density of O₃. In this work, the O₃ absorption cross-section measured by Gorshlev et al. [73] at $\lambda_0 = 253.73$ nm and $T_0 = 295 \pm 3$ K, i.e., $\sigma = 1.12 \times 10^{-17}$ cm²/molecule, is adopted to approximate the corresponding cross-section at $\lambda = 255$ nm and room temperature, which is measured around $T \approx 298$ K in the Combustion Lab.

To compensate the influence from possible non-ideal factors on the O₃ concentration calculation, a constant correction factor C is added to the original Beer's equation. Based on the present experimental set-up, it is believed that the non-ideality is mainly aroused by 1) The difference between the peak $\lambda = 255$ nm of the UV LED and the reference $\lambda_0 = 253.73$ nm at which σ was measured, 2) The incoherent light provided by the LED with FWHM of 12 nm, and 3) The inaccuracy in optical length caused by the tubular geometry of the flow reactor. Because of the low power output (1 mW) from the LED in this work, no attempt is made to establish a reference detector by splitting the collimated UV light beam, otherwise the signal-to-noise ratio would be lowered. During operations,

the measurement of I and I_0 is simply done by switching on and off the O_3 generator respectively at same reactor position.

To calibrate the absorption system and determine the correction factor C , under non-reacting condition, i.e., premixed $O_2/O_3/N_2$ no C_2H_4 , the measured O_3 concentrations from 255 nm UV absorption and ideal Beer's Law are plotted against the readings given by the O_3 monitor, with the latter ones considered as the authentic values. The result is shown in Figure 3.21.

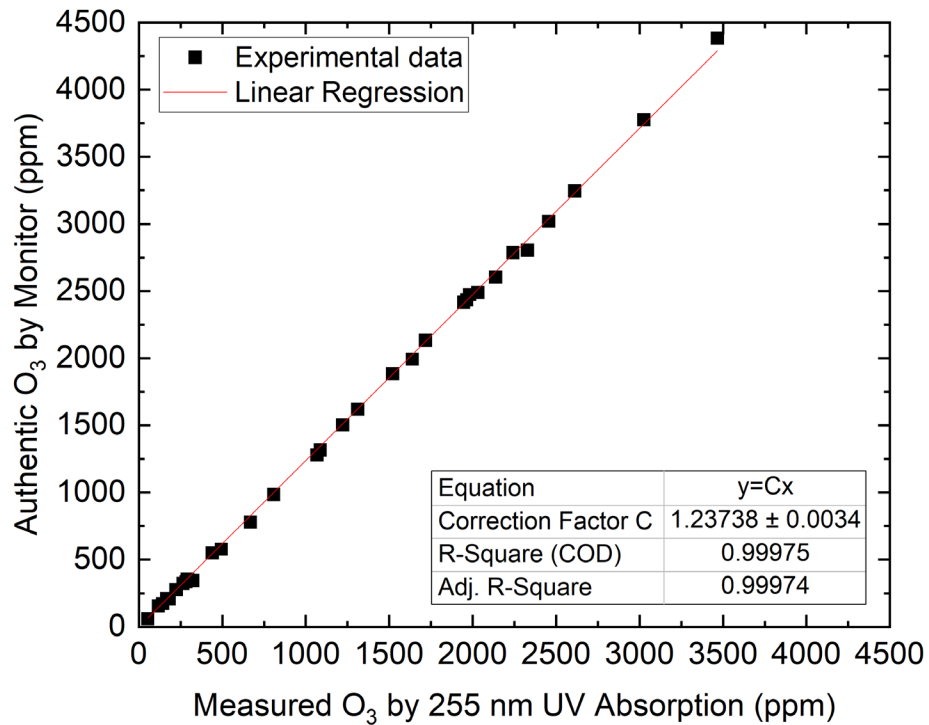


Figure 3.21. Linear regression between the measured O_3 concentrations (in ppmv) by 255 nm UV absorption (x axis) and the authentic values given by the O_3 monitor (y axis). The correction factor is given by the slope.

The calibration is accomplished with a wide range of O_3 concentrations from the lowest 60 ppmv to the highest 4000 ppmv. Given by the outcome of linear regression in Figure 3.21, the system correction factor of $C = 1.23738 \pm 0.0034$ is determined. Finally, at

$\lambda = 255$ nm and room temperature, using the present UV LED absorption and flow reactor set-up, the O₃ molar concentration can be calculated by,

$$n_{O_3}(\text{mole}/\text{cm}^3, \lambda = 255 \text{ nm and room temperature})$$

$$= \frac{1.23738 \times \ln(I/I_0)}{(-1.12 \times 10^{-17} \text{ cm}^2/\text{molecule}) \times 2.2 \text{ cm} \times (6.02 \times 10^{23} \text{ molecule}/\text{mole})}$$

It should be noted that since the readings from O₃ monitor (Teledyne Instruments, Model 454, accuracy $\pm 1\%$ of full scale) is considered as the reference in the calibration procedure, its performance strongly affects the absolute accuracy and detection limit of the UV absorption system. By using other calibration references with much higher accuracy, a different correction factor C should be expected.

3.5 Synchrotron Radiative Photoionization Molecular Beam Mass Spectrometry (SRPI-MBMS)

Being one of the most advanced and adaptable diagnostic techniques, the vacuum ultraviolet (VUV) photoionization molecular beam mass spectrometry has been known as a very powerful tool in chemical kinetic study. The use of synchrotron radiation as the light source renders high photon intensity meanwhile delicate tunability in wide range, which makes unambiguous species characterization and isomer differentiation possible.

To have a deeper understanding in the complex chemistry of the O_3 initiated C_2H_4 oxidation at room temperature, kinetic study is undertaken by coupling the fast-mixing flow reactor system to the SRPI-MBMS at the Combustion and Flame endstation on the beamline BL03U of Hefei Light Source-II (HLS-II, energy of 800 MeV and constant beam current 400 mA) at National Synchrotron Radiation Laboratory (NSRL), China. The photographs of the HLS-II overview and BL03U beamline are shown in Figure 3.22 and Figure 3.23 respectively. Details regarding the design of the beamline and endstation can be found in Ref. [77].



Figure 3.22. Overview of HLS-II at NSRL, Hefei, China, with energy of 800 MeV and constant beam current 400 mA.



Figure 3.23. Undulator beamline BL03U at HLS-II.

This undulator based beamline provides VUV light with photon energy from 5 eV to 21 eV and photon flux of 10^{13} photons/s at 10 eV. The monochromator of the beamline gives an averaged resolution of $E/\Delta E \approx 4000$ in full energy range. In order to attenuate the high-order harmonics, a low-pressure Ar gas filter is placed upstream to the endstation. The sampling is done by a quartz nozzle (orifice diameter $\approx 70 \mu\text{m}$) fixed at the outlet center of the flow reactor. Immediately downstream to the nozzle, by the sudden two-stage expansions (1st stage pressure $\sim 10^{-4}$ torr and 2nd stage pressure $\sim 10^{-7}$ torr), a supersonic molecular beam excluding further collision between molecules is generated. The molecular beam would then intersect with the synchrotron radiative VUV photon beam in ionization chamber, where selective photoionization happens. The resulting cations are then guided into a time-of-flight mass spectrometry (mass resolution $m/\Delta m \approx 2000$) and distinguished by their mass-to-charge ratios (m/z). By continuously tuning the VUV photon energy, photoionization efficiency (PIE) curve for each single m/z can be acquired. With known molecular weight and ionization threshold on the PIE curve, the species could possibly be characterized. The isomers may be separated by their different ionization thresholds on the same PIE curve. The coupling between SRPI-MBMS and fast-mixing flow reactor system is schematically shown in Figure 3.24 and the direct photograph is shown in Figure 3.25.

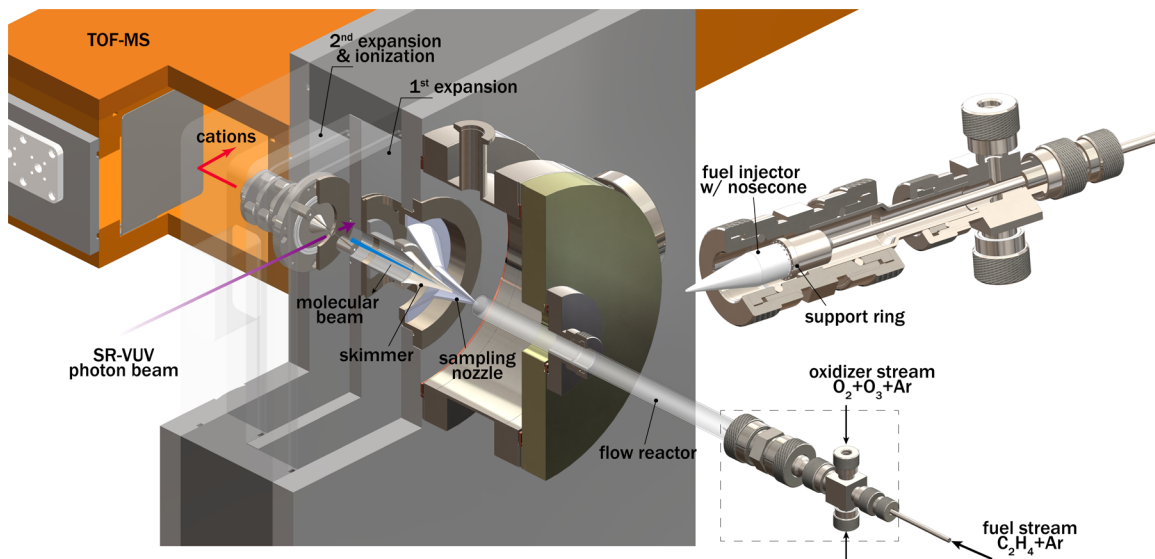


Figure 3.24. Schematic of coupling between SRPI-MBMS and the fast-mixing flow reactor system.

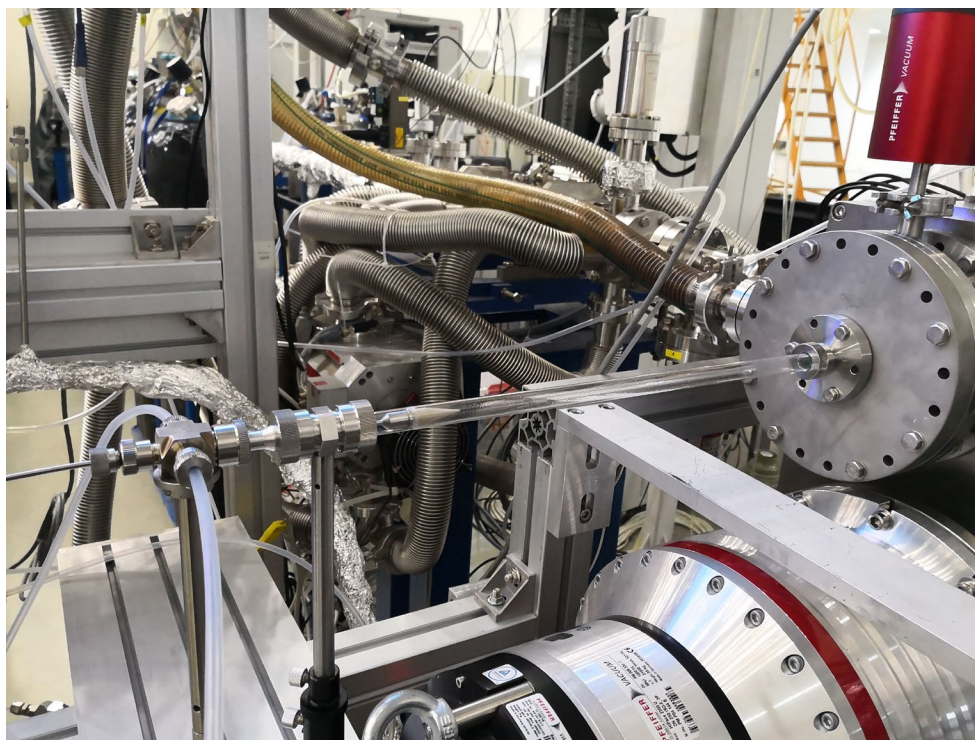


Figure 3.25. Direct photograph of fast-mixing flow reactor system being coupled to SRPI-MBMS at Combustion and Flame endstation, HLS-II, NSRL.

The latest designed flow reactor system in Figure 3.9 is deployed in this SRPI-MBMS study, with similar gas supply arrangement illustrated in Chapter 3.2 and Chapter 3.3. The O₃ is produced by a commercial ozone generator (model CF-G-3-10g, Qingdao Guolin) from pure O₂, and its real-time mass fraction is demonstrated by the ozone monitor (Teledyne Instruments, Model 454, accuracy $\pm 1\%$ of full scale) downstream. During experiments, the maximum fluctuation in O₃ concentration is recorded as -2.4% to 8.4% of the set point. All supplied gases are in the UHP grade, whose flow rates are precisely regulated by the mass flow controllers (MKS Instruments, accuracy $< 1\%$ of set point).

3.6 Laminar Jet Flame Burner

Extensive studies have been reported on lifted laminar jet flames in the past [78-84]. Figure 3.26 clearly shows the detail structure of a steady laminar lifted flame. The lean and rich premixed wings, together with the diffusion flame in between, converging at one point, namely, the triple point.

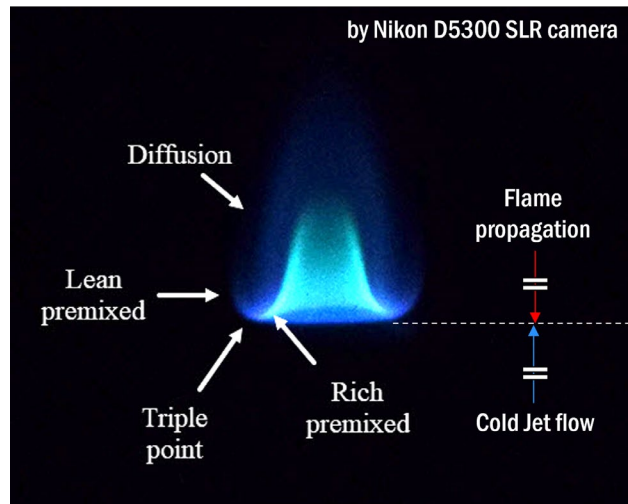


Figure 3.26. Structure of steady laminar lifted flame, direct photograph taken by SLR camera.

Based on the diffusion flame theory, if the lifted flame is steady, then the triple point would necessarily sit on the stoichiometric contour ($\phi = 1$), where the fuel mass fraction follows $Y_F = Y_{F, st}$. Accordingly, the stabilization of lifted flame is achieved by the dynamic balance between the propagation speed of the triple flame (S_{tri}), which is located at the base of the lifted flame, and the axial flow velocity (u_{st}) just upstream of the flame along the stoichiometric contour. Therefore, the liftoff height (HL) of the flame could be a sensitive indicator to the change in either S_{tri} or upstream flow condition. As the triple flame propagation speed S_{tri} is closely correlated to S_L , the steady laminar lifted flame has been utilized as a platform to study the change in S_L caused by chemical kinetic effect.

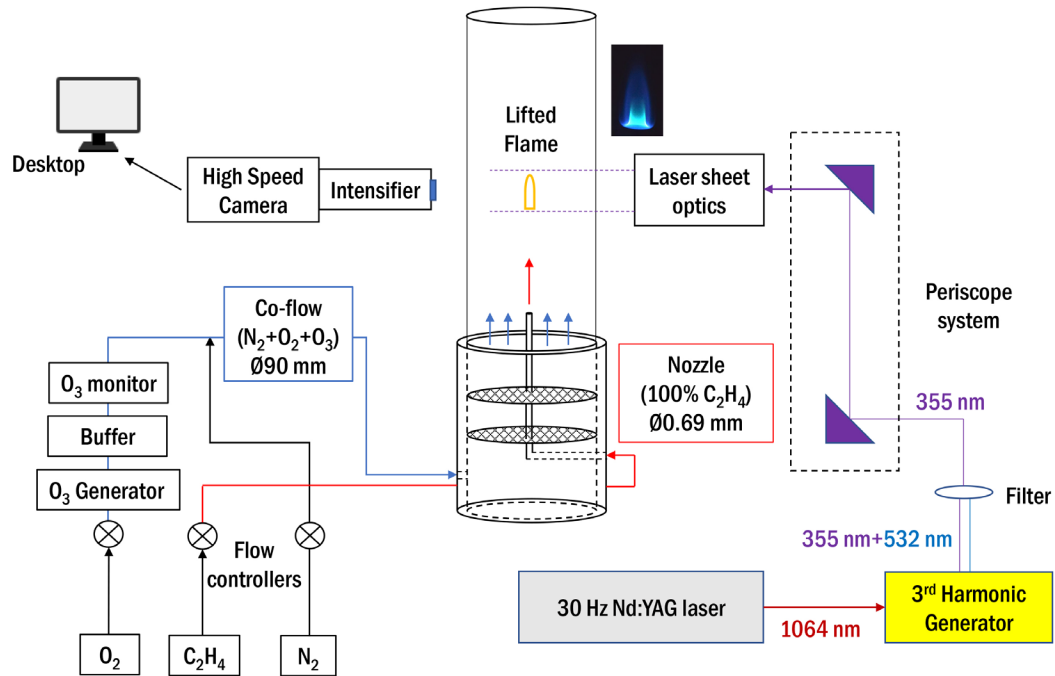


Figure 3.27. Schematic of laminar jet flame burner experimental set-up.

Figure 3.27 schematically illustrates the experimental system, which consists of a laminar jet flame burner and a CH_2O planar laser induced fluorescence (PLIF) set-up. The burner used here is the same one applied in the study by Ombrello et al. [8, 85] comprising

a slender, aerodynamically shaped quartz fuel nozzle with 0.69 mm inner diameter at the exit on the tip, and a cylindrical quartz shield with inner diameter of 90 mm and length of 460 mm to contain the O₂/O₃/N₂ co-flow. During operations, the O₃ is continuously produced by the O₃ generator (Ozone Solutions, TG40) using pure O₂ as input and its mass fraction is measured by an absorption-based monitor (Teledyne Instruments, Model 454, accuracy ±1% of full scale) downstream. Both O₂ and N₂ are of UHP (99.999%, Airgas) grade, and C₂H₄ is of chemically pure (99.5%, Airgas) grade.

The spatial distribution of CH₂O is qualitatively characterized by PLIF employing the 3rd harmonic Nd:YAG laser at 355 nm, and a 0.5 mm thick, 28 mm width laser sheet is formed by the combination of a concave lens and two convex lenses. The CH₂O fluorescence corresponding to the $\tilde{A}^1A_2 \sim \tilde{X}^1A_1$ transition is collected by a high-speed camera (NAC GX-3) coupled to an intensifier (Video Scope International Ultracam3) with a 425 nm centered band-pass filter. To track the flames at different steady H_L, a periscope mechanism is used to adjust the laser sheet vertically. During the experiments, 400 images are accumulated in each measurement and the background scattering is subtracted to increase the signal-to-noise ratio.

CHAPTER 4. MEASUREMENT OF GLOBAL REACTION RATE CONSTANT BETWEEN ETHYLENE AND OZONE AT AMBIENT CONDITIONS

In this chapter, the long-studied global reaction rate constant of $C_2H_4+O_3$ is revisited using non-intrusive diagnostic technique at room temperature and atmospheric pressure. By the application of 255 nm UV LED absorption, in-situ O_3 concentration is quantified along the quartz flow reactor. The experimental set-up of coupling between the optical and the fast-mixing flow reactor system has been demonstrated in Chapter 3.4, where the molar density of O_3 is given by the modified Beer's Law with added system correction factor.

4.1 Pseudo 1st Order Kinetics

To determine the rate constant of bimolecular reaction $C_2H_4+O_3$, with the amount of C_2H_4 in excess of O_3 , i.e., $[C_2H_4]_0 \gg [O_3]_0$, the original 2nd order reaction can be approximated as pseudo 1st order instead, and the following equation is then satisfied,

$$k \times t = \frac{1}{[C_2H_4]_0} \ln \frac{[O_3]_0}{[O_3]}$$

where $[C_2H_4]_0$ and $[O_3]_0$ are the initial molar densities of C_2H_4 and O_3 , respectively, in the unit of mole/cm³; k is the reaction rate constant in the unit of cm³/mole s, and t is the absolute reaction time. In the flow reactor scheme, k can be obtained by measuring the O_3 concentrations at two separated locations, e.g., L_A and L_B , along the flow reactor with known axial distance and bulk flow velocity U , in order that the reaction time t and $[O_3]_0$

are eliminated. The equation above regarding k could then be rewritten in the form as follows,

$$k \times \frac{(L_B - L_A)}{U} = \frac{1}{[C_2H_4]_0} \ln \frac{[O_3]_A}{[O_3]_B}$$

4.2 Experimental Boundary Conditions

The initial reactant mole fractions and volumetric flow rates are tabulated in Table 3, where the C_2H_4 is measured by the GC before O_3 addition, and the O_3 is given by the monitor upstream of the flow reactor. With initially $(C_2H_4)_0/(O_3)_0 \approx 190$, the requirement of $[C_2H_4]_0 \gg [O_3]_0$ should be safely satisfied and the pseudo 1st order approximation is reasonable. In this work, the experiments are carried out at ambient conditions, which are gauged as $T \approx 298$ K and $P \approx 740$ torr (or 0.987 bar) in the isolated room 121 of the Combustion Lab. Due to dominant abundance (~90%) of diluent N_2 in the reaction system, no temperature regulation is applied during the experiments. Nevertheless, in-situ temperature in the flow reactor is monitored using a thermocouple for higher accuracy in the rate constant calculation.

Table 3. Initial reactant mole fractions and volumetric flow rates in the 255 nm absorption experiments at room temperature and pressure. Both C_2H_4 and O_2 are measured by the GC, and O_3 is given by the O_3 monitor.

Species	Measured Mole Fractions	Flow Rates
$(C_2H_4)_0/(O_3)_0$	~190	-
C_2H_4	2.2411%	264 sccm
O_3	0.0118%	-
O_2	7.8761%	1156 sccm
N_2	balance	10573 sccm

4.3 Global Reaction Rate Constant Measurement

To examine the stability of O_3 at current experimental conditions, the 255 nm UV LED absorption experiment is first conducted with O_3 only, in which no C_2H_4 is added. The O_3 concentration in $O_3/O_2/N_2$ mixture is measured at multiple axial positions along the flow reactor, and the result is shown in Figure 4.1. The axial distance in the flow reactor is counted with zero point on the fuel injector nosecone tip. The measured concentrations directly demonstrate that negligible O_3 decomposition can be observed within interested flow residence time. At $T = 298$ K and zero humidity, a long half-life time of O_3 near 1500 minutes was reported [86] in quiescent air, however, the air flow could greatly accelerate the O_3 decomposition and extraordinarily lower the half-life time.

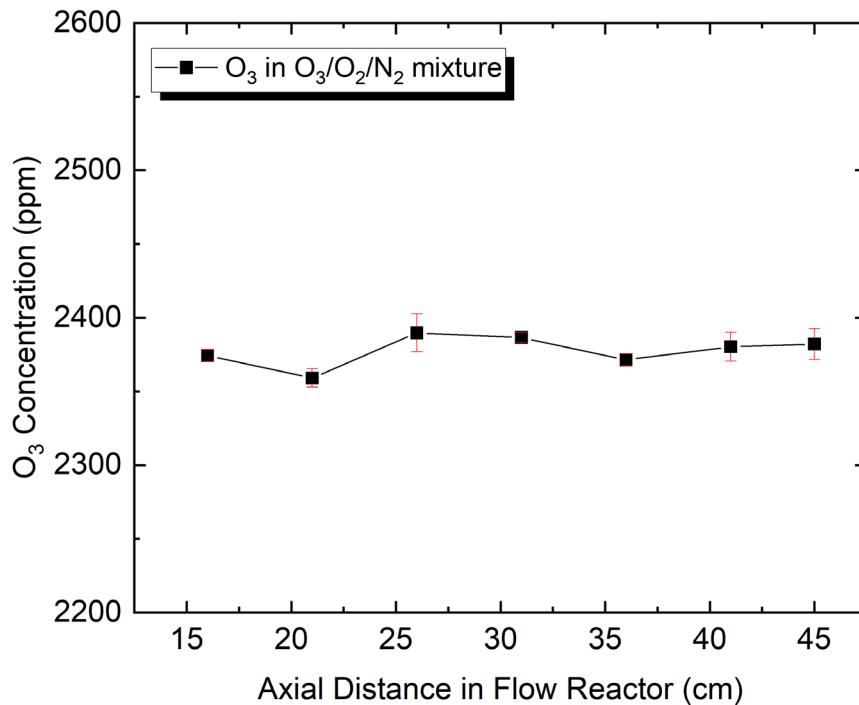


Figure 4.1. The measured O_3 concentrations using 255 nm UV LED absorption along flow reactor without C_2H_4 addition at room temperature and pressure.

The C_2H_4 is then added into the flow reactor system and the resulted O_3 decay is recorded at reactant ratio of $(C_2H_4)_0/(O_3)_0 \approx 190$. The UV absorption measurement is carried out at 5 equally distributed axial locations, each separated by 5 cm. Repeated experiments are undertaken three times to ensure the data accuracy and repeatability. The measured O_3 concentrations at different axial positions are plotted in Figure 4.2, in which linear O_3 decay along the flow reactor is clearly demonstrated.

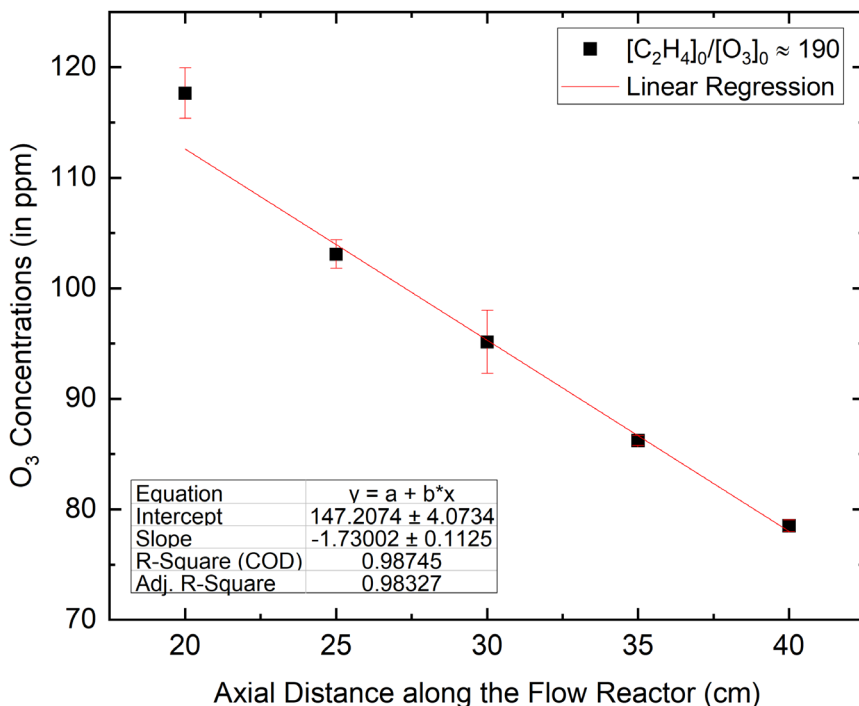


Figure 4.2. Measured O_3 decays in flow reactor with $(C_2H_4)_0/(O_3)_0 \approx 190$ at room temperature and atmospheric pressure. Linear regression of raw data given in the red line.

During each kinetic experiment, almost constant temperature is recorded in the flow reactor by the thermocouple, before and after C_2H_4 addition. With the bulk velocity U estimated from total gas flow rate around 11993 sccm (the sum of $C_2H_4+O_2+N_2$), the global rate constant of $C_2H_4+O_3$ at ambient conditions is calculated as,

$$k_{\text{C}_2\text{H}_4+\text{O}_3}(\text{room } T) = (8.1460 \pm 0.1797) \times 10^5 \text{ cm}^3/\text{mole s}$$

The comparison between this newly measured rate constant, and the selected values from literatures [48, 87-94] found in NIST Chemical Kinetics Database, is illustrated in Figure 4.3, where the results obtained by single temperature measurement are demonstrated in scattered symbols, while the other results from continuous measurement in range of temperatures are plotted in lines.

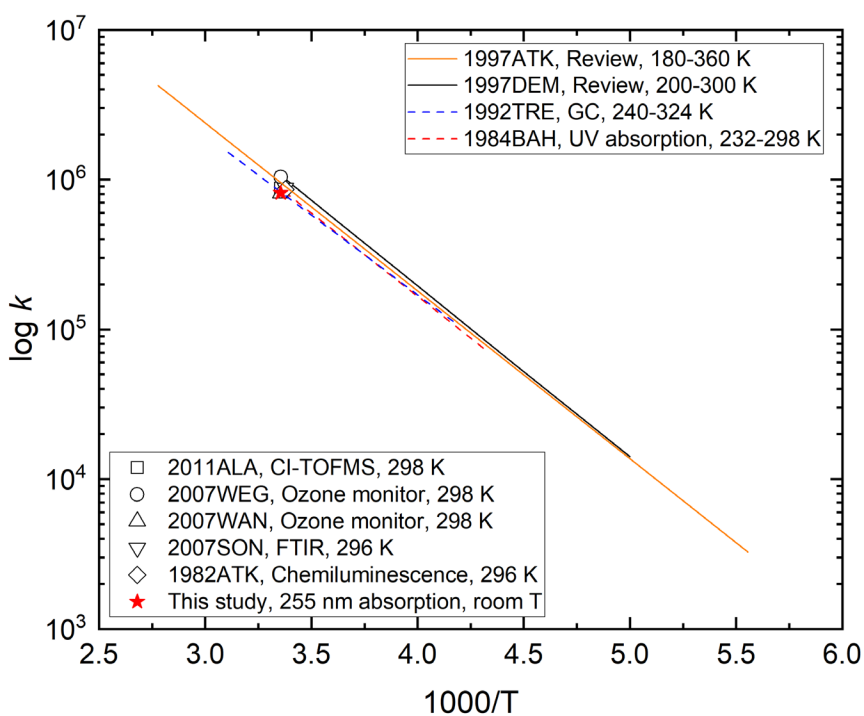


Figure 4.3. Comparison between the newly measured rate constant k of $\text{C}_2\text{H}_4+\text{O}_3$ in this study at ambient conditions, and the selected results from past literatures in NIST Chemical Kinetics Database. Applied diagnostic methods and temperature conditions are given in boxes.

Multiple diagnostic techniques were applied previously, including both intrusive, i.e., GC, chemical ionization time-of-flight mass spectrometry (CI-TOFMS) and UV-absorption-based ozone monitor, and non-intrusive methods, i.e., Fourier transform

infrared spectroscopy (FTIR), chemiluminescence and UV absorption. Figure 4.3 plainly reveals the excellent agreement between the result in this work and the ones from former literatures.

In regard to the uncertainty in this newly measured k , based on the equation from the pseudo 1st order kinetic approximation, the bulk velocity U in flow reactor should be the direct and most dominant source of error in rate constant determination. In this work, U is simply estimated from the total flow rates of the reactants, assuming a uniform velocity profile on the reactor cross-section. It is believed that this uncertainty from U could be greatly reduced if the flow field in the reactor is known, or the flow time between the two optical sampling positions is accurately measured. Moreover, the uncertainty in molar density measurement of $[C_2H_4]_0$ from the GC (INFICON, sensitivity down to 1 ppm) would be transferred to the calculated rate constant. However, this part is expected to be of minor importance only, compared to the uncertainty from U .

CHAPTER 5. INVESTIGATION OF PRODUCT COMPOSITION IN OZONE INITIATED ETHYLENE OXIDATION USING GC AT ROOM TEMPERATURE

In this chapter, the composition of major products in O_3 initiated C_2H_4 oxidation at ambient conditions is investigated in the fast-mixing flow reactor system using gas chromatography. The set-up has been described in Chapter 3.3. Even though the number of products identified by the GC is limited, many insights have been gained from the results especially the kinetic importance of secondary reactions induced by the rapid ozonolysis of C_2H_4 . The outcome in this chapter reveals that there are many unknowns in this room-temperature oxidation process and impels the further and more detailed investigations using SRPI-MBMS which will be shown later.

5.1 Experimental Boundary Conditions

To study the behavior of products under different C_2H_4/O_3 ratios, three different sets of concentrations are designated for the reactants $C_2H_4/O_2/O_3/N_2$. Namely, excessive C_2H_4 , excessive O_3 and $C_2H_4:O_3 \approx 1:1$. The reactant mole fractions are tabulated in Table 4. For the two cases with excess reactant, the value of C_2H_4/O_3 or O_3/C_2H_4 is designed to be 10, which is commonly adopted in chemical kinetic studies.

Table 4. Designed reactant mole fractions for the three cases in the GC experiments at room temperature and atmospheric pressure.

Case Name	C_2H_4	O_2	O_3	N_2	C_2H_4/O_3
Excessive C_2H_4	2%	9%	0.2%	Balance	10
Excessive O_3	0.1%	14%	1%	Balance	0.1
$C_2H_4:O_3 \approx 1$	0.2%	9%	0.2%	Balance	1

The experiments in this chapter are carried out at room temperature and atmospheric pressure, which are locally $T \approx 298$ K and $P \approx 740$ torr in the isolated room 121 of the Combustion Lab. No specific temperature control strategy is applied due to dominant inert N_2 among the reactants. During the experiments, a maximum 10 K increase is measured along the flow reactor by thermocouple, which can be considered negligible.

5.2 Chromatographs and Product Identification

The first goal of this work is to identify the major products in O_3 initiated C_2H_4 oxidation at ambient condition. The GC probe is fixed 500 mm downstream of the fuel injector, and the sampling time for each run is set to be 20 s. The flow residence time before sampling is around 1 s for all three cases. The chromatography results before O_3 addition are shown in Figure 5.1.

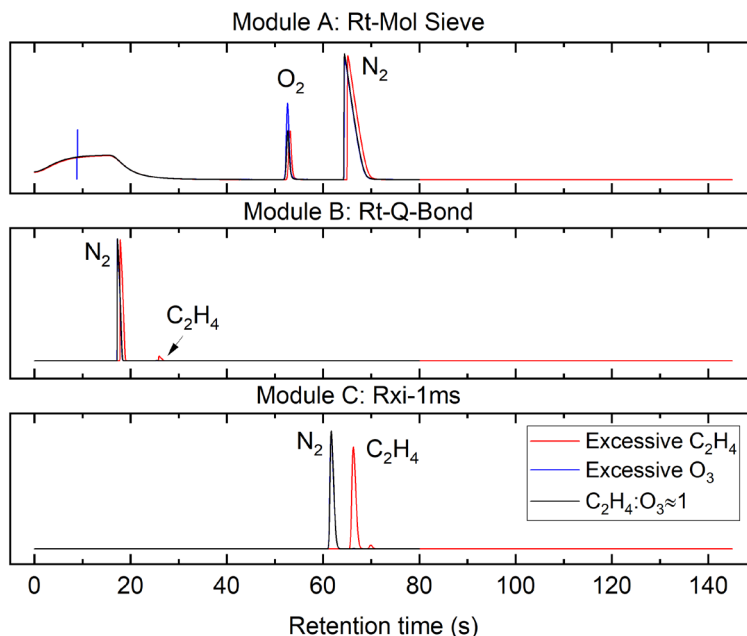


Figure 5.1. Chromatographs without O_3 addition of excessive C_2H_4 (red), excessive O_3 (blue) and $C_2H_4:O_3 \approx 1$ (black) cases.

For the case of excessive C_2H_4 , excessive O_3 and $C_2H_4:O_3 \approx 1$, before O_3 is added, the mole fractions of C_2H_4 are measured as 2.084%, 0.079% and 1.812% by the GC respectively, which all reasonably match the target boundary conditions tabulated in Table 4. The O_3 generator is then switched on, and the results of reacting cases given by module A, B and C are presented individually in Figure 5.2, Figure 5.3 and Figure 5.4 as following.

In this INFICON GC, the module A with Rt-molecular sieve column is specifically designed for detection of permanent gases, i.e., the common components in air. In Figure 5.2, it is shown that both H_2 and CO are characterized as products in this oxidation process at room temperature, which is aligned with the prediction by C_2H_4 ozonolysis mechanism.

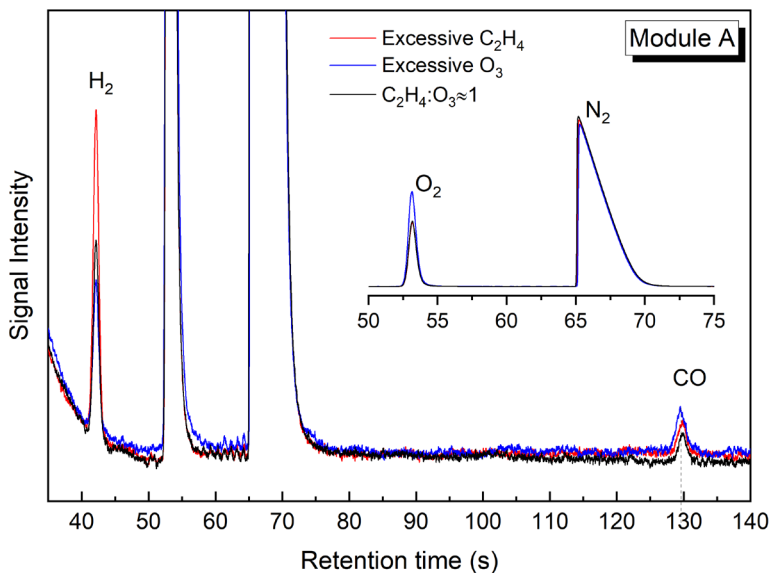


Figure 5.2. Chromatograph by module A with O_3 addition of excessive C_2H_4 (red), excessive O_3 (blue) and $C_2H_4:O_3 \approx 1$ (black) cases, with retention time 35 s to 140 s.

The module B with Rt-Q-bond column is intended for detection of hydrocarbons smaller than C_3 . As shown in Figure 5.3(a), with retention time from 15 s to 55 s, the productions of CO_2 and H_2O are detected. For the case of excessive C_2H_4 , small amount of ethane (C_2H_6) can be seen at retention time near 31 s, which is believed due to the impurity

of C_2H_4 , as identical 8 ppmv of C_2H_6 is measured before and after O_3 addition. Within the same module in Figure 5.3(b), CH_3OH comes off at around 105 s. The combined signal of ethylene oxide, cyc- C_2H_4O , and acetaldehyde, CH_3CHO , is observed with retention time close to 117 s. However, the two isomers could not be separated by the Rt-Q-bond column under applied GC method.

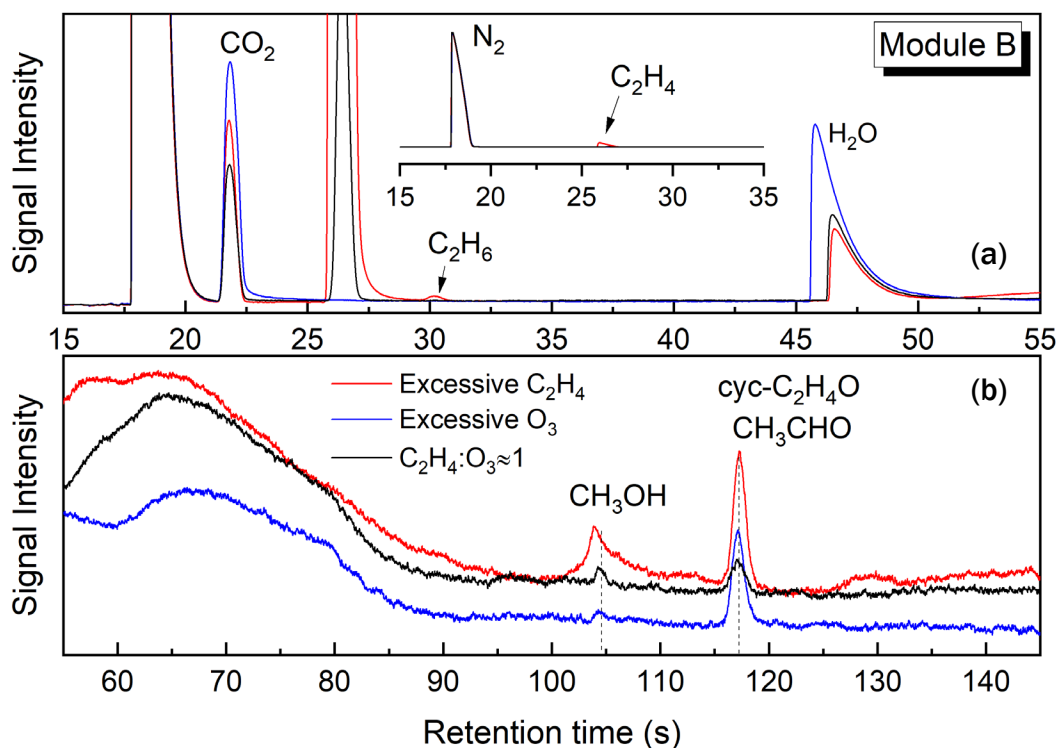


Figure 5.3. Chromatograph by module B with O_3 addition of excessive C_2H_4 (red), excessive O_3 (blue) and $C_2H_4:O_3 \approx 1$ (black) cases, with retention time (a) 15 s to 55 s and (b) 55 s to 145 s.

The module C with Rxi-1ms column is designed for detection of hydrocarbons larger than C_3 , as well as the oxygenated compounds. As shown in Figure 5.4(a), being the most abundant ozonolysis products, CH_2O elutes with retention time around 74 s. Other major ozonolysis products, CO_2 and H_2O , including the reactant C_2H_4 are also detected in module C. In Figure 5.4(b), it clearly demonstrates that successful separation between cyc- C_2H_4O

and CH_3CHO is achieved using the Rxi-1ms column. Besides, formic acid, HCOOH , is characterized with retention time near 100 s.

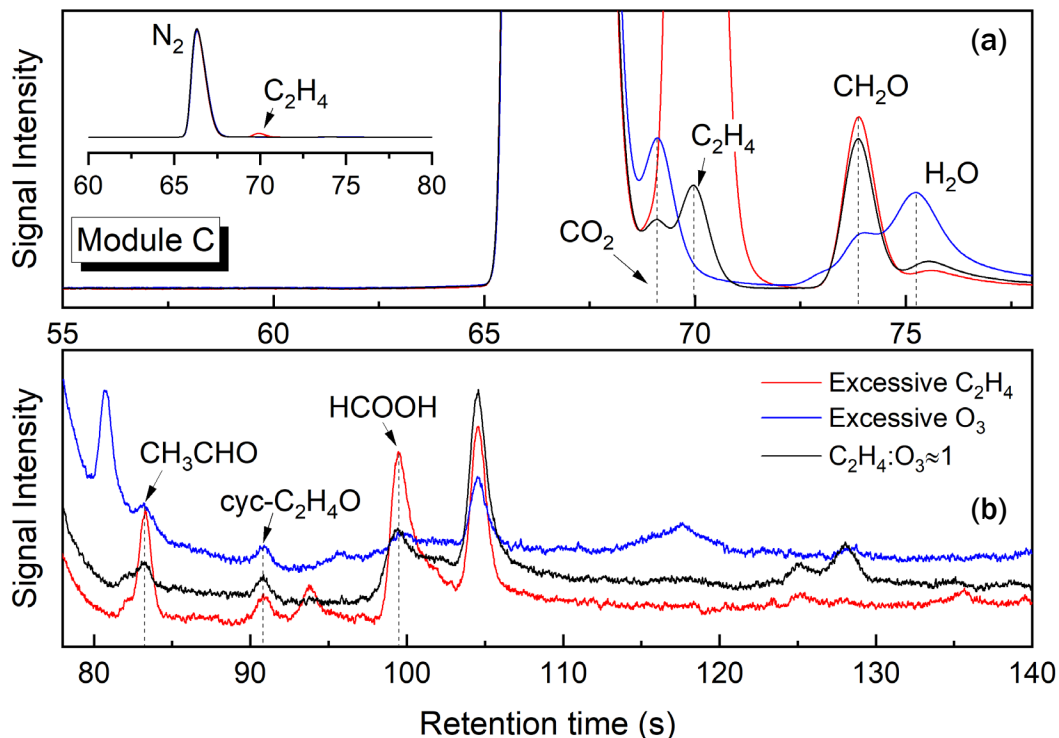


Figure 5.4. Chromatograph by module C with O_3 addition of excessive C_2H_4 (red), excessive O_3 (blue) and $\text{C}_2\text{H}_4:\text{O}_3 \approx 1$ (black) case, with retention time (a) 55 s to 78 s and (b) 78 s to 140 s.

Generally, by the simple diagnostic method of GC, in total nine species are characterized as products in the O_3 initiated C_2H_4 oxidation at room temperature. Six of them are predicted by the mechanism of $\text{C}_2\text{H}_4+\text{O}_3$ described in Chapter 2.2, including CO , H_2 , CO_2 , H_2O , CH_2O and $\text{cyc-C}_2\text{H}_4\text{O}$. It is most likely that the probed CH_3OH , CH_3CHO and HCOOH are generated via secondary reactions following the ozonolysis of C_2H_4 . As proposed by Neeb et al. [59], the production of HCOOH is kinetically feasible via the bimolecular reaction between sCI and CH_2O , i.e., $\text{CH}_2\text{OO}+\text{CH}_2\text{O} \rightarrow \text{HCOOH}+\text{CH}_2\text{O}$. The

authors experimentally demonstrated that with extra CH_2O added to the reaction system of C_2H_4 and O_3 , a higher production yield of HCOOH was measured.

From a qualitative point of view regarding the products, similar composition is observed for all three cases with various initial $\text{C}_2\text{H}_4/\text{O}_3$ ratios. However, noticeable inconsistency in relative yields between products strongly indicates the difference in dominant secondary kinetic pathways. For example, looking at the mechanism of C_2H_4 ozonolysis reaction in Figure 2.3, the only production pathway for CO and H_2 is via R11a and R11b, respectively. Therefore, similar ratio of CO/H_2 should be expected for all three cases. However, in Figure 5.2, a much higher CO/H_2 in signal intensity is observed in the case of excessive C_2H_4 than excessive O_3 , which implies the existence of different producing/consuming channels in addition to the basic ozonolysis pathways.

Although nine species have been successfully identified so far, many peaks remain unrecognized yet in Figure 5.4(b). Great efforts have been paid in the past trying to figure out the species they stand for, however, with this compact INFICON GC this task is nearly impossible. With the retention time as the only information, which is a strong function of temperature and pressure in the GC column, the only way for species identification is by comparing experimental results with calibration standards. If the mass number of the peak on chromatograph is known, then the identification process might be much easier.

5.3 Quantitative Analysis

The relative concentrations of identified species are measured and tabulated in Table 5. The results indicate that for the excessive O_3 case, C_2H_4 has been consumed completely upon sampling by the GC, showing direct ozonolysis products, H_2 , CO , CO_2 ,

H₂O and CH₂O are being produced. The calculated yields of all nine identified products in relative to the converted C₂H₄ are listed in Table 6. Regarding the uncertainty of the relative concentrations given by the GC, the largest component should come from the calibration. Higher uncertainties should be expected for those species calibrated from liquid standard evaporation, which are HCOOH and CH₃CHO in this work.

Table 5. Measured species relative concentrations (in ppmv) by GC in O₃ initiated C₂H₄ oxidation at room temperature and atmospheric pressure, under flow residence time ~ 1 s.

Species	Excessive C ₂ H ₄	Excessive O ₃	C ₂ H ₄ :O ₃ ≈ 1
C ₂ H ₄	19193	0	685
O ₂	96355	144792	97532
CH ₂ O	1883	512	1283
CO	388	546	350
CO ₂	322	425	221
H ₂ O	563	1711	817
H ₂	240	104	132
cyc-C ₂ H ₄ O	8	8	8
HCOOH	165	16	78
CH ₃ CHO	89	70	20
CH ₃ OH	15	1	1

a. the ozonolysis products; b. products by secondary reactions

Table 6. Product yields in O₃ initiated C₂H₄ oxidation at room temperature and atmospheric pressure, under flow residence time ~ 1 s.

	Excessive C ₂ H ₄	Excessive O ₃	C ₂ H ₄ :O ₃ ≈ 1
[C ₂ H ₄] ₀ (ppmv)	20842	787	1812
ΔC ₂ H ₄ (ppmv)	1649	787	1127
Y(CH ₂ O)	1.142	0.651	1.138
Y(CO)	0.235	0.694	0.310
Y(CO ₂)	0.195	0.540	0.196
Y(H ₂ O)	0.341	2.175	0.725
Y(H ₂)	0.145	0.132	0.117
Y(cyc-C ₂ H ₄ O)	0.005	0.010	0.007
Y(HCOOH)	0.100	0.020	0.069
Y(CH ₃ CHO)	0.054	0.089	0.018
Y(CH ₃ OH)	0.009	0.001	0.001

It appears that comparable yields can be found between the case of excessive C₂H₄ and C₂H₄:O₃ ≈ 1, regarding all direct ozonolysis products except H₂O, which suggests similar kinetic mechanism and pathways controlling those two cases. Reasonable agreement is achieved between the measured product yields of H₂, CO, CO₂ and HCOOH in those two cases and past literatures [59, 60, 62, 95, 96] from atmospheric chemistry. As shown in Table 6, it is interesting to see apparent difference in product yields in the case of excessive O₃ compared with the other two. Specifically, much higher yields of CO, CO₂ and H₂O are measured with excess O₃, while a much lower yield of CH₂O is obtained instead. For the case of excessive C₂H₄ and C₂H₄:O₃ ≈ 1, the corresponding CH₂O yields of 1.142 and 1.138 are measured respectively, which are both close to unity in accordance with the prediction by the ozonolysis mechanism. However, for the case of excessive O₃, the yield of CH₂O is measured to be 0.651 only. Similar observation was reported by Neeb et al. [59], where the yield of CH₂O decreased, meanwhile the yield of CO increased with excess O₃ in reactants. This result could be rationalized by the further oxidation of CH₂O by $\dot{O}H$ through the following reaction sequence,



With the theoretical production yield of $\dot{O}H$ up to 20% from C₂H₄+O₃ at T = 300 K and P = 760 torr (refer to Chapter 2.2), in the chemical system with abundant O₂ and O₃, the reaction sequence of R21 to R23 could be ideally self-catalytic. Consequently, more

CO and H₂O would be directly generated from CH₂O oxidation, while extra CO₂ could be provided through $\text{CO} + \dot{\text{O}}\text{H} \rightarrow \text{CO}_2 + \dot{\text{H}}$. Being contrary to those products as discussed above, nearly consistent yield of H₂ is measure for all three cases, independent to the ratio of C₂H₄/O₃. Such outcome suggests that the ozonolysis reaction is the exclusive formation mechanism for H₂ in O₃ initiated C₂H₄ oxidation at room temperature, while the effect from possible secondary reactions on H₂ is minor.

In addition to the six ozonolysis products, non-negligible yields of HCOOH and CH₃CHO are measured as well. As listed in Table 6, among all three cases, the highest yield of HCOOH appears with excess C₂H₄, while the lowest value is measure with excess O₃. This could be qualitatively explained by the proposed association between CH₂O and HCOOH in the current chemical system, where higher CH₂O concentration would lead to higher HCOOH formation, and vice versa. Both CH₃OH and CH₃CHO have been widely acknowledged as key intermediates in low-temperature fuel oxidation chemistry. The possible formation pathways of these two species will be proposed later in Chapter 6.

CHAPTER 6. COMPREHENSIVE PRODUCT CHARACTERIZATION IN OZONE INITIATED ETHYLENE OXIDATION USING SRPI-MBMS AT ROOM TEMPERATURE

To have further understanding in the complex chemistry behind the O₃ initiated C₂H₄ oxidation, a kinetic investigation is conducted in the newly designed flow reactor at room temperature, using tunable SRPI-MBMS and quantum chemical calculations. With the help of advanced diagnostic method, much more species are detected and identified in this room-temperature oxidation system, including both relative stable products and reactive intermediates. Based on such new discovery by experiment, some relevant secondary reactions following the ozonolysis of C₂H₄ are proposed. The set-up has been previously shown in Chapter 3.5.

6.1 Experimental Boundary Conditions

As have been demonstrated by the results using GC in Chapter 5, no apparent difference is observed among the three cases with different C₂H₄/O₃ ratios, in terms of product composition. Therefore, the boundary condition with excess C₂H₄ is adopted here, specifically, 1.8% C₂H₄, 0.2% O₃, 9.4% O₂, and 88.6% Ar. The residence time in the flow reactor before sampling is estimated close to 1.2 s. The experiments in this chapter are carried out at ambient conditions, which the room temperature at NSRL is regulated around $T \approx 297$ K and the pressure is approximately $P \approx 760$ torr. No temperature control is applied on the flow reactor due to dominant diluent Ar in the mixture. The PIE curves are recorded from photon energy 8.3 eV to 11.8 eV at 0.02 eV/step and sampling time of 200 s/step.

6.2 Species Characterization

An example of a mass spectrum is demonstrated in Figure 6.1, where the photon energy of VUV light is fixed at 14.49 eV, so that most products in the gaseous sample could be ionized and therefore detected by the mass spectrometry.

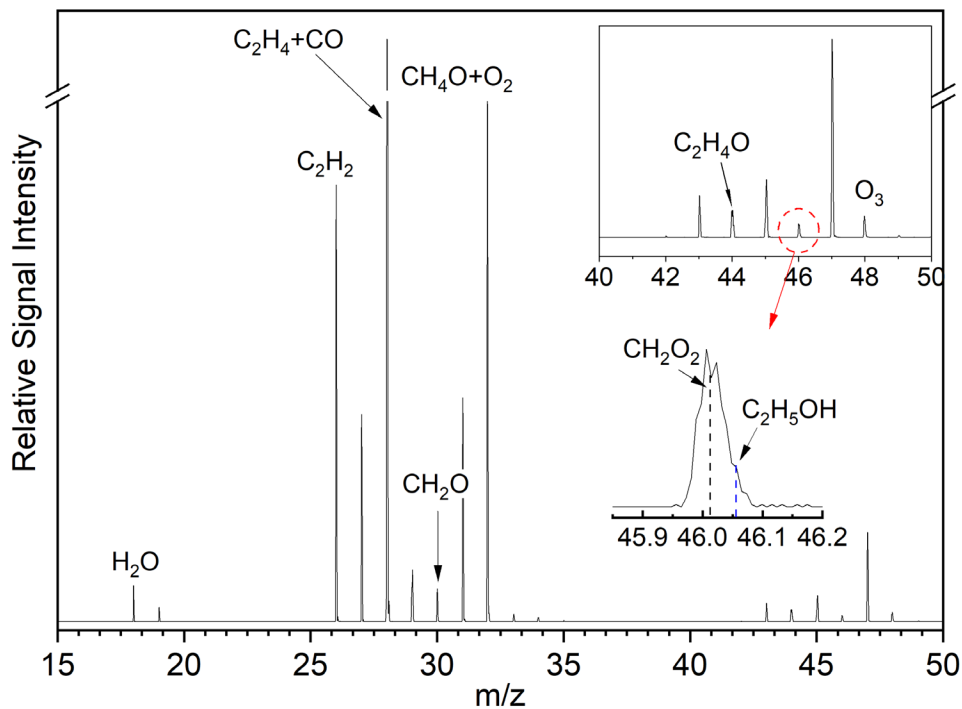


Figure 6.1. The mass spectrum of O_3 initiated C_2H_4 oxidation at room temperature and atmospheric pressure, from $m/z = 15$ to 30 with fixed photon energy of 14.49 eV.

Due to proximity in molecular weights, the peaks of CH_2O_2 and $\text{C}_2\text{H}_6\text{O}$ could not be completely separated under mass resolution of $m/\Delta m \approx 2000$, which is shown by the inset in Figure 6.1. Being supplementary to the results by GC in Table 5, acetylene (C_2H_2) and ethanol ($\text{C}_2\text{H}_5\text{OH}$) are identified, whose PIE curves obtained by experiments are displayed in Figure 6.2(a) and (b) respectively as follows,

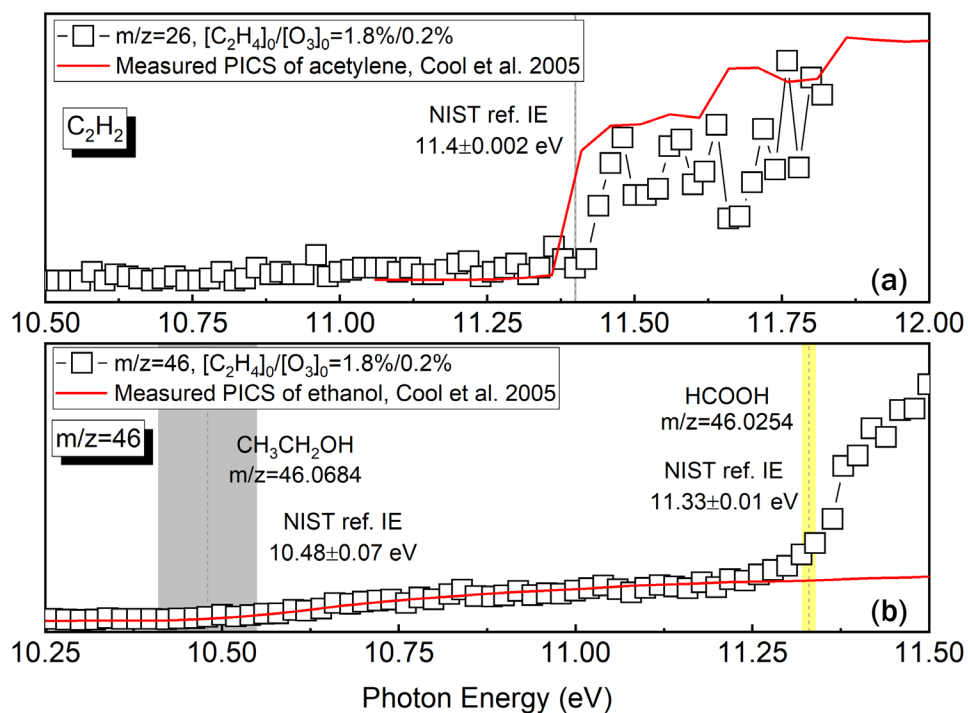


Figure 6.2. The PIE curves of (a) $m/z = 26$, C_2H_2 and (b) $m/z = 46$. The evaluated ionization energies from NIST are illustrated by shaded columns and measured PICS curves from Ref. [97] are overlapped.

By comparing the experimental results with evaluated ionization energies of C_2H_2 and C_2H_5OH , as well as the photoionization cross-section (PICS) measured by Cool et al. [97], perfect agreements are attained in terms of both ionization thresholds and line shapes. Despite the subtle difference in mass numbers, Figure 6.2(b) shows the C_2H_5OH could be successfully distinguished from $HCOOH$ by the ionization energies.

If the evaluated ionization energy of interested species is not available in either NIST database or any other reference, the quantum chemistry calculation is then performed to determine the adiabatic ionization energy (AIE) in theory. In this chapter, for most characterized products, the long-validated CBS-APNO method is used to calculate the energies of species proposed by experimental results. All presented quantum chemistry

calculations in this chapter and next are conducted by Xiaoqing Wu in Prof. Feng Zhang's group at NSRL, Hefei, China.

In general, more than 50 species have been characterized using the flow reactor and SRPI-MBMS, including both stable compounds and reactive radicals. Based on determined molecular structures, it is reasonable to propose that they are mostly generated via the secondary reactions following the ozonolysis of C₂H₄, and could be categorized into alcohol, aldehyde and peroxy by their functional groups.

6.3 Alcohol

In Table 7, all identified alcohols in O₃ initiated C₂H₄ oxidation at ambient temperature are summarized. The column of Exp. IE (eV) shows the measured ionization threshold from corresponding PIE curve, with uncertainty of ±0.01 eV. The column of Ref. IE (eV) gives the reference ionization energy, whose source is noted by the superscript, which could be either measured by experiments or calculated by quantum chemistry theory.

Table 7. Summary of identified alcohols in O₃ initiated C₂H₄ oxidation at room temperature.

m/z	Species	Name	Exp. IE (eV)	Ref. IE (eV)
32	CH ₃ OH	methanol	10.81±0.01	10.84±0.01 ^[NIST]
44	CH ₂ =CHOH	ethenol	9.22±0.01	9.18 ^[98]
46	C ₂ H ₅ OH	ethanol	10.42±0.01	10.48±0.07 ^[NIST]
58	CH ₂ =CHCH ₂ OH [†]	2-propen-1-ol	9.67±0.01	9.67±0.03 ^[NIST]
60	HOCH=CHOH [†]	ethen-1,2-diol	9.52±0.01	9.50±0.1 [this work, CBS-APNO]

[†] *Species characterized for the first time*

Both alkyl alcohols and enols are identified, and it is strongly believed that all of them are delivered by secondary reactions following C₂H₄+O₃. Referring to the HP-Mech

[67, 68] and USC Mech II [70], in the low-temperature oxidation of C₂H₄, CH₃OH could be mainly generated via two individual pathways,



If fact, it has been suggested [99, 100] both theoretically and experimentally the importance of reaction R24 in atmospheric CH₃OH formation. Although no prediction is given by both reference mechanisms (HP-Mech and USC Mech II) regarding C₂H₅OH production, formation pathways similar to R24 and R25 could be reasonably expected.

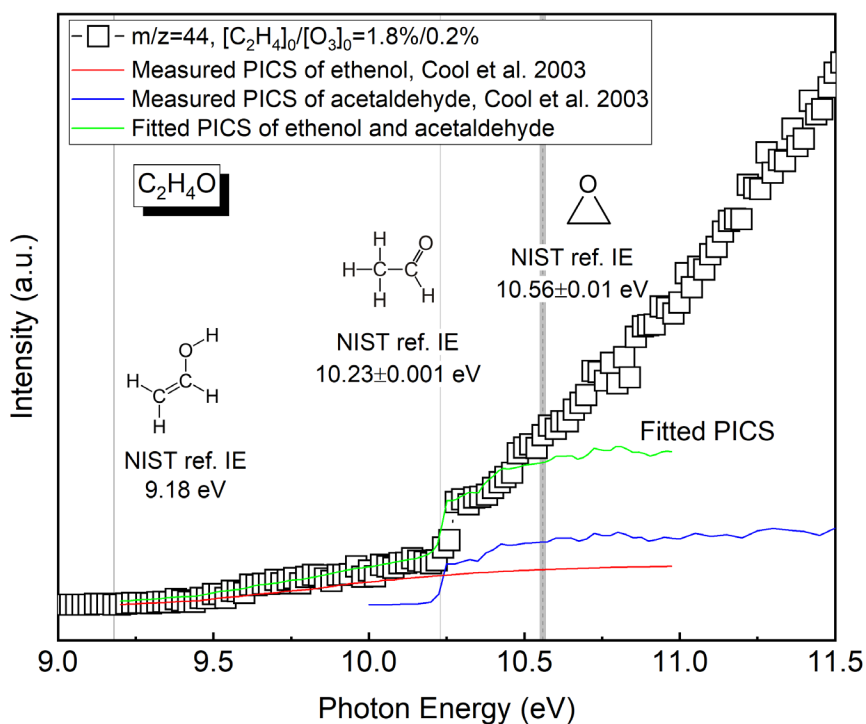
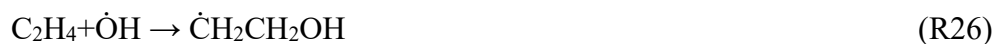


Figure 6.3. The PIE curve of $m/z = 44$. Measured PICS curves of ethenol (red) and acetaldehyde (blue) from Ref. [101] are given. Fitted PICS (green) with combined ethenol and acetaldehyde is superimposed on experimental data.

Enols have been recognized as common intermediates in hydrocarbon oxidation process [102]. Two enols have been characterized in this work, which are ethenol ($\text{CH}_2=\text{CHOH}$) and ethen-1,2-diol ($\text{HOCH}=\text{CHOH}$), and the latter one is detected for the first time in present chemical system. The experimental PIE curve of $m/z = 44$, $\text{C}_2\text{H}_4\text{O}$, is shown in Figure 6.3. It is clearly demonstrated that two apparent ionization thresholds exist at around 9.22 eV and 10.22 eV, which correspond to $\text{CH}_2=\text{CHOH}$ and CH_3CHO , respectively. The linear combination of the measured PICS of those two tautomers perfectly fits the PIE curve and therefore their existence is further validated. The discrepancy in line shape between PIE curve and fitted PICS initiates near the photon energy of 10.5 eV coinciding with the ionization of cyc- $\text{C}_2\text{H}_4\text{O}$, whose existence is also confirmed by GC in Chapter 5.

Based on kinetic simulation using the HP-Mech [67, 68], $\text{CH}_2=\text{CHOH}$ is majorly produced via the following reaction sequence starting from C_2H_4 ,



Although the one-step pathway of $\text{C}_2\text{H}_4 + \dot{\text{O}}\text{H} \rightarrow \text{CH}_2=\text{CHOH} + \dot{\text{H}}$ is also kinetically allowable, however, Zhu et al. [103] theoretically proposed that this channel would only be competitive at $T > 800$ K.

Figure 6.4(a) and (b) demonstrate the PIE curves of $m/z = 58$ and $m/z = 60$ with photon energy of 9.3-10.75 eV respectively. For better demonstration purpose, the intensity

of PIE curve of $m/z = 60$ in Figure 6.4(b) is multiplied by 10 within the photon energy range close to ionization.

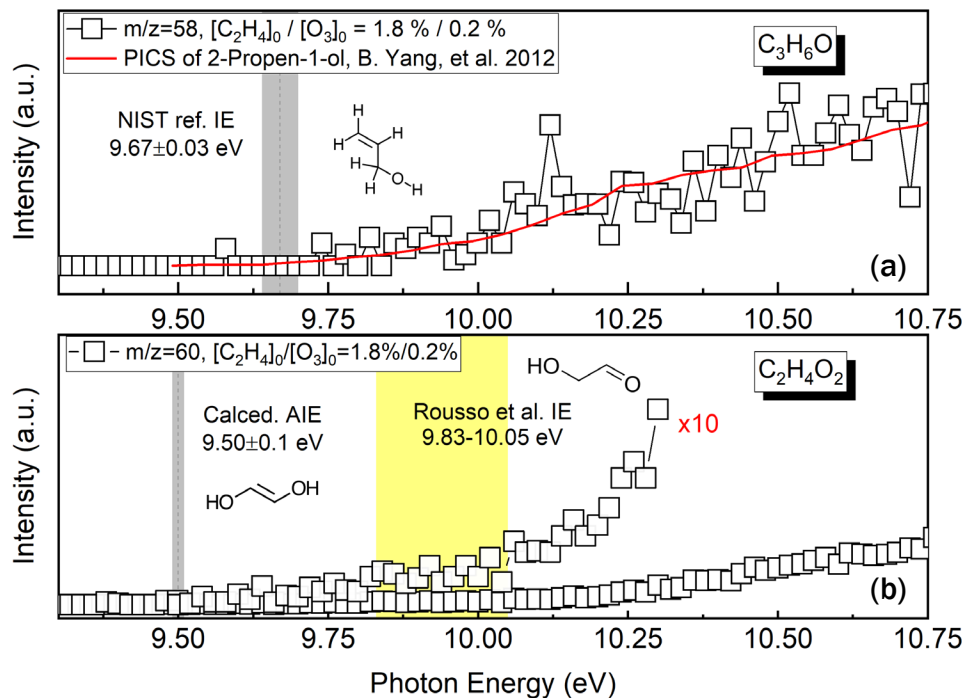


Figure 6.4. The PIE curves of (a) $m/z = 58$, C_3H_6O , and (b) $m/z = 60$, $C_2H_4O_2$. Measured PICS curve (red) of 2-propen-1-ol from Ref. [104] overlapped.

In Figure 6.4(a), the ionization threshold for $m/z = 58$ is close to 9.72 eV, which agrees fairly well with the evaluated IE of 2-propen-1-ol ($CH_2=CHCH_2OH$, also known as allyl alcohol). By overlapping the measured PICS data, the existence of 2-propen-1-ol is further confirmed. Analogous to the formation of CH_3OH through R24, it is possible that this allyl alcohol could be produced via $CH_2=CHCH_2OO\dot{O} + \dot{O}H \rightarrow CH_2=CHCH_2OH + O_2$, where the existence of allylperoxy radical, $CH_2=CHCH_2OO\dot{O}$, in present chemical system will be demonstrated in Chapter 7.

In Figure 6.4(b), the first threshold can be recognized close to 9.50 eV, conforming to the calculated AIE of ethen-1,2-diol ($HOCH=CHOH$) at CBS-APNO level of theory. As

photon energy is increased, a weak inflection point shows up at around 10.04 eV on the PIE curve, which coincides to the ionization of glycolaldehyde (HOCH₂CHO). No possible formation pathway with respect to HOCH=CHOH can be proposed for now.

6.4 Aldehyde

Table 8. Summary of identified aldehydes in O₃ initiated C₂H₄ oxidation at room temperature.

m/z	Species	Name	Exp. IE (eV)	Ref. IE (eV)
30	CH ₂ O	formaldehyde	10.89±0.01	10.88±0.01 ^[NIST]
44	CH ₃ CHO	acetaldehyde	10.22±0.01	10.23±0.001 ^[NIST]
56	CH ₂ =CHCHO [†]	acrolein	10.06±0.01	10.11±0.01 ^[NIST]
58	(CHO) ₂ [†]	glyoxal	10.20±0.01	10.2 ^[NIST]
60	HOCH ₂ CHO	glycolaldehyde	10.04±0.01	9.83-10.05 ^[65]

[†] Species characterized for the first time

The summary of identified aldehydes is given in Table 8. Not surprisingly, CH₂O is detected in enormous amount. Being consistent to the results by GC, CH₃CHO is characterized in this work using SRPI-MBMS. Although CH₂=CHOH is unstable and tend to isomerize into CH₃CHO via 1,3-H migration in condensed phase, however, in gas-phase reaction, the corresponding tautomerization would have sizable energy barrier due to lack of catalyst. In the HP-Mech [67, 68], it is recommended that the enol-aldehyde tautomerization is the dominant CH₃CHO formation pathway catalyzed by the $\dot{\text{H}}$ radical,



Other common radicals such as HO $\dot{\text{O}}$ [105] has also been proposed theoretically in the capability to catalyze such tautomerization in gas-phase reaction. A similar kinetic pathway

may be feasible between HOCH₂CHO and HOCH=CHOH, however, no relevant study has been reported yet and more theoretical work is required.

The PIE curves of two newly characterized aldehydes, acrolein (CH₂=CHCHO) and glyoxal ((CHO)₂), are shown in Figure 6.4(a) and (b), respectively.

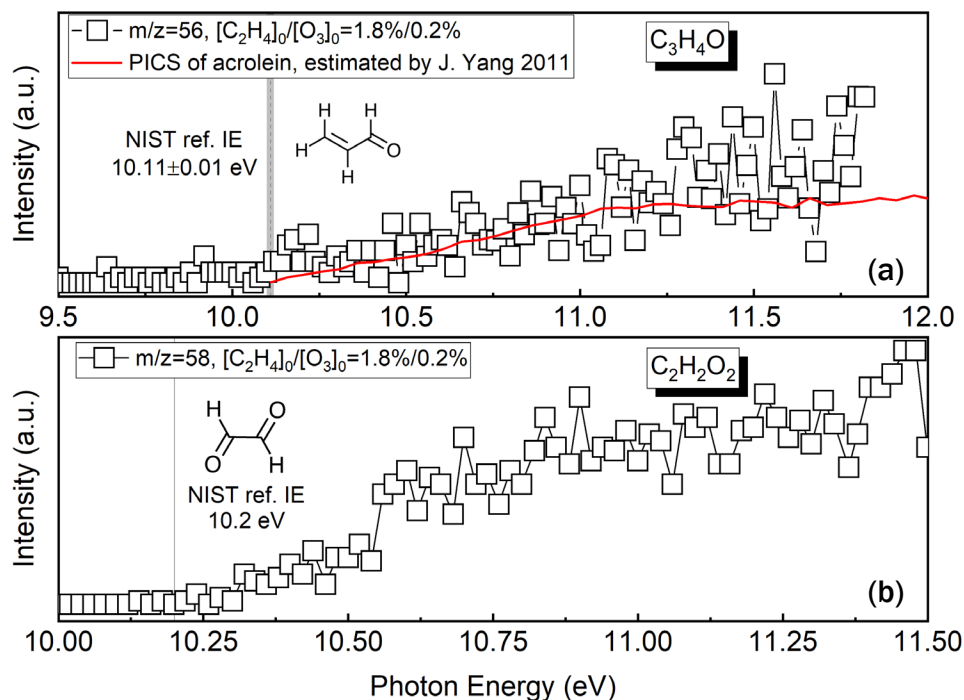


Figure 6.5. The PIE curves of (a) $m/z = 56$, C_3H_4O , and (b) $m/z = 58$, $C_2H_2O_2$. Estimated PICS curve of acrolein is superimposed.

Being the simplest unsaturated aldehyde, CH₂=CHCHO is newly identified in present room-temperature oxidation and could be possibly produced via the reaction of C₂H₄+H $\dot{C}O \rightarrow CH_2=CHCHO+H$ [106]. Even though this chain-propagating reaction needs to overcome an energy barrier higher than 14 kcal/mole, the energy released from C₂H₄ ozonolysis reaction might allow this pathway to be kinetically accessible in the current reaction scheme. Harding and Goddard [39] proposed that in C₂H₄ ozonolysis reaction,

(CHO)₂ could be potentially generated by dissociation of HCOCH₂OOH from the POZ biradical as follows,



Very recently, the reaction sequence of R4, R29 and R30 was supported by quantum chemistry calculations [107]. Based on calculated relative potential energies, it was suggested that the formation of trans-glyoxal is favored both kinetically and thermodynamically. The successful identification of (CHO)₂ here could serve as the first-time-ever experimental evidence to the proposed reaction pathway above.

6.5 Hydroperoxide

In this work, multiple hydroperoxides are experimentally characterized using the SRPI-MBMS. With the results from quantum chemistry calculations, great diversity is observed in determined molecular structures, and therefore additional subcategorization can be proceeded.

6.5.1 *sCI Insertion and Oligomerization*

The first group of hydroperoxides possess similar molecular structures with identical O-CH₂OO-H or -CH₂OO- insertion as moiety. It is proposed that this group should be generated via the bimolecular reaction of vibrationally stabilized CH₂OO, i.e., *sCI*, with alcohols, aldehydes, organic acids and other hydroperoxides. With enough *sCI*

being provided by the ozonolysis of C₂H₄, continuous oligomerization could happen and results in the formation of heavy hydroperoxides. The summary of this group is tabulated in Table 9, and the potential parent species based on calculated molecular structures are suggested.

Table 9. Summary of identified hydroperoxides produced by sCI bimolecular reactions in O₃ initiated C₂H₄ oxidation at room temperature.

m/z	Species	Parent Species	Exp. IE (eV)	Ref. IE (eV)
64	HOCH ₂ OH	H ₂ O	9.55±0.01	9.60±0.1 ^[This work, CBS-APNO]
74	C ₃ H ₅ OOH	C ₂ H ₄	9.36±0.01	9.44±0.1 ^[This work, CBS-APNO]
78	CH ₃ OCH ₂ OOH	CH ₃ OH	9.54±0.01	9.56±0.1 ^[66]
80	HOCH ₂ OOH	H ₂ O ₂	9.90±0.01	9.89±0.1 ^[66]
90	C ₂ H ₃ OCH ₂ OOH [†]	CH ₂ =CHOH	9.50±0.01	9.51±0.1 ^[This work, CBS-APNO]
92	C ₂ H ₅ OCH ₂ OOH	C ₂ H ₅ OH	9.24±0.01	9.23±0.1 ^[This work, CBS-APNO]
92	HC(O)OCH ₂ OOH [†]	HCOOH	10.24±0.01	10.16±0.1 ^[This work, CBS-APNO]
106	HCOCH ₂ OCH ₂ OOH [†]	HOCH ₂ CHO	9.60±0.01	9.64±0.1 ^[This work, CBS-APNO]
136	C ₂ H ₃ O[CH ₂ OO] ₂ H [†]	CH ₂ =CHOH	9.12±0.01	9.12±0.1 ^[This work, CBS-APNO]
138	HC(O)O[CH ₂ OO] ₂ H [†]	HCOOH	9.50±0.01	9.46±0.1 ^[This work, CBS-APNO]

[†] Species characterized for the first time

Up to now, the highest order oligomer characterized in this work is m/z = 138, HC(O)O[CH₂OO]₂H, whose parent species is HCOOH and has two sCI insertions. With high initial concentrations of C₂H₄ and O₃, the reaction rate of sCI oligomerization could be quite noticeable. Strong signals of some determined oligomers have been recorded by SRPI-MBMS, indicating their potentially high abundance even with residence time no

longer than 1.2 s in the flow reactor. The highly oxygenated oligomers are believed to be closely associated with the formation of extremely low-volatility organic compounds (ELVOCs) in Earth's atmosphere. As illustrated by the direct photographs in Figure 6.6(a) and (b), after the PIE scanning, substantial amount of liquid sample with high viscosity could be collected from the inner wall of flow reactor. The liquid has pungent odor similar to aldehydes and faint yellow color. No apparent vaporization would occur even when evacuating the flow reaction down to $P \approx 1$ torr. This phenomenon directly indicates the extremely low saturated vapor pressures of the constituents in the liquid. Further investigations are strongly encouraged to learn more about the ELVOC as observed and its possible influence on the O_3 assisted combustion.



Figure 6.6. Direct photographs of (a) highly viscous liquid accumulated on the inner wall of the flow reactor and (b) liquid sample collected with pungent odor and faint yellow color.

6.5.2 Ozonolysis Mechanism

The second group of characterized hydroperoxides are believed to be those intrinsically generated by ozonolysis channels, including SOZ and relative keto-hydroperoxide formed via stepwise POZ decomposition (see Figure 2.3). The identified hydroperoxides in this category is summarized in Table 10.

Table 10. Summary of identified hydroperoxides produced by ozonolysis channels in O₃ initiated C₂H₄ oxidation at room temperature.

m/z	Species	Name	Exp. IE (eV)	Ref. IE (eV)
76	cyc-OOCH ₂ OCH ₂	1,2,4-Trioxolane	9.70±0.01	9.68±0.1 ^[65]
76	HCOCH ₂ OOH	hydroperoxyl acetaldehyde	9.78±0.01	9.80±0.1 ^[65]
90	cyc-OOCH(CH ₃)OCH ₂ †	3-methyl-1,2,4-trioxolane	9.42±0.01	9.44±0.1 ^[66]

† Species characterized for the first time

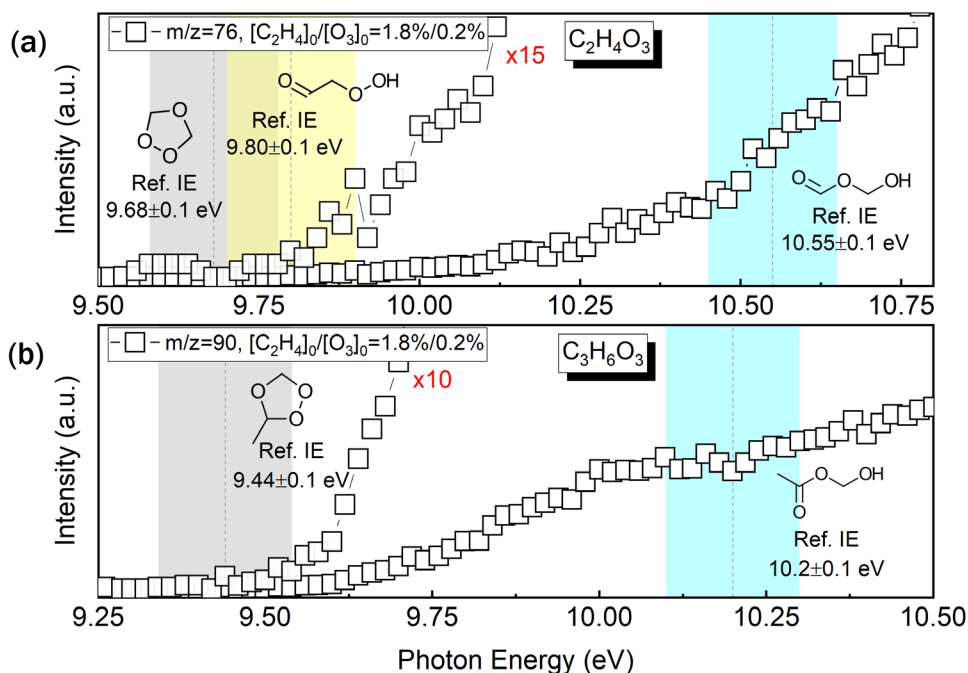


Figure 6.7. The PIE curves of (a) m/z = 76, C₂H₄O₃ and (b) m/z = 90, C₃H₆O₃. Ref. IEs are given in shaded columns for SOZ (grey), keto-hydroperoxide (yellow) and ester (blue), adopted from Rouso et al. [65, 66].

In this work, two different SOZs are detected at room temperature. Being additional to the 1,3,4-trioxolane (cyc-OOCH₂OCH₂), which is the SOZ of C₂H₄, the corresponding SOZ of propene (C₃H₆), 3-methyl-1,2,4-trioxolane (cyc-OOCH(CH₃)OCH₂) is characterized as well. The experimental PIE curves of m/z = 76, C₂H₄O₃, and m/z = 90, C₃H₆O₃, are shown in Figure 6.7(a) and (b), respectively. For m/z = 76, a weak but noticeable ionization threshold appears near 9.70 eV, which agrees to the calculated ionization energy 9.68 eV of cyc-OOCH₂OCH₂ by Roussio et al. [65] at CCSD(T)/CBS//M06-2X/cc-pVTZ level of theory. However, due to the proximity in calculated ionization energy of hydroperoxyl acetaldehyde (HCOCH₂OOH), extra theoretical evidence is preferred, e.g., simulated PIE data, so that the characterization of cyc-OOCH₂OCH₂ could be unambiguous. As stated in Chapter 2.2.3, the high-level calculation [41] suggested further cleavage pathway of SOZ may be proceeded in gas-phase reaction, due to sizable energy release from the 1,3-cycloaddition of sCI onto aldehyde or ketone, and the result would be the production of ester. Under the present experimental condition, however, no convincing evidence is observed for hydroxymethyl formate (HC(O)OCH₂OH) using SRPI-MBMS.

For m/z = 90, Figure 6.7(b) clearly illustrates the distinct ionization thresholds presented on the PIE curve at around 9.46 eV and 10.2 eV, which corresponds to SOZ cyc-OOCH(CH₃)OCH₂ and hydroxymethyl acetate (CH₃C(O)OCH₂OH), respectively. Although C₃H₆ is not one of the reactants, the sCI may directly combine with CH₃CHO via cycloaddition and yield cyc-OOCH(CH₃)OCH₂.

6.5.3 Low-Temperature Oxidation Mechanism

The third group of characterized hydroperoxides are proposed to be generated via the traditional low-temperature oxidation mechanism, which is initiated from the combination of fuel radical and O₂, i.e., $\dot{R} + O_2 \rightarrow RO\dot{O} \rightarrow ROOH$. The identified hydroperoxides in this category are summarized in Table 11. Instead of the CBS-APNO method applied in previous sections, the energies of ROOH in this section are determined with the DLPNO-CCSD(T) method for higher accuracy but meanwhile with higher computational cost.

Table 11. Summary of identified hydroperoxides produced via the tradition low-temperature fuel oxidation mechanism in O₃ initiated C₂H₄ oxidation at room temperature.

m/z	Species	Name	Exp. IE (eV)	Ref. IE (eV)
34	H ₂ O ₂	hydrogen peroxide	10.62±0.01	10.58±0.04 ^[NIST]
48	CH ₃ OOH	methyl hydroperoxide	9.82±0.01	9.75 ^[This work, DLPNO-CCSD(T)]
62	CH ₃ OOCH ₃ [†]	dimethyl peroxide	9.14±0.01	9.13 ^[This work, DLPNO-CCSD(T)]
62	C ₂ H ₅ OOH	ethyl hydroperoxide	9.54±0.01	9.53 ^[This work, DLPNO-CCSD(T)]
78	HO(CH ₂) ₂ OOH	2-hydroxyethyl hydroperoxide	9.86±0.01	9.86 ^[This work, DLPNO-CCSD(T)]

[†] Species characterized for the first time

Being one of the most prevalent intermediates in all low-temperature chemistries, hydrogen peroxide (H₂O₂) is detected in this room-temperature oxidation of C₂H₄. Based on the simulation using HP-Mech [67, 68], the formation of H₂O₂ is dominantly initiated through the chain-propagating steps rendering HO \dot{O} radical,



then two hydroperoxy radicals would combine into H_2O_2 , i.e., $\text{HO}\dot{\text{O}} + \text{HO}\dot{\text{O}} \rightarrow \text{H}_2\text{O}_2 + \text{O}_2$.

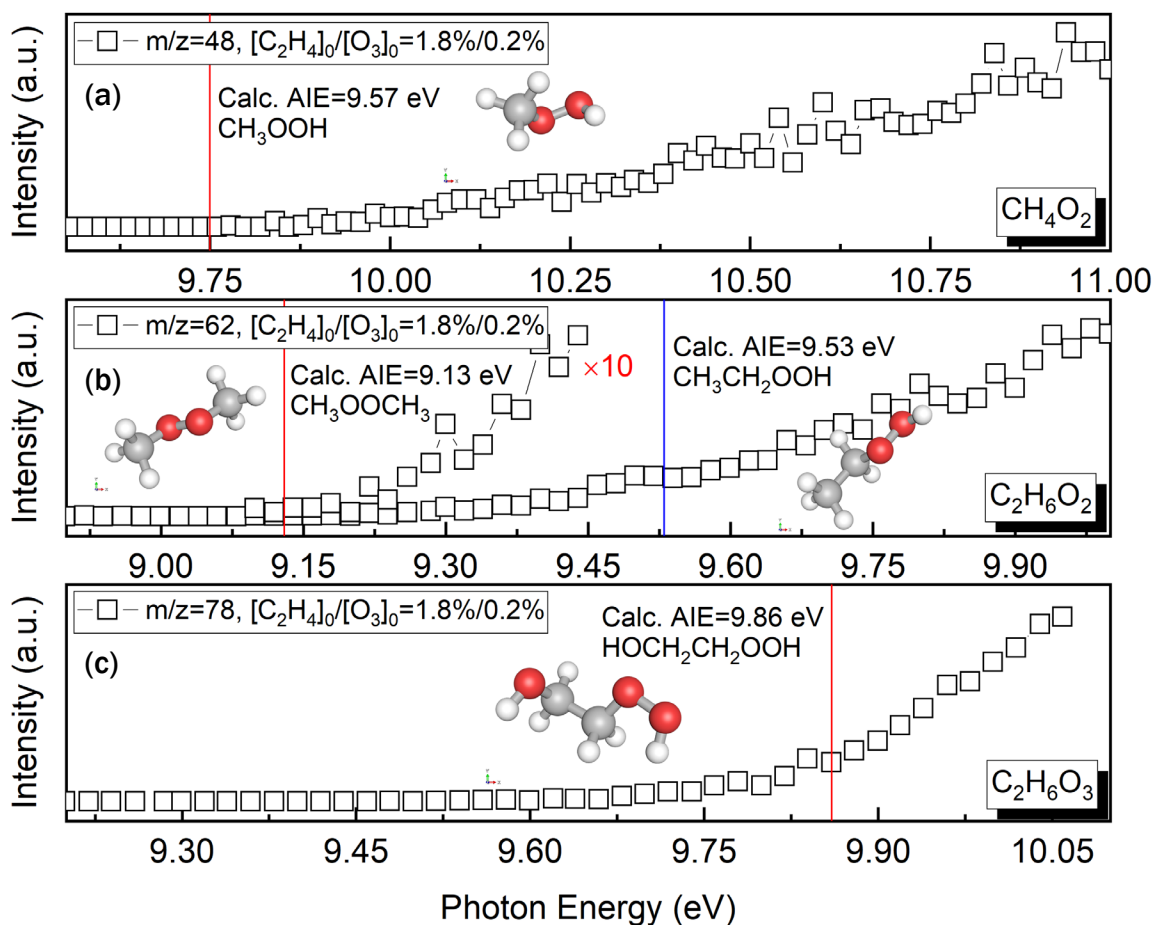


Figure 6.8. The PIE curves of (a) $m/z = 48$, CH_4O_2 , (b) $m/z = 62$, $\text{C}_2\text{H}_6\text{O}_2$ and (c) $m/z = 78$, $\text{C}_2\text{H}_6\text{O}_3$. The AIEs of ROOH are calculated at DLPNO-CCSD(T)/cc-pVQZ//B2PLYP-D3/cc-pVTZ level of theory and marked by the vertical lines.

The methyl hydroperoxide (CH_3OOH) should be formed from the intermolecular H atom abstraction between relevant methylperoxy radical ($\text{CH}_3\text{OO}\dot{\text{O}}$) and other H donors.

For example, the reaction channel could be $R_1\dot{O}O+R_2OOH \rightarrow R_1OOH+R_2\dot{O}O$ or $RO\dot{O}+H_2O_2 \rightarrow ROOH+HO\dot{O}$. The identified dimethyl peroxide (CH_3OOCH_3) is most likely generated by the self-condensation of $CH_3O\dot{O}$ radicals, i.e., $CH_3O\dot{O}+CH_3O\dot{O} \rightarrow CH_3OOCH_3+O_2$ [108]. The PIE curves of $m/z = 48$, CH_4O_2 , $m/z = 62$, $C_2H_6O_2$ and $m/z = 78$, $C_2H_6O_3$ are shown in Figure 6.8(a), (b) and (c) respectively. Excellent agreements are achieved between the measured ionization energies and the theoretical AIEs for both CH_3OOH and CH_3OOCH_3 . Additionally, two other hydroperoxides predicted by the low-temperature oxidation pathway of C_2H_4 with different fuel radicals, ethyl hydroperoxide (C_2H_5OOH) and 2-hydroxyethyl hydroperoxide ($HO(CH_2)_2OOH$), are both identified as well. Their corresponding peroxy radicals are detected and will be discussed in Chapter 7.

CHAPTER 7. DIRECT DETECTION OF ORGANIC PEROXY RADICALS IN OZONE INITIATED ETHYLENE OXIDATION AT ROOM TEMPERATURE

With intrinsically high yield of radical production, including $\dot{\text{O}}\text{H}$, $\text{H}\dot{\text{C}}\text{O}$ and sCl , such nature renders the ozonolysis reaction high prospect for efficiently promoting fuel oxidation at low-temperature conditions. Although the pivotal role of organic peroxy radicals has been widely acknowledged in autocatalytic low-temperature combustion chemistry [109-111], direct observation is still rare at relevant conditions due to their extremely short lifespans at such temperatures. Using the combination of SRPI-MBMS and high-level quantum chemistry calculations, four different $\text{RO}\dot{\text{O}}$ radicals are detected and rigorously characterized in this work. Based on the calculated molecular structures, it is postulated that these peroxy radicals are fundamentally derived from the reactions between C_2H_4 and free radicals, which are produced by either ozonolysis or subsequent secondary reactions. Such observation not only further reveals the unclear underlying chemistry about O_3 addition, but also serves as an experimental evidence for the existence of $\text{RO}\dot{\text{O}}$ radicals by the chain-propagating step, $\dot{\text{R}} + \text{O}_2 \rightarrow \text{RO}\dot{\text{O}}$, in a native low-temperature fuel oxidation, which was rarely observed in the past.

7.1 Experimental Boundary Conditions

In this work, the initial reactant concentrations are identical to the ones in Chapter 6, which are 1.8% C_2H_4 , 0.2% O_3 , 9.4% O_2 , and 88.6% Ar. Besides the experiment at atmospheric pressure ($P \approx 760$ torr at NSRL), the PIE scanning is also carried out at $P = 30$

torr in this work, under which the production of large compounds can be attenuated along with the possible ionized fragments from photofragmentation, so that the small species in the chemical system might be identified unambiguously. The low pressure is controlled by a throttle valve connected to a vacuum pump, and the residence time in the flow reactor is accordingly reduced to estimated 0.3 s. To obtain higher signal-to-noise ratio in the PIE scanning at $P = 30$ torr, the sampling time is extended to 600 s/step, and the photon energy is ranged from 9.2 eV to 10.7 eV at 0.025 eV/step.

7.2 Electronic Structure Calculations

The structures of the RO \dot{O} radicals are optimized by the density functional method of B2PLYP-D3 [112] with Dunning's augmented cc-pVTZ basis set. Grimme et al. [113] have investigated the impact of a series of DFT methods on the structure of organic compounds in the gas phase and suggested the smallest mean absolute variance of the B2PLYP-D3 method. In the present work, single point energies are refined using the domain based local pair-natural orbital coupled-cluster (DLPNO-CCSD(T)) [114, 115] method along with the cc-pVQZ basis set. The DLPNO-CCSD(T) method is beneficial to sort and select the most important excitation in electron correlation, and it possesses sufficient accuracy and significantly higher computational costs [116-118]. This method has been employed in previous studies [119-121] involving the ionization energy calculation for highly oxygenated cyclohexene ozonolysis products, iodide-based compounds and mononuclear copper complexes. The spin expectation value, $\langle S^2 \rangle$, is used to check for the possible spin contamination wave functions [122]. And the values of $\langle S^2 \rangle$ for various peroxy radicals are provided in Table 12, which indicate a negligible spin-contaminated phenomenon. A scaled factor of 0.9830 was used for zero-point energy

correction [123]. The calculated AIEs are summarized in Table 12, and the detailed molecular geometry after optimization is listed in Table 13. All quantum chemical calculations in this work are employed by the Gaussian09 package [124] except for the DLPNO-CCSD(T) calculations which are performed by the ORCA program package [125, 126].

Table 12. DLPNO-CCSD(T)/cc-pVQZ//B2PLYP-D3/cc-pVTZ energies of characterized RO₂ radicals in O₃ initiated C₂H₄ oxidation at T = 298 K.

m/z	Formula	$\langle s^2 \rangle$	Calc. AIE (eV)
47.013	CH ₃ O ₂	0.757	10.17
	CH ₃ O ₂ ⁺	2.015	
59.013	C ₂ H ₃ O ₂	0.764	9.91
	C ₂ H ₃ O ₂ ⁺	/	
61.029	C ₂ H ₅ O ₂	0.758	9.52
	C ₂ H ₅ O ₂ ⁺	2.018	
77.024	C ₂ H ₅ O ₃	0.756	9.62/9.74
	C ₂ H ₅ O ₃ ⁺	2.023	

Table 13. Bond distances (Å) and angles (deg) optimized at the B2PLYP-D3/ cc-pVTZ Level of Theory.

Species	Structure	R _{Ca-Cb} /R _{0-Ca}	R _{Ca-O}	R _{O-O}	∠C _a OO	θ ^α
CH ₃ O ₂	CH ₃ OO·	/	1.44	1.32	111	/
CH ₃ O ₂ ⁺		/	1.65	1.22	120	/
C ₂ H ₃ O ₂	CH ₂ =CHOO·	1.32	1.39	1.32	112	-180
C ₂ H ₃ O ₂ ⁺		1.37	1.34	1.28	117	180
C ₂ H ₅ O ₂	CH ₃ CH ₂ OO·	1.51	1.46	1.32	111	180
C ₂ H ₅ O ₂ ⁺		1.43	2.1	1.21	121	-180
C ₂ H ₅ O ₃	HOCH ₂ CH ₂ OO·	1.52	1.42	1.45	107	175
C ₂ H ₅ O ₃ ⁺		1.68	1.36	1.4	108	77

7.3 CH₃OO and C₂H₅OO

Both methylperoxy and ethylperoxy radicals, i.e., CH₃OO· and C₂H₅OO·, are probed and characterized. The corresponding PIE curves of m/z = 47 and m/z = 61 are shown in Figure 7.1(a) and (b) respectively, at both P = 30 torr and P = 760 torr (i.e., atmospheric pressure at NSRL). The calculated AIEs are marked by the red vertical lines for reference.

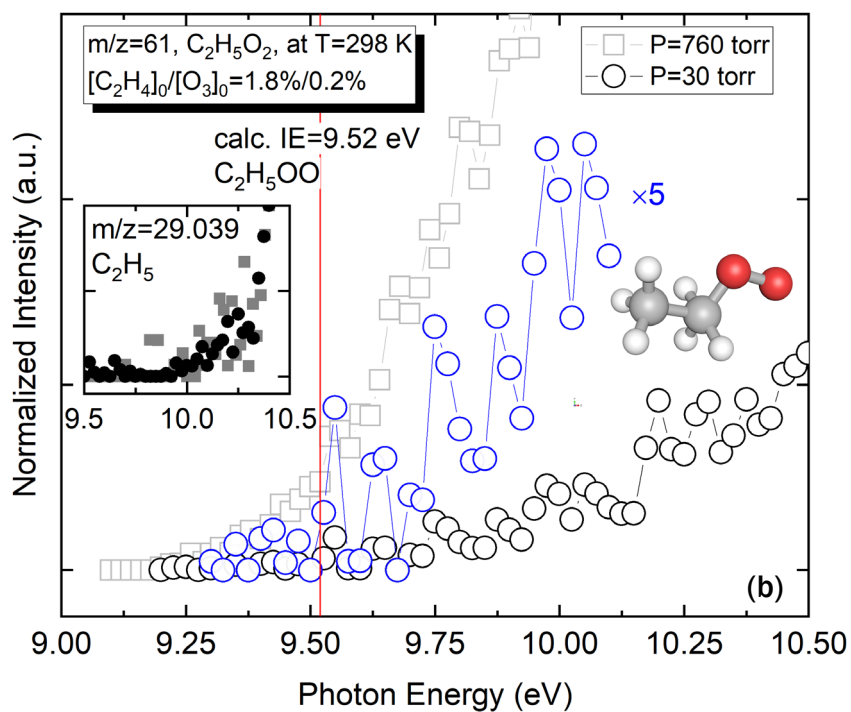
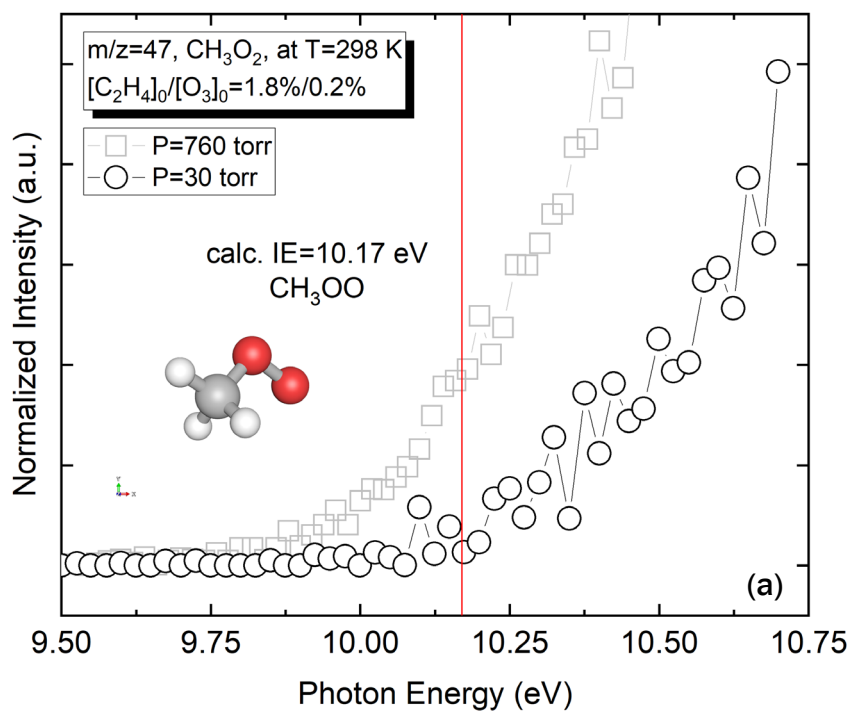
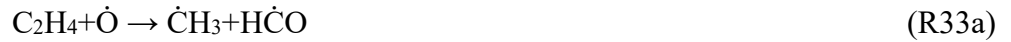


Figure 7.1. Experimental PIE curves of (a) $m/z = 47$, CH₃O₂, and (b) $m/z = 61$, C₂H₅O₂, with inset of C₂H₅, recorded at both P = 30 torr with 0.025 eV/step, and P = 760 torr with 0.02 eV/step. Calculated AIEs are marked by vertical lines in red.

The comparison between experimental results at low and atmospheric pressures, i.e., $P = 30$ torr and $P = 760$ torr, clearly demonstrates the disadvantage of ionized fragments on determination of small radicals. For example, regarding CH_3O_2 as shown in Figure 7.1(a), the much lower appearance energy of CH_3O_2^+ near 9.86 ± 0.01 eV at $P = 760$ torr should most likely be induced by photofragmentation of certain products, though no further information on the parent species is available at this time. For the case of $P = 30$ torr, the reduced pressure in the flow reactor effectively suppresses the undesired signal from photofragmentation, by decreasing the production of dissociative parent species. The PIE curve recorded at $P = 30$ torr clearly shows the ionization threshold near 10.174 ± 0.0125 eV, which well agrees to the calculated AIE of 10.17 eV, corresponding to the transition of $\text{CH}_3\text{O}\dot{\text{O}} (\tilde{X}^2A'') + h\nu \rightarrow \text{CH}_3\text{O}\dot{\text{O}}^+ (\tilde{X}^3A'') + e^-$.

For $\text{C}_2\text{H}_5\text{O}_2$ as shown in Figure 7.1(b), similar interference from ionized fragments is seen at $P = 760$ torr. By reducing the reactor pressure to $P = 30$ torr, it is perceived that the PIE curve starts vibrating strongly near 9.50 ± 0.0125 eV, which reasonably matches the calculated ionization energy of 9.52 eV for the transition of $\text{C}_2\text{H}_5\text{O}\dot{\text{O}} (\tilde{X}^2A'') + h\nu \rightarrow \text{C}_2\text{H}_5\text{O}\dot{\text{O}}^+ (\tilde{X}^3A'') + e^-$. The absence of sharp threshold in the PIE curve of $\text{C}_2\text{H}_5\text{O}_2$ implies a relatively low cation density. This could be rationalized by the dissociative ionization, $\text{C}_2\text{H}_5\text{O}\dot{\text{O}}^+ \rightarrow \dot{\text{C}}\text{H}_2\text{CH}_3^+ + \text{O}_2$, as proposed by Meloni et al. [127], based on potential energy calculations using CBS-APNO method. Actually, no PIE curve of $\text{C}_2\text{H}_5\text{O}\dot{\text{O}}$ was experimentally reported in their study [127] due to poor signal-to-noise ratio, but only the observation of C_2H_5 fragments with appearance energy close to 10.0 eV. The insetted PIE curves of C_2H_5 at both $P = 760$ torr and $P = 30$ torr in Figure 7.1(b) corroborate such observation, which therefore further confirms the existence and detection of $\text{C}_2\text{H}_5\text{O}\dot{\text{O}}$ here.

It is believed that both detected $\text{CH}_3\text{O}\dot{\text{O}}$ and $\text{C}_2\text{H}_5\text{O}\dot{\text{O}}$ are derived through traditional low-temperature oxidation channels, i.e., $\dot{\text{R}}+\text{O}_2 \rightarrow \text{RO}\dot{\text{O}}$, where $\dot{\text{R}}$ represents the fuel radical. The directly ozonolysis produced $\dot{\text{O}}\text{H}$, $\dot{\text{H}}$ and $\text{H}\dot{\text{C}}\text{O}$, together with other radicals by secondary reactions, especially the ones with O_2 and O_3 in present case, would then attack the fuel molecule C_2H_4 , rendering different fuel radicals. Referred to the HP-Mech [67, 68], for methyl radical ($\dot{\text{C}}\text{H}_3$), the two dominant production channels are,



and the other two-step channel,



where the $\dot{\text{O}}$ radical is produced by $\text{CH}_2=\dot{\text{C}}\text{H}+\text{O}_2 \rightarrow \text{CH}_2=\text{CH}\dot{\text{O}}+\dot{\text{O}}$, and $\dot{\text{H}}+\text{O}_3 \rightarrow \text{HO}\dot{\text{O}}+\dot{\text{O}}$ at low temperatures. Both theoretical [128] and experimental [129] studies of reaction $\text{C}_2\text{H}_4+\dot{\text{O}}$ revealed that the branching ratio between R33a and R33b is approximately 0.6:0.35 at room temperature. For ethyl radical ($\dot{\text{C}}\text{H}_2\text{CH}_3$), the primary production channel should be solely as,



though other pathways of H transfer such as $\text{C}_2\text{H}_4+\text{H}\dot{\text{C}}\text{O} \rightarrow \dot{\text{C}}\text{H}_2\text{CH}_3+\text{CO}$ exists, however, because of the low reactivity [130] of formyl radical with respect to olefins, this channel is of minor importance. It is interesting to notice that the formations of both $\text{CH}_3\text{O}\dot{\text{O}}$ and

$C_2H_5OO\dot{O}$ involve \dot{H} radical, whose yield from ozonolysis of C_2H_4 has been theoretically suggested inadequate [41, 42]. In addition to $C_2H_4+O_3$, other secondary \dot{H} production pathways might contribute also, for instance, $CO+\dot{O}H \rightarrow CO_2+\dot{H}$ and $O_3+H\dot{C}O \rightarrow 2O_2+\dot{H}$.

Nevertheless, the possibility of other mechanisms leading to the probed $CH_3OO\dot{O}$ and $C_2H_5OO\dot{O}$ could not be ruled out completely. In a recent theoretical study [131], the barrierless addition of $\dot{O}H$ onto sCI, propanone oxide ($(CH_3)_2COO$), through the formation of C-O bond was proposed based on calculations. In the same manner, would $CH_3OO\dot{O}$ and $C_2H_5OO\dot{O}$ be possibly formed via $\dot{H}+CH_2OO$ and $\dot{C}H_3+CH_2OO$, respectively? Although many investigations focused on the bimolecular reactions regarding sCI, little attention has been paid for reactions between the zwitterion sCI and radicals. Further quantum chemical study and isotopic experiment with $^{18}O_3$ are strongly encouraged.

7.4 $CH_2=CHOO$ and $HOCH_2CH_2OO$

At low-temperature conditions, the reaction of $C_2H_4+\dot{O}H$ could proceed through three major channels. One of the channels leads to vinyl radical ($CH_2=\dot{C}H$) and H_2O , while another one is the formation of adduct 2-hydroxyethyl radical ($\dot{C}H_2CH_2OH$). The two fuel radicals could be rapidly captured by ambient O_2 and then yield to vinylperoxy, $CH_2=CHO\dot{O}$, and 2-hydroxyethylperoxy radical, $HOCH_2CH_2OO\dot{O}$, respectively. Their experimental PIE curves are demonstrated in Figure 7.2(a) and (b). It should be noted that for those two peroxy radicals, only results obtained at atmospheric pressure are presented and used for the radical determination, due to poor signal-to-noise ratio at $P = 30$ torr.

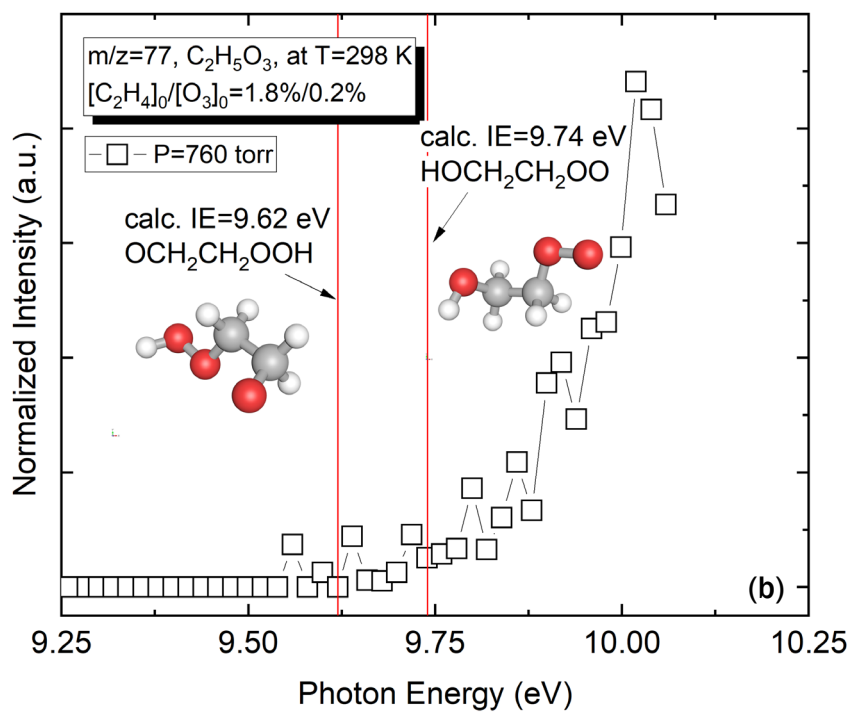
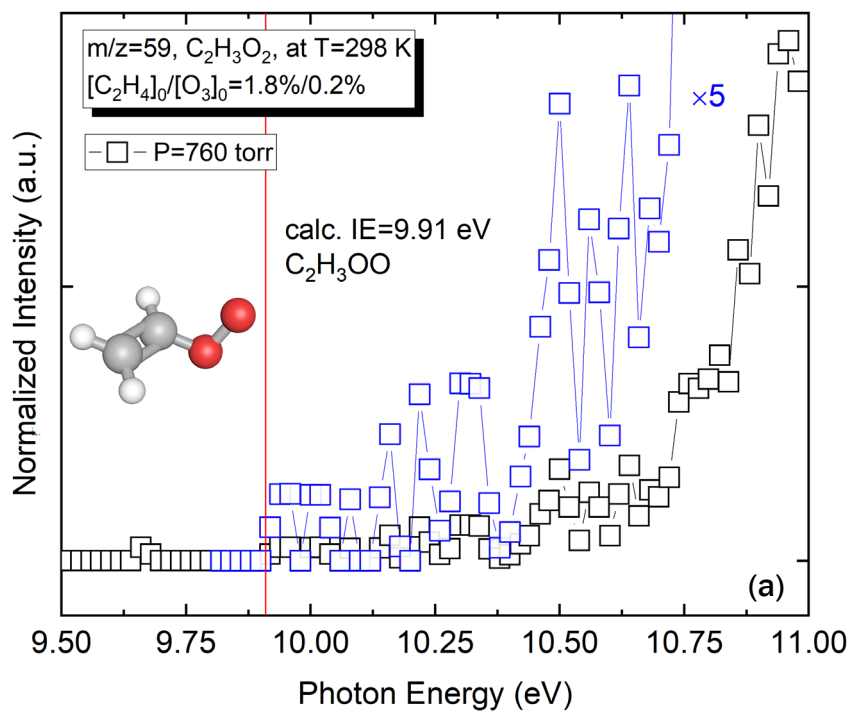


Figure 7.2. Experimental PIE curves of (a) $m/z = 59$, $C_2H_3O_2$, and (b) $m/z = 77$, $C_2H_5O_3$, recorded at $P = 760$ torr with 0.02 eV/step. Calculated AIEs are marked by vertical lines in red.

For $\text{CH}_2=\text{CHO}\dot{\text{O}}$, no sharp ionization threshold is perceived, instead, strong vibration in PIE curve starts at 9.90 ± 0.01 eV, which matches the calculated AIE of 9.91 eV. The near-limit detection indicates low density of $\text{CH}_2=\text{CHO}\dot{\text{O}}^+$ in current chemical system, however, this is not a result of dissociative ionization as shown for $\text{C}_2\text{H}_5\text{O}\dot{\text{O}}$ in Chapter 7.3. Based on the study regarding 1-alkenylperoxy radical by Meloni et al. [132], the photoionization process $\text{CH}_2=\text{CHO}\dot{\text{O}}+\text{h}\nu \rightarrow \text{CH}_2=\text{CHO}\dot{\text{O}}^++\text{e}^-$ removes the electron from antibonding molecular orbital of $\text{C}_\alpha-\text{O}$, and consequently stabilizes the peroxy radical cation. This agreed with the shortened $\text{C}_\alpha-\text{O}$ bond for $\text{CH}_2=\text{CHO}\dot{\text{O}}^+$ in our calculation in Table 13. Therefore, the observed low cation density is indeed caused by the lack of neutral $\text{CH}_2=\text{CHO}\dot{\text{O}}$ radical. Such outcome is aligned with the theory [103] that $\text{C}_2\text{H}_4+\dot{\text{O}}\text{H} \rightarrow \dot{\text{C}}\text{H}_2\text{CH}_2\text{OH}$ is the dominant channel at $T = 298$ K, due to higher energy barrier in the formation of $\text{CH}_2=\dot{\text{C}}\text{H}+\text{H}_2\text{O}$. Moreover, the calculations [133] regarding $\text{CH}_2=\dot{\text{C}}\text{H}+\text{O}_2$ suggested two other channels, $\text{CH}_2=\text{CH}\dot{\text{O}}+\dot{\text{O}}$ and $\text{H}\dot{\text{C}}\text{O}+\text{CH}_2\text{O}$, are also kinetically significant together with the formation of $\text{CH}_2=\text{CHO}\dot{\text{O}}$ at $T = 300$ K and $P = 760$ torr, whose reaction rate constants are on the same order. All these factors together yield the low abundance of $\text{CH}_2=\text{CHO}\dot{\text{O}}$ as observed in this work.

For $\text{C}_2\text{H}_5\text{O}_3$, ionization energies are calculated for the isomers of $\text{HOCH}_2\text{CH}_2\text{O}\dot{\text{O}}$ and 2-hydroperoxyethoxy radical ($\dot{\text{O}}\text{CH}_2\text{CH}_2\text{OOH}$), being $\text{IE}=9.74$ eV and $\text{IE}=9.62$ eV, respectively. As presented in Figure 7.2(b), the apparent onset of ionization near 9.62 ± 0.01 eV is in good agreement with the calculation of $\dot{\text{O}}\text{CH}_2\text{CH}_2\text{OOH}$. With increasing photon energy, another steeper rise in the PIE curve is noticed near 9.82 ± 0.01 eV, giving a 0.08 eV difference in reference to the calculated AIE value of $\text{HOCH}_2\text{CH}_2\text{O}\dot{\text{O}}$, which is at the edge of unambiguous characterization. It has been theoretically [134] proposed that the

1,5-intramolecular H shift, $\text{HOCH}_2\text{CH}_2\text{O}\dot{\text{O}} \leftrightarrow \dot{\text{O}}\text{CH}_2\text{CH}_2\text{OOH}$, via a strainless 6-member cyclic transition state is kinetically achievable, and the equilibrium in such isomerization process is favored, while the decomposition of $\dot{\text{O}}\text{CH}_2\text{CH}_2\text{OOH}$ is almost negligible at current experimental conditions.

7.5 Experiments with n-C₄H₁₀ Addition

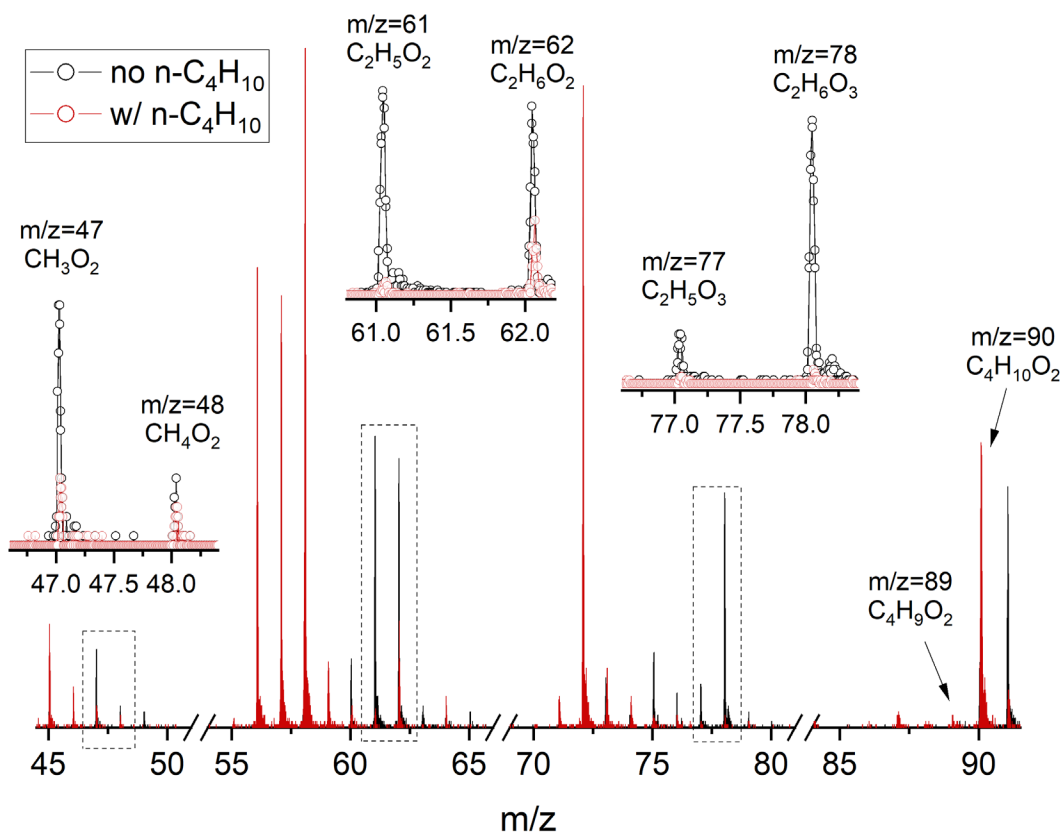


Figure 7.3. Mass spectrums with (in red) and without (in black) scavenger at ambient conditions, recorded with photon energy 10.5 eV. The added n-C₄H₁₀ concentration is 10 times the initial C₂H₄ concentration.

To further validate the existence and formation channels of detected RO $\dot{\text{O}}$ radicals, experiments with n-butane (n-C₄H₁₀) addition as a radical scavenger are conducted at ambient conditions. The comparison of reaction rate constants at T = 300 K, between C₂H₄

and n-C₄H₁₀ with respect to selected free radicals and O₃, are listed in Table 14. It reveals that n-C₄H₁₀ can be rather competitive with C₂H₄ in the reactions with $\dot{\text{O}}\text{H}$ radical, while showing much lower reactivity with respect to $\dot{\text{O}}$ and $\dot{\text{H}}$ radicals, and the reaction of n-C₄H₁₀+O₃ is negligible.

Table 14. Summary of reaction rate constants of C₂H₄ and n-C₄H₁₀ with respect to selected free radicals and O₃ at T = 300 K, in the unit of cm³/mole s.

<i>k</i> , cm ³ /mole s	C ₂ H ₄	n-C ₄ H ₁₀
$\dot{\text{O}}\text{H}$ [135]	5.08×10^{12}	1.54×10^{12}
$\dot{\text{H}}$ [136]	7.99×10^{11}	1.73×10^8
$\dot{\text{O}}$ [136]	4.33×10^{11}	1.18×10^{10}
O ₃ [137, 138]	1.01×10^6	6.85

In this section, low initial concentration of C₂H₄ is adopted, so that the result of radical scavenging by excessive n-C₄H₁₀ may be better observed experimentally. For the group without scavenger, the boundary condition is set to be 0.1% C₂H₄, 1.0% O₃, 14.8% O₂ and 84.1% Ar, with 1.2 s residence time in the flow reactor. For the control group with scavenger, 10% of n-C₄H₁₀ is added in the fuel stream and premixed with C₂H₄, meanwhile, same amount of Ar is removed to keep the initial concentrations of reactants and the flow residence time unchanged.

The overlapped mass spectrums of experiments with and without n-C₄H₁₀ is shown in Figure 7.3. The photon energy is fixed at 10.5 eV. It should be noticed that at such a photon energy level, though all four characterized peroxy radicals have been majorly ionized, the unfavored ionized fragments rise simultaneously along with the target peroxy cations. This is especially the case for CH₃O $\dot{\text{O}}$ and C₂H₅O $\dot{\text{O}}$, whose ionizations fall behind the appearance energies of the fragments, as already shown in Figure 7.1(a) and (b) at

atmospheric pressure. Accordingly, the presented mass peaks on the spectrum in Figure 7.3 is not necessarily referring to RO \dot{O} radicals only but could be the sum of RO \dot{O}^+ and fragment cations, causing difficulty in analysis. However, unlike those small peroxy radicals, their saturated hydroperoxides with much longer lifespan could be characterized and quantified rigorously free from issues with fragments. At atmospheric pressure, $m/z = 48$, CH₃OOH without other isomers, is identified in this work, which corroborates the observation by Rouso et al. [65]. Based on the low-temperature oxidation mechanism, the dominant production channel for CH₃OOH is through the chain-terminating pathway CH₃O \dot{O} +HO \dot{O} \rightarrow CH₃OOH+O₂. Therefore, the observed CH₃OOH should have direct correlation with CH₃O \dot{O} . Similarly, $m/z = 62$, C₂H₅OOH and $m/z = 78$, HOCH₂CH₂OOH could be considered as indicators for C₂H₅O \dot{O} and HOCH₂CH₂O \dot{O} , respectively.

As shown in Figure 7.3, the peaks of $m/z = 47$, 61 and 77, corresponding to CH₃O₂, C₂H₅O₂ and C₂H₅O₃, respectively, together with the peaks of correlated hydroperoxides are identified and enlarged as insets. However, the mass peak of C₂H₃O₂ is not fully recognizable under current boundary condition, which is most likely due to low abundance below detection limit. Following the addition of excess n-C₄H₁₀, signals for all interested m/z ratios, partially corresponding to the peroxy radicals, and their hydroperoxides uniformly decrease, especially for C₂H₅O₃ and C₂H₆O₃, where dramatic drop in relative intensity is observed. Although considerable decrease shows for both CH₃O₂ and C₂H₅O₂ peaks, it is interesting to notice much weaker reduction in the signals of correlated hydroperoxides CH₄O₂ and C₂H₆O₂ compared to C₂H₆O₃, which indicates a smaller effect of n-C₄H₁₀ scavenger on CH₃O \dot{O} and C₂H₅O \dot{O} , being contrary to HOCH₂CH₂O \dot{O} . This observation can be rationalized by the view that in the present oxidation system at room

temperature, the hydroxylperoxy radical is solely generated via the $\dot{\text{O}}\text{H}$ reaction channel, $\text{C}_2\text{H}_4+\dot{\text{O}}\text{H}$, while the other two alkylperoxy radicals are predominantly formed via $\text{C}_2\text{H}_4+\dot{\text{O}}$ and $\text{C}_2\text{H}_4+\dot{\text{H}}$, respectively, where the $\dot{\text{O}}$ radical is produced by secondary reactions of $\dot{\text{H}}$ and $\dot{\text{O}}\text{H}$ radicals. With large amount of n-C₄H₁₀ added, the $\dot{\text{O}}\text{H}$ radical from the ozonolysis of C₂H₄ would be greatly quenched, hindering the reaction of $\text{C}_2\text{H}_4+\dot{\text{O}}\text{H}$ and therefore the further formation of HOCH₂CH₂O $\dot{\text{O}}$. However, the $\dot{\text{H}}$ and $\dot{\text{O}}$ radical would experience weaker scavenging by the n-C₄H₁₀ due to lower reactivity, causing less attenuation in CH₃O $\dot{\text{O}}$ and C₂H₅O $\dot{\text{O}}$ formations.

7.6 Peroxy Radicals Derived from sCI Reaction

In addition to the four peroxy radicals produced through the classic $\dot{\text{R}}+\text{O}_2$ channel, other RO $\dot{\text{O}}$ radicals are also characterized with similar molecular structures, which are summarized in Table 15. The identical -CH₂O $\dot{\text{O}}$ moiety of these peroxy radicals strongly implies their possible connection with the sCI, i.e., CH₂O $\dot{\text{O}}$.

Table 15. Summary of identified RO $\dot{\text{O}}$ radicals possibly produced from bimolecular reaction of sCI at room temperature. All listed AIEs are calculated at DLPNO-CCSD(T)/cc-pVQZ//B2PLYP-D3/cc-pVTZ level of theory.

m/z	Formula	Structure	Parent Radical	Exp. IE (eV)	Calc. AIE (eV)
73	C ₃ H ₅ O ₂ [†]	CH ₂ =CHCH ₂ O $\dot{\text{O}}$	CH ₂ = $\dot{\text{C}}\text{H}$	9.87±0.01	9.92
89	C ₃ H ₅ O ₃ [†]	CH ₂ =CHOCH ₂ O $\dot{\text{O}}$	CH ₂ =CH $\dot{\text{O}}$	9.78±0.01	9.71
93	C ₂ H ₅ O ₄ [†]	CH ₃ OOCH ₂ O $\dot{\text{O}}$	CH ₃ O $\dot{\text{O}}$	9.82±0.01	9.78
123	C ₃ H ₇ O ₅ [†]	HO(CH ₂) ₂ OOCH ₂ O $\dot{\text{O}}$	HO(CH ₂) ₂ O $\dot{\text{O}}$	9.70±0.01	9.67

[†] Species characterized for the first time

With the help of quantum chemistry calculations, Vereecken et al. [139] and Anglada et al. [140] consistently proved the kinetic feasibility of bimolecular reaction between sCI and CH₃O $\dot{\text{O}}$ as follows,



assuming that the generated peroxide-substituted peroxy radical may have long enough lifespan to be finally thermalized. The unique electronic configuration confers certain amount of biradical feature to sCI at ground state. Analogous to the mechanism of R36, may other free radicals be able to react with sCI in a comparable manner? The potential parent radicals in the formation of identified $\text{RO}\dot{\text{O}}$ in Table 15 are postulated, whose existence have been either predicted by mechanism, i.e., $\text{CH}_2=\dot{\text{C}}\text{H}$ and $\text{CH}_2=\text{CH}\dot{\text{O}}$, or experimentally proven, i.e., $\text{CH}_3\text{O}\dot{\text{O}}$ and $\text{HO}(\text{CH}_2)_2\text{O}\dot{\text{O}}$, in this room-temperature oxidation of C_2H_4 .

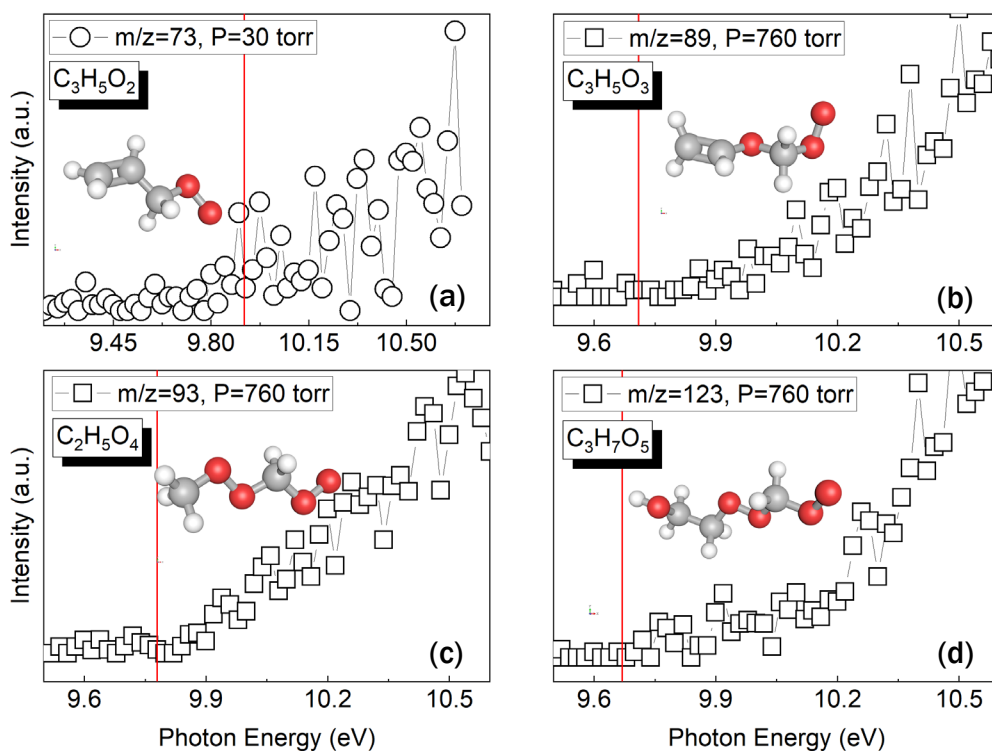


Figure 7.4. The PIE curves of (a) $m/z = 73$, $\text{C}_3\text{H}_5\text{O}_2$, (b) $m/z = 89$, $\text{C}_3\text{H}_5\text{O}_3$, (c) $m/z = 93$, $\text{C}_2\text{H}_5\text{O}_4$ and (d) $m/z = 123$, $\text{C}_3\text{H}_7\text{O}_5$. The calculated AIE at DLPNO-CCSD(T)/cc-pVQZ//B2PLYP-D3/cc-pVTZ level of theory is designated in red vertical line.

The PIE curves of RO \dot{O} radicals in Table 15 are given in Figure 7.4(a) to (d). The result shows reasonable agreement between the measured ionization thresholds and the relevant AIEs calculated at DLPNO-CCSD(T)/cc-pVQZ//B2PLYP-D3/cc-pVTZ level of theory for all four peroxy radicals. However, unlike the reaction sequence of $\dot{R}+O_2 \rightarrow RO\dot{O} \rightarrow ROOH$ in low-temperature oxidation, it has been revealed in Chapter 6.5.1 that the corresponding hydroperoxides, e.g., $CH_2=CHOCH_2OOH$, could be directly formed via the CH_2OO insertion. Therefore, the successful identification of RO \dot{O} radicals in Figure 7.4 is not necessarily the evidence for direct bimolecular reaction between sCI and other radicals. It is also plausible that these RO \dot{O} radicals are yielded via the $R_1O\dot{O}+R_2OOH \rightarrow R_1OOH+R_2O\dot{O}$ channel instead, with the ROOH being generated first. Detail quantum chemistry study on the reaction pathways between sCI and general radicals is necessitated, the result of this study might contribute greatly to both atmospheric chemistry and O_3 assisted combustion of unsaturated fuel at low temperatures.

CHAPTER 8. DYNAMICS OF LAMINAR ETHYLENE LIFTED FLAME WITH OZONE ADDITION

In this chapter, the effect of O₃ addition on C₂H₄ flame dynamics is studied using a non-premixed laminar co-flow jet flame burner. By tuning the co-flow composition, a stable C₂H₄ lifted flame is obtained in the laminar regime at room temperature and atmospheric pressure. Various flame dynamic behaviors are observed as a function of fuel jet velocity (u_f). Specifically, in the low u_f region, flame liftoff height, H_L , decreases with O₃ addition, while instead it increases in high u_f region. Planar laser-induced fluorescence (PLIF) of CH₂O and numerical simulations are performed to understand the highly coupled kinetic and dynamic process. The experimental set-up of jet flame burner and PLIF has been demonstrated in Chapter 3.6. The results and discussions demonstrated in this chapter have been published in the journal of Proceedings of the Combustion Institute. (Wu et al. [141])

8.1 Computational Framework

8.1.1 Numerical Set-up

The numerical simulations are conducted using ANSYS Fluent [72] in this work. Because of the simple geometry of the jet flame burner, to lower the computational cost, an axisymmetric 2-D computational domain is adopted with a size (axial \times radial) of 450 mm \times 45 mm. A gravitational acceleration of 9.79 m/s² is given in the negative axial direction so that the buoyancy effect could be accounted for. Regarding the types of boundaries, both fuel and oxidizer inlets are the velocity type with constant $T = 300$ K, and

the pressure-outlet is set with gauge pressure equals to zero. All walls in the computational domain are adiabatic and no-slip. The schematic of the 2-D computational domain together with structured meshes are illustrated in Figure 8.1, in which both geometric dimensions and boundary types are given. The aerodynamic shape of the fuel nozzle is kept in the 2-D simulations, with length of 11.1 mm in the axial direction and the nozzle exit of 0.345 mm in width.

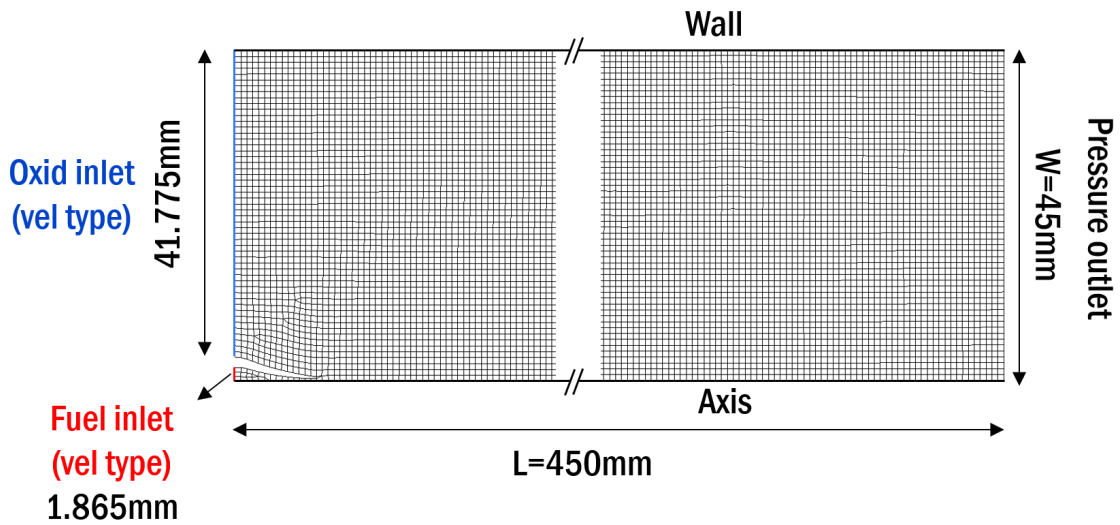


Figure 8.1. Schematic of the 2-D axisymmetric computation domain of the jet flame burner and the structured meshes.

All simulations, i.e., both non-reacting and reacting flow, are performed using the laminar model with energy equation solved. For species transportation, the thermal conductivity and viscosity of the mixture are calculated by the ideal gas mixing law, while the mass diffusivity of each species is given by the kinetic theory. In terms of the solution methods selection, the SIMPLEC algorithm is used for the pressure-velocity coupling, and the default second order upwind scheme is adopted for the spatial discretization of pressure, momentum, energy, and species. In reacting-flow simulations, the built-in CHEMKIN-CFD solver of laminar finite-rate chemistry is enabled. To ignite the established C₂H₄ jet

with O₂/N₂ co-flow, an instantaneous high-temperature (e.g., T = 2400 K) ignition kernel with radius of 1.5 mm is patched 8 mm downstream of the fuel nozzle exit, which will ideally develop into steady lifted flames at different liftoff heights according to the fuel jet velocities.

8.1.2 Chemical Kinetic Model

The detailed USC Mech II [70] is firstly reduced (for shorter computational time) using the Global Pathway Selection (GPS) algorithm [142] and then adopted as the base gas-phase kinetic model. The resulting skeletal kinetic model contains 43 species compared to 111 species in the detailed one with maximum deviation on auto-ignition delay and flame speed predictions of approximately 4.5% and 4.9%, respectively.

This reduced USC Mech II model is then supplemented with a series of O₃ elementary reactions from Ref. [10]. Due to the complexity of the C₂H₄ ozonolysis mechanism, a highly simplified 4-channel global reaction model contains R20a to R20d in Chapter 2.3 is used to describe the complicated ozonolysis chemistry, assuming equal branching ratios of each channel. The corresponding global kinetic parameters of ozonolysis are adopted from Ref. [88] with the pre-exponential factor $A = 5.48 \times 10^9$ and the activation energy $E_a = 21.45$ kJ/mole. The supplemented O₃ reactions together with the 4-channel C₂H₄+O₃ model are summarized in Table 16. Qualitative agreements were reported between numerical and experimental results in previous O₃ assisted combustion studies [12, 16] employing this ozone kinetic model. The overall chemical kinetic model for simulation in this work, i.e., the combination of O₃ reactions in Table 16 and reduced USC Mech II, contains 44 species and 260 reactions in total.

Table 16. Summary of O₃ elementary reactions from Ref. [10] and 4-channel C₂H₄+O₃ model.

Reaction	Pre-exponential factor, A	Temperature dependence, n	Activation energy, E_a (kJ/mole)
C ₂ H ₄ +O ₃ → CH ₂ O+OH+HCO	1.37×10 ⁹	0	21.45
C ₂ H ₄ +O ₃ → CH ₂ O+2H+CO ₂	1.37×10 ⁹	0	21.45
C ₂ H ₄ +O ₃ → CH ₂ O+H ₂ +CO ₂	1.37×10 ⁹	0	21.45
C ₂ H ₄ +O ₃ → CH ₂ O+H ₂ O+CO	1.37×10 ⁹	0	21.45
O ₃ +O ₂ → O ₂ +O+O ₂	1.54×10 ¹⁴	0	96.50
O ₂ +O+O ₂ → O ₃ +O ₂	3.26×10 ¹⁹	-2.1	0
O ₃ +N ₂ → O ₂ +O+N ₂	4.00×10 ¹⁴	0	94.84
O ₂ +O+N ₂ → O ₃ +N ₂	1.60×10 ¹⁴	-0.4	-5.82
O ₃ +O → O ₂ +O+O	2.48×10 ¹⁵	0	95.09
O ₂ +O+O → O ₃ +O	2.28×10 ¹⁵	-0.5	-5.82
O ₃ +O ₃ → O ₂ +O+O ₃	4.40×10 ¹⁴	0	96.50
O ₂ +O+O ₃ → O ₃ +O ₃	1.67×10 ¹⁵	-0.5	-5.82
O ₃ +H → O ₂ +OH	8.43×10 ¹³	0	3.91
O ₃ +H → O+HO ₂	4.52×10 ¹¹	0	0
O ₃ +OH → O ₂ +HO ₂	1.85×10 ¹¹	0	3.48
O ₃ +H ₂ O → O ₂ +H ₂ O ₂	66.2	0	0
O ₃ +HO ₂ → OH+O ₂ +O ₂	6.62×10 ⁹	0	4.16
O ₃ +O → O ₂ +O ₂	4.82×10 ¹²	0	17.14
O ₃ +CH ₃ → CH ₃ O+O ₂	5.83×10 ¹⁰	0	0

*Rate expression $k(T)=A (T/298)^n e^{-E_a/RT}$ in the unit of $\text{cm}^3/\text{mole s}$

8.2 Steady Lifted Flames Without O₃ Addition

8.2.1 The Establishment of Steady C₂H₄ Lifted Flames

Stable C₂H₄ laminar lifted flames are obtained with pure fuel jet and the O₂/N₂ mixture as co-flow. Figure 8.2 shows a series of photographs of stable C₂H₄ lifted flames at different u_f but constant co-flow velocity, $U_{CO} = 0.013$ m/s, and constant oxidizer composition of 12.7% O₂+87.3% N₂. The u_f changes from 2.98 m/s as an attached diffusion flame to finally 5.23 m/s.

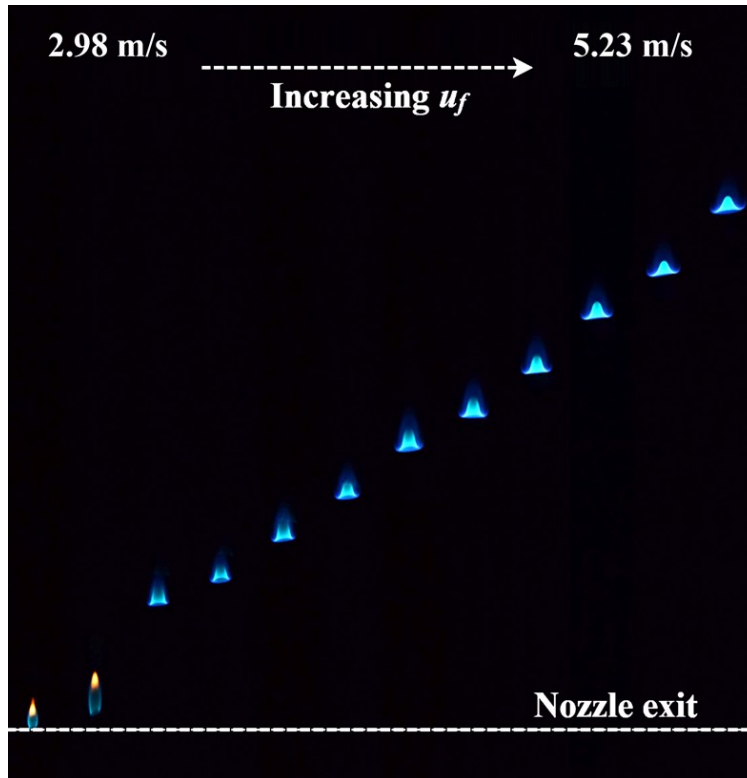


Figure 8.2. Direct photographs of steady lifted flames in series with different C_2H_4 jet velocities start from $u_f = 2.98$ m/s, and 12.7% $O_2 + 87.3\%$ N_2 co-flow with constant velocity of $U_{CO} = 0.013$ m/s.

As the flame detaches from the fuel nozzle, a clear triple flame structure appears with a relatively weak lean premixed wing and strong rich premixed wing, and the trailing diffusion flame in between, intersecting at the so-called “triple point”. If the lifted flame is steady, a dynamic balance between the axial flow velocity just upstream of the flame along the stoichiometric contour, u_{st} , and the propagation speed of the triple flame, S_{tri} , must be satisfied at the corresponding HL as $u_{st} = S_{tri}$. Based on the non-premixed flame theory, the triple point should be located on the stoichiometric contour where the fuel mass fraction $Y_F = Y_{F,st}$ (the stoichiometry mass fraction $Y_{F,st}$ is calculated with C_2H_4 as fuel and O_2/N_2 co-flow mixture as oxidizer). With identical boundary conditions of the experiments as shown in Figure 8.2, non-reacting flow simulations are performed at several u_f , and the

comparison between numerically simulated stoichiometric contours, in terms of axial (x_{st}) and radial position (r_{st}), and the experimentally measured triple point locations is given in Figure 8.3. Qualitatively, reasonable agreement is achieved.

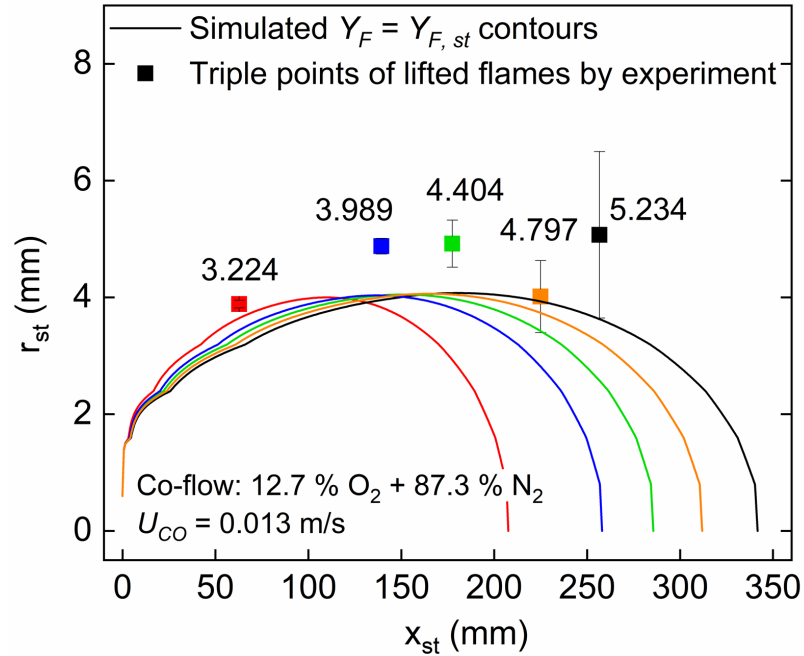


Figure 8.3. Comparison of numerical simulations of stoichiometric contours (solid line) in non-reacting jet and the triple point positions (solid point) of lifted flames measured experimentally. Different u_f distinguished by colors.

8.2.2 Effect of Co-flow Conditions on Flame Lift-off

To investigate the effect of co-flow conditions on non-premixed C_2H_4 flame lift-off, additional experiments are carried out with different O_2 abundances in the co-flow and U_{CO} . Figure 8.4(a) and (b) demonstrate the measured H_L under co-flow conditions of (a) constant $U_{CO} = 0.016$ m/s with different O_2 concentrations and (b) constant 11.5% O_2 +88.5% N_2 with various U_{CO} .

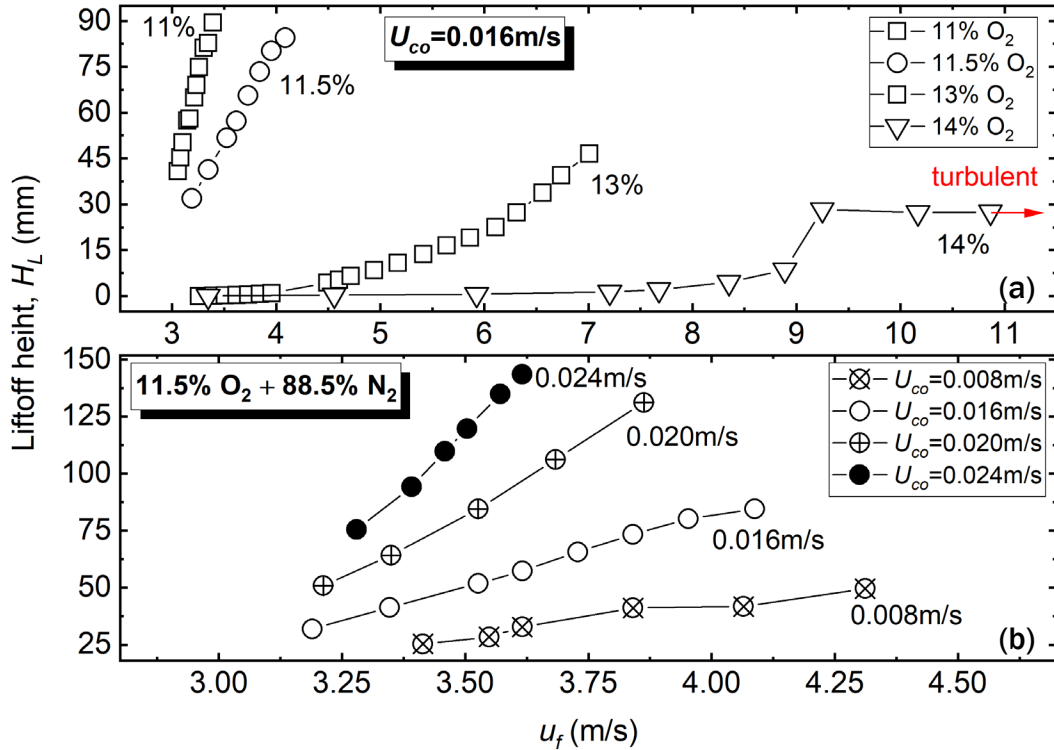


Figure 8.4. Experimentally measured H_L with different co-flow conditions of (a) constant $U_{co} = 0.016$ m/s with different O_2 concentrations and (b) constant 11.5% O_2 with different U_{co} .

A wide range of O_2 concentrations in co-flow are tested, however, not all conditions would allow flame liftoff in laminar regime. It clearly shows in Figure 8.4(a) that with the O_2 concentration being elevated in co-flow, the liftoff from an attached C_2H_4 diffusion flame becomes more difficult. For the case with O_2 concentration of 14% in co-flow, the jet flame does not detach from the nozzle exit until $u_f = 6$ m/s. As the u_f keeps increasing, a sudden jump in H_L appears near $u_f = 9$ m/s, however, the flame could not be lifted up farther with even higher u_f and becomes highly unstable. In our experiments, no flame liftoff can be obtained with O_2 concentration in co-flow higher than 15%. Using the laminar flame speed calculator in CHEMKIN [143], this O_2 effect can be reasonably explained by the 86% reduction in S_L of stoichiometric C_2H_4 and co-flow mixture, with the O_2

concentration in co-flow being decreased from 21% to 11%. In order to establish a steady lifted flame, the dynamic balance of $u_{st} = S_{tri}$ has to be satisfied constantly. Although the subtle change in O₂ concentration in co-flow would not obviously disturb the overall velocity field, it would strongly influence S_L , or equivalently S_{tri} . As plotted in Figure 8.4(a), with the O₂ concentration in co-flow being lowered from 14% to 11%, the flame would be easier to liftoff from the nozzle exit, while the resistant ability of flame to perturbation becomes weaker.

In Figure 8.4(b), the effect of co-flow velocity U_{CO} on H_L is also investigated. It can be perceived that with higher U_{CO} , larger H_L can be achieved with identical co-flow composition and u_f . Furthermore, the increase in slope indicates the flame would be more vulnerable to flow perturbation with higher U_{CO} .

8.3 Effect of O₃ Addition on C₂H₄ Lifted Flame

8.3.1 Flame Liftoff Height, H_L

To study the effect of O₃ addition on lifted flame dynamics, a steady lifted C₂H₄ flame is first established at O₃ free condition, and then the generator is switched on to convert part of the O₂ into O₃ in co-flow. All lifted flame experiments presented in this Chapter 8.3 are undertaken with co-flow composition of 11.5% O₂+88.5% N₂ and $U_{CO} = 0.016$ m/s. Figure 8.5(a) shows the liftoff heights of flames with different amounts of O₃ in the co-flow. It is interesting that with same O₃ addition in the co-flow, opposite trends on the change of H_L can be observed. The lifted flame descends (H_L decreases) with O₃ addition if u_f is small or, equivalently, the initial liftoff height (H_{L,0}) is low, while it ascends instead if the value of u_f is relatively large. At the high H_{L,0} condition, e.g., with $u_f = 3.68$

m/s, the addition of O_3 in excess of 150 ppmv in the oxidizer co-flow could directly result in flame blow-out. However, in similar experiments using C_3H_8 as fuel [8], H_L consistently decreased with O_3 addition, regardless of the u_f .

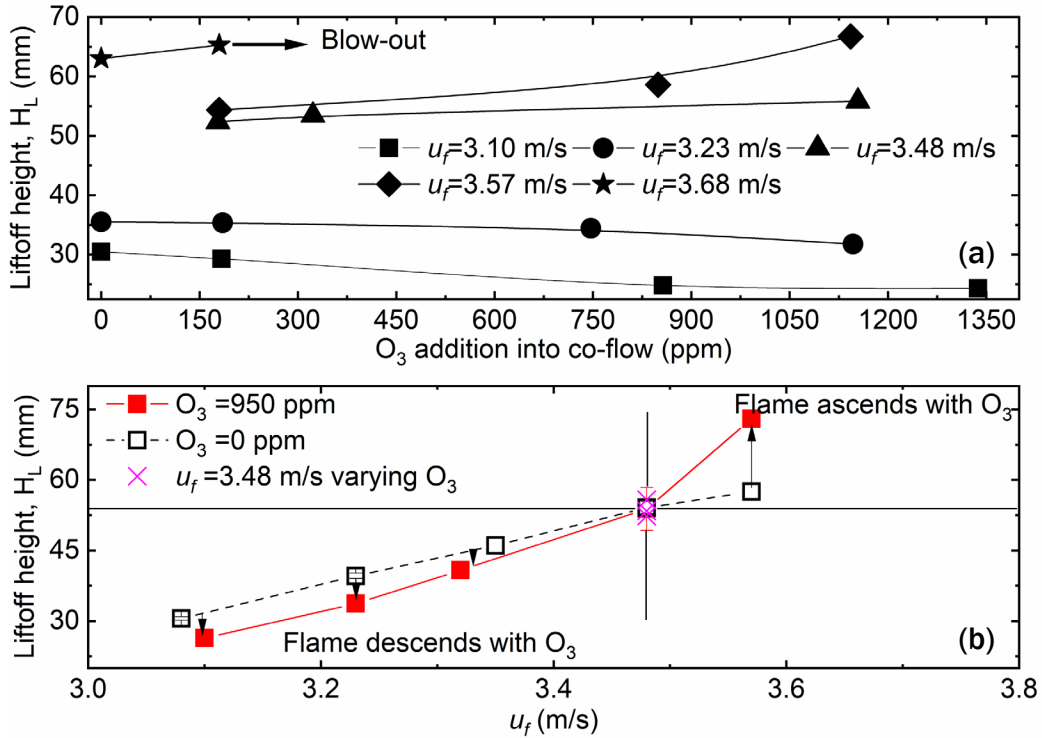


Figure 8.5. The change in measured H_L with (a) increasing O_3 addition in co-flow at different u_f and (b) ranging u_f of constant O_3 in co-flow. The co-flow composition 11.5% O_2 +88.5% N_2 with constant velocity of $U_{CO} = 0.016$ m/s.

Further experiments are conducted with different u_f but constant O_3 concentration in the co-flow, and the measured lift-off heights are shown in Figure 8.5(b). Noticeable change in H_L can be seen at both relatively low and high $H_{L,0}$ while the effect of O_3 addition on H_L diminishes at $H_{L,0}$ in between. Accordingly, it could be concluded that the effect of O_3 addition on the lifted C_2H_4 flame is a function of $H_{L,0}$ (or equivalently u_f). As the flame gradually lifts from the fuel nozzle, O_3 addition in the co-flow would firstly decrease and then increase the H_L , while seemingly there is a region in between where the flame is not

sensitive to the effect from O_3 . Based on this observed “two-way” (non-monotonic) C_2H_4 lifted flame behavior with O_3 addition, a pair of competing pathways must exist controlling the flame dynamics.

8.3.2 CH_2O PLIF Measurement

As one of the major products, CH_2O , could be considered as an indicator to demonstrate the existence and spatial distribution of the C_2H_4 ozonolysis reaction, especially in the low-temperature regime. A CH_2O PLIF measurement is then conducted for lifted flames with and without O_3 addition.

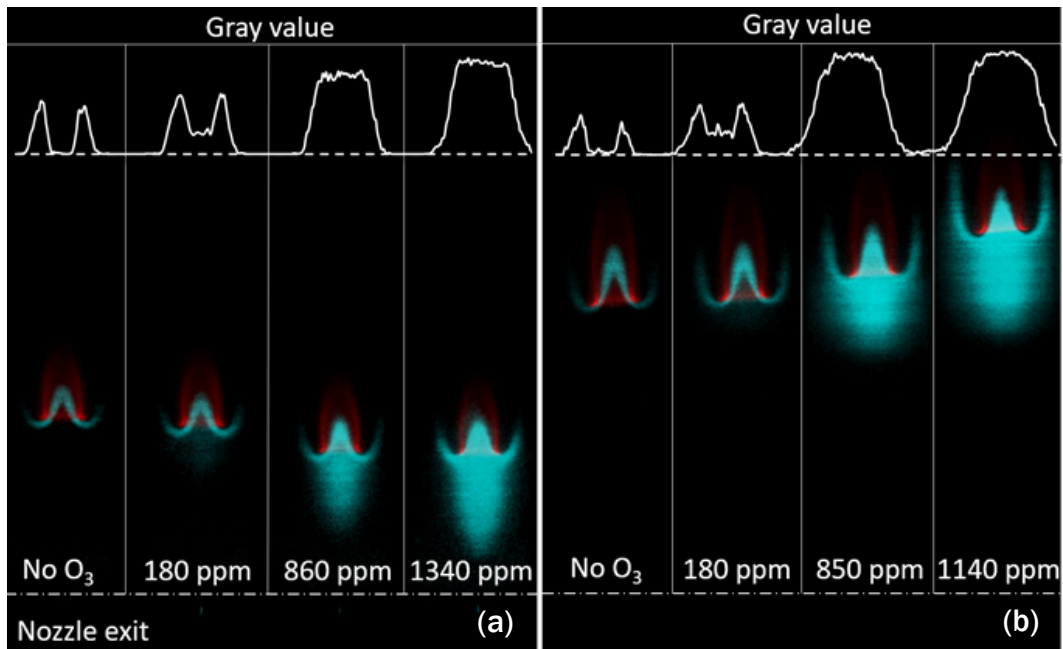


Figure 8.6. CH_2O PLIF (blue) and broadband chemiluminescence (red) of lifted flames with different O_3 concentrations at (a) $u_f = 3.10$ m/s and (b) $u_f = 3.57$ m/s.

Figure 8.6 shows overlaid images of CH_2O PLIF (blue) and broadband chemiluminescence (red) collected by the same ICCD camera at (a) $u_f = 3.10$ m/s and (b) $u_f = 3.57$ m/s, corresponding to cases of $\Delta H_L < 0$ and $\Delta H_L > 0$, respectively. The gray value

of CH₂O PLIF is sampled at the horizontal level of the triple points of each lifted flame, as illustrated in Figure 8.6 as well. For both cases with no O₃ addition, CH₂O is only detected at the premixed wings of the triple flames. Once O₃ is added to the co-flow, CH₂O starts to appear upstream. As the added O₃ concentration continues to increase, more intense fluorescence signals from CH₂O are captured.

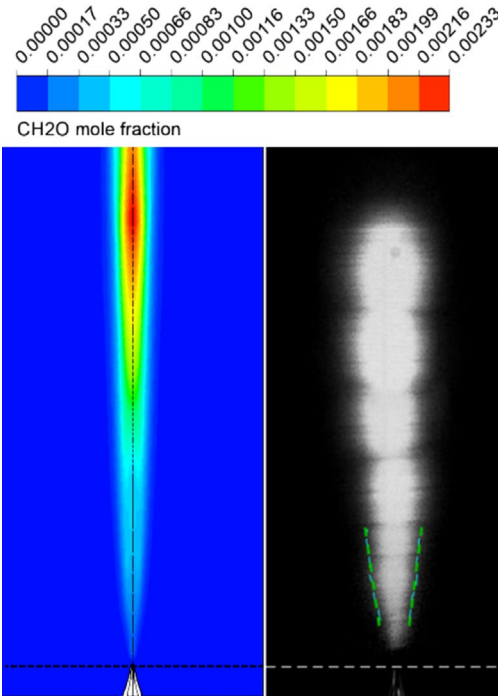


Figure 8.7. Comparison between the CH₂O distributions at $u_f = 3.24$ m/s and 1300 ppmv O₃ addition in the co-flow. Left: simulated reacting co-flow jet (no flame) using Fluent. Right: the CH₂O PLIF by experiments.

By moving the laser sheet upstream, it is found that CH₂O forms immediately, near the nozzle exit where C₂H₄ and O₃ start to mix in the shear layer. Figure 8.7 illustrates the comparison between the CH₂O spatial distributions from reacting jet simulation and the CH₂O PLIF at $u_f = 3.24$ m/s and 1300 ppmv O₃ addition in the co-flow. The plume angle indicated by the two green dashed lines in experimental PLIF result is measured as 18.10 degrees while 13 degrees is given by the simulation. Although no quantitative data can be

provided by the PLIF due to ICCD camera saturation, a similar distribution is noticed from the numerical result and the PLIF image that CH₂O spreads out from the nozzle exit and the maximum value appears along the centerline.

In general, the CH₂O PLIF measurements indicate that the ozonolysis reaction proceeds far upstream of the flame, regardless of the value of initial liftoff height. However, the reason of the observed two-way change in H_L after O₃ addition is still unclear. To further understand the kinetic/dynamic process resulting in the change of H_L, numerical simulations are performed regarding the fundamental flame stabilization mechanism.

8.4 Numerical Simulation and Analysis

8.4.1 Effect of O₃ Addition on *S_{tri}*

The effect of O₃ addition on *S_L*, and therefore on *S_{tri}*, is evaluated by using CHEMKIN [143]. A 1-D Plug Flow Reactor (PFR) module is connected in tandem with Premixed Laminar Flame Speed Calculator to mimic the effect of C₂H₄ ozonolysis reaction upstream. The residence time in the PFR is set to be $\tau_{\text{PFR}} = 20\sim 80$ ms, which is approximately the same as the value estimated from the nozzle exit to the upstream boundary of the lifted flame as $\tau \sim H_L/u_f$. The energy equation is solved in the PFR module with an adiabatic boundary and inlet conditions of T = 298 K and P = 760 torr. The fuel is pure C₂H₄, and oxidizer is an O₂/O₃/N₂ mixture with global stoichiometry of unity. Calculations are performed at different τ_{PFR} so that the cases with both low and high H_{L,0} can be compared. *S_L* is also calculated with O₃ addition while the ozonolysis reaction of C₂H₄ is excluded but other O₃ related elementary reactions remain the same. Results are presented in Figure 8.8.

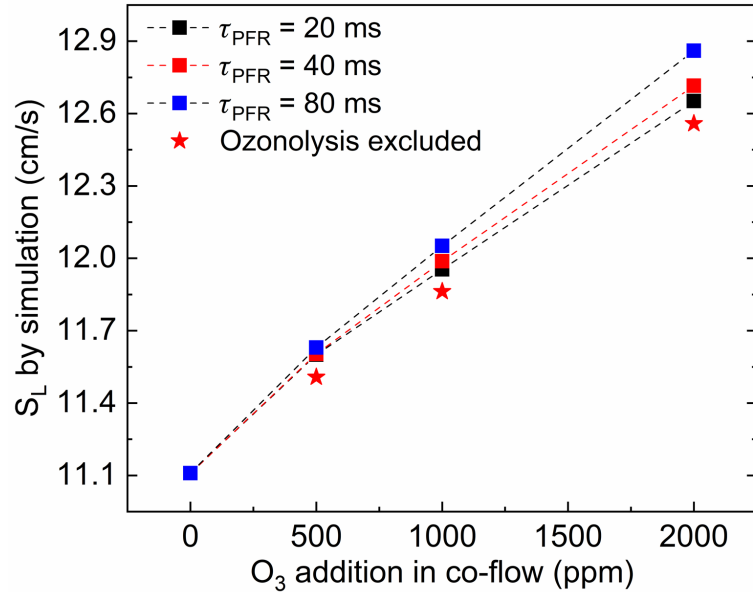


Figure 8.8. Calculated S_L with different amounts of O_3 addition using PFR + Laminar Flame Speed model in CHEMKIN. Different residence times: 20 ms (black squares), 40 ms (red squares) and 80 ms (blue squares) are set in the PFR to simulate lifted flames with different H_L .

It is clearly demonstrated that considerable enhancement in S_L is achieved with O_3 addition no matter the residence time in the PFR. Approximately 0.84% of the additional increment on S_L is obtained if the C_2H_4 ozonolysis reaction is included compared to the case without at 2000 ppmv O_3 addition and $\tau_{PFR} = 20$ ms. Under such conditions, the change in fluid physical properties, e.g., specific heat capacity of gas mixture, is nearly negligible ($\sim 0.1\%$) and the corresponding enhancement in S_L should be dominantly from the chemical kinetic effect. Generally, the overall increase in S_L owing to O_3 addition in the co-flow should be expected at both low and high $H_{L,0}$, which would accordingly increase the S_{lri} and decrease H_L regardless of its initial value. However, besides the triple flame propagation, the change in chemical composition—initiated by the ozonolysis reaction upstream of the flame stabilization point—should also be considered.

8.4.2 Effect of Fluid Composition on u_{st}

In former study, Xue et al. [144] investigated liftoff characteristic of a dimethyl ether (DME) flame and no stable lifted DME jet flame could be obtained. The observation was rationalized by the much larger $Y_{F,st}$ of DME comparing to hydrocarbon fuels due to the oxygenation (fuel bound O atom), which consequently renders a much higher u_{st} for DME according to the linear relation between $Y_{F,st}$ and u_{st} , predicted by the Landau-Squire similarity solution [145, 146]. This implies that both u_{st} and $Y_{F,st}$ can be significantly affected, owing to the change in chemical composition induced by the ozonolysis reaction upstream of the flame. Ozonolysis yields large amounts of CH₂O that blend with C₂H₄ locally, and thus the fuel jet transitions to a C₂H₄/CH₂O mixture gradually. A rough calculation indicates that a transition from pure C₂H₄ to 10%/90% of CH₂O/C₂H₄ could lead to a 7.6% increase in $Y_{F,st}$ and consequently increase the u_{st} . In fact, as previously stated in Chapter 6 and 7, many other oxygenated compounds in addition to CH₂O have been experimentally characterized in O₃ initiated C₂H₄ oxidation at ambient condition, which may further increase the u_{st} upstream of the flame.

Consequently, both S_{tri} and u_{st} will be enhanced by O₃ addition in the co-flow, though their corresponding principles are different. Based on the stabilization mechanism of laminar lifted flame through velocity balance, the increase in S_{tri} and u_{st} would result in either a decrease or an increase of the H_L: At the low H_{L,0} condition, the effect from S_{tri} dominates that from u_{st} and the H_L decreases; at the high H_{L,0} condition, the higher yield of CH₂O (owing to longer residence time) upstream of the flame could further increase u_{st} , consequently increasing the H_L instead.

8.4.3 2-D Reacting Flow Simulations using ANSYS Fluent

To support the proposed kinetic/dynamic interaction hypothesis, qualitative reacting flow simulations are performed using Fluent with the steady lifted flames first established at arbitrary liftoff heights; then, 2000 ppmv O₃ is added in the oxidizer co-flow.

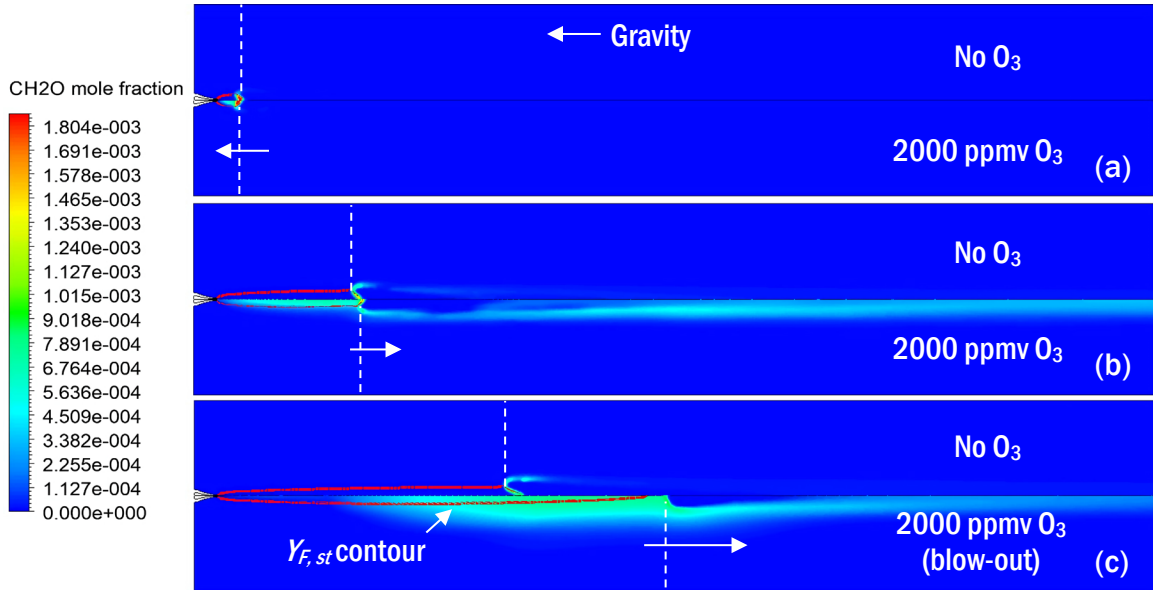


Figure 8.9. Simulated CH₂O distributions of C₂H₄ lifted flames before and after O₃ addition. (a) H_L decrease (b) H_L increase and (c) blow-out. The stoichiometric contour $Y_F = Y_{F, st}$ is marked with the red line.

It should be noted that in the current qualitative simulations, the high O₃ concentration is employed for demonstration purposes (i.e., to produce a clearer result). It is believed that this higher concentration of O₃ does not alter the underlying physical mechanisms. All three cases are reproduced numerically: 1) H_L decrease (Figure 8.9(a)), H_L increase (Figure 8.9(b)), and flame blow-out (Figure 8.9(c)). In all three cases with added O₃, there is clear CH₂O formation upstream of the flame. It appears that if the lifted flame is steady, then the corresponding triple point remains on the stoichiometric contour, as predicted by theory. Additionally, if the ozonolysis reaction is removed from the kinetic

model, the lifted flame would consistently move to upstream after O_3 addition because of the increased S_L , regardless of the value of $H_{L,0}$; this result coincides with the experiment using saturated fuel [8]. The red lines in Figure 8.9 visualize the stoichiometric contours where $Y_F = Y_{F, st}$. By sampling along the simulated stoichiometric contours, CH_2O mole fraction and the local axial jet velocity u_{st} are plotted in Figure 8.10(a) and (b), respectively.

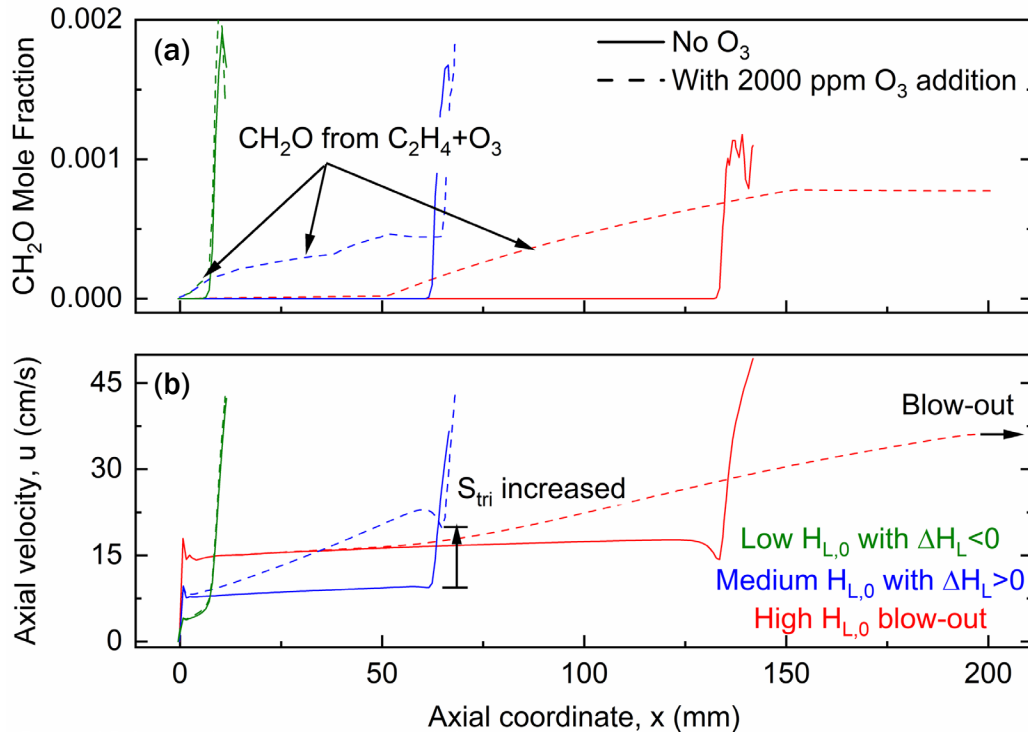


Figure 8.10. Numerical results along the $Y_F = Y_{F,st}$ contour of C_2H_4 lifted flames with (dashed lines) and without (solid lines) O_3 addition. (a) Mole fraction of CH_2O and (b) u_{st} .

When $H_{L,0}$ is low, once O_3 is added, the increase of S_{tri} dominates the effect of the change (increase) in u_{st} , so the initially stable lifted flame propagates upstream until a new dynamic balance is established along the stoichiometric contour, and the green dashed line in Figure 8.10(b) indicates that a slightly higher S_{tri} is obtained compared to the initial value. When $H_{L,0}$ is in medium range, once O_3 is added in the co-flow, the higher value of

u_{st} at $H_{L,0}$ pushes the lifted flame downstream to a steady position where both u_{st} and S_{tri} are enhanced as shown by the blue dashed line in Figure 8.10(b). When $H_{L,0}$ is very high, the simulation shows that the O_3 addition rendering a continuous increase of CH_2O as well as u_{st} along the stoichiometric contour. However, the corresponding increase of u_{st} is much faster than of S_{tri} , so that no dynamic balance between them can be regained along the stoichiometric contour as flame is moving downstream and eventually blow-out occurs. In summary, these numerical results qualitatively demonstrate the competing effects induced by the ozonolysis reaction that result in either an increase or a decrease in H_L .

Besides the enhancements in both S_{tri} and u_{st} from the chemical kinetic effect, with the intrinsically high exothermicity, it is believed that the heat release from ozonolysis of C_2H_4 upstream of the flame could also contribute to both velocities, and therefore affecting the dynamic balance. From the reacting flow simulations, the temperature fields for both $\Delta H_L < 0$ and $\Delta H_L > 0$ cases are given in Figure 8.11(a) and (b) respectively, with and without O_3 addition in co-flow.

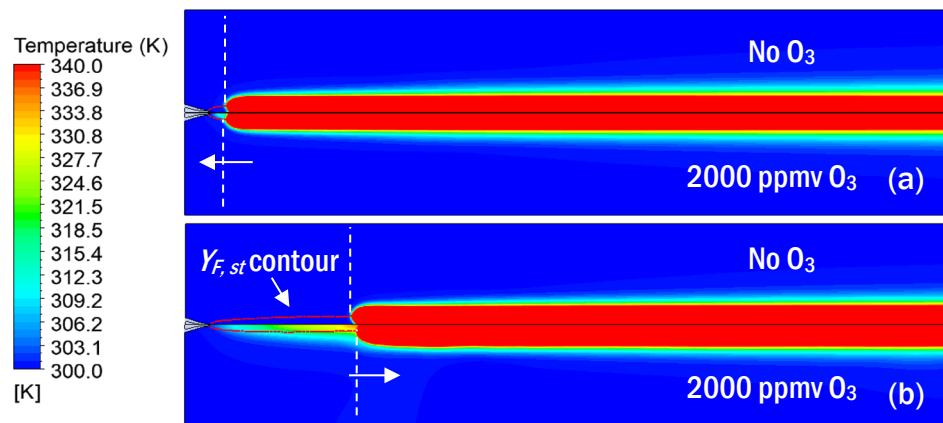


Figure 8.11. Simulated temperature fields of C_2H_4 lifted flames before and after O_3 addition. (a) H_L decrease and (b) H_L increase. The stoichiometric contour $Y_F = Y_{F,st}$ is marked with the red line.

Even though the residence time is quite limited from the fuel nozzle exit to the bottom of lifted flame, apparent temperature increase is predicted in the co-flow jet for both cases. By sampling along the stoichiometric contour of $Y_F = Y_{F,st}$, the temperature of both $\Delta H_L < 0$ and $\Delta H_L > 0$ cases are obtained and plot in Figure 8.12(a).

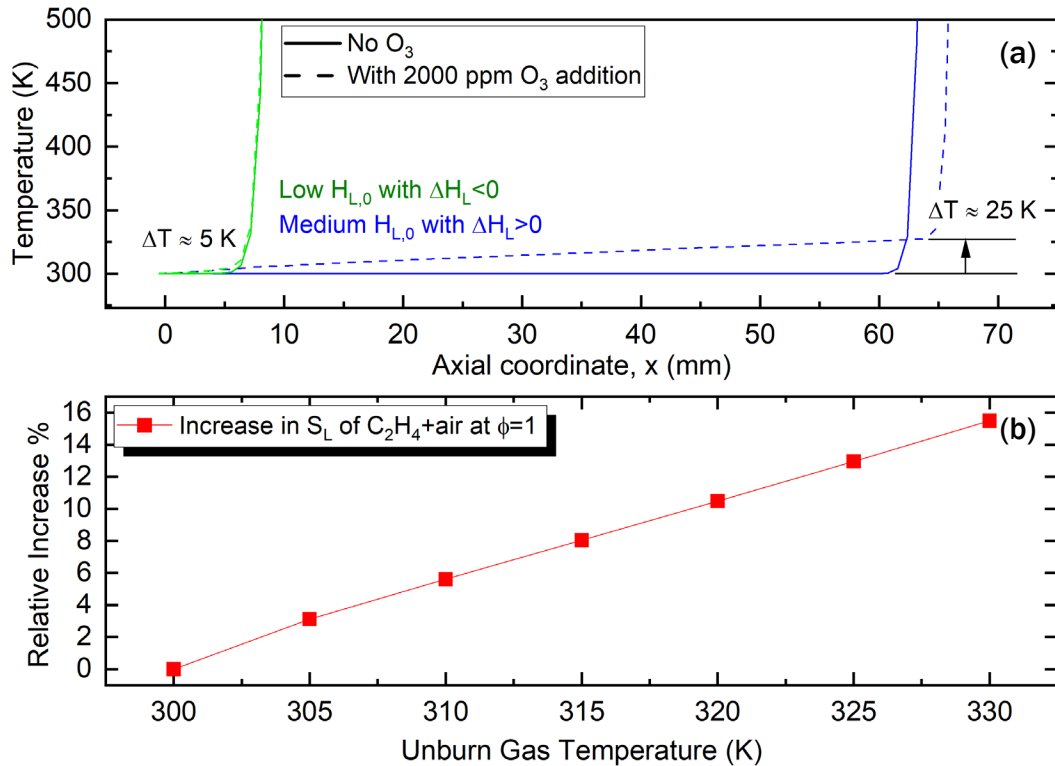


Figure 8.12. The numerical results of (a) temperature along $Y_F = Y_{F,st}$ contour of C₂H₄ lifted flames with (dashed lines) and without (solid lines) O₃ addition, and (b) relative enhancement in S_L of C₂H₄ in air with increasing unburned gas temperature from 300 K to 330 K.

For the case of low $H_{L,0}$, around 5 K increase in temperature is simulated upstream of the flame with O₃ addition, while a larger temperature increase around 25 K is observed for the case with high $H_{L,0}$ after O₃ is added. Similar to the effect from added ozonolysis products as proposed previously, the increased temperature upstream of the lifted flame would enhance both S_{tri} and u_{st} simultaneously. As shown in Figure 8.10(b), for the two

cases with steady lifted flames after O_3 addition, the relative increase in S_{tri} is estimated around 8% and 111% for $\Delta H_L < 0$ and $\Delta H_L > 0$, respectively. By simply calculating the laminar flame speed of C_2H_4 in air at unity stoichiometry, with rising unburned gas temperature from $T_{in} = 300$ K to 330 K, the relative enhancements (compared to $T_{in} = 300$ K) in S_L are presented in Figure 8.12(b). It is interesting to note that at $T_{in} = 325$ K ($\Delta T = 25$ K) around 13% enhancement in S_L is predicted, which is much lower than the 111% increase in S_{tri} for the $\Delta H_L > 0$ case with high $H_{L,0}$. On the other hand, for the $\Delta H_L < 0$ case with low $H_{L,0}$, the 8% increase in S_{tri} reasonably coincides with the 4% enhancement in S_L at $T_{in} = 305$ K ($\Delta T = 5$ K). Therefore, it can be qualitatively concluded that with the $H_{L,0}$ being increased, the effect of temperature on the velocity balance, i.e., $S_{tri} = u_{st}$, would be lowered. As the degree of ozonolysis reaction increases, with more species being generated in the co-flow jet, a larger effect from the ozonolysis products on the velocity balance should be expected.

CHAPTER 9. CONCLUSIONS AND FUTURE RECOMMENDATIONS

9.1 Kinetic Study on O₃ Initiated C₂H₄ Oxidation at Room Temperature

With the newly designed fast-mixing flow reactor system, the chemistry of O₃ initiated C₂H₄ oxidation is experimentally investigated at room temperature. The global reaction rate constant of C₂H₄+O₃ is measured. By applying the UV LED absorption at 255 nm, the decay of O₃ along the flow reactor is recorded at $[C_2H_4]_0 \gg [O_3]_0$. The calculated reaction rate constant under pseudo 1st order approximation, $k = (8.1460 \pm 0.1797) \times 10^5$ cm³/mole s, agrees well to the previous results in literatures. With the combination of tunable photoionization mass spectrometry, and high-level calculations on molecular structure and adiabatic ionization energy, unambiguous species characterization is succeeded. Over 50 products and intermediates have been rigorously identified in the room-temperature oxidation of C₂H₄, which can be categorized by their functional groups into alcohol, aldehyde, and peroxide. It is strongly believed that the secondary reactions following the ozonolysis play vital roles in the production of most detected species.

Multiple organic peroxy radicals are directly probed and characterized. Referring to the classic low-temperature fuel oxidation mechanism, it is proposed that the formation of observed CH₃O \dot{O} is initiated from C₂H₄+ \dot{O} , and C₂H₅O \dot{O} is from C₂H₄+ \dot{H} , respectively, while both CH₂=CHO \dot{O} and HOCH₂CH₂O \dot{O} are from C₂H₄+ $\dot{O}H$. By comparison of relative intensities of corresponding hydroperoxides in mass spectrums, with and without n-C₄H₁₀ as scavenger, the existence and proposed formation channels of those peroxy

radicals are supported qualitatively. With high yields radical production from ozonolysis of C₂H₄, especially the $\dot{\text{O}}\text{H}$ radical, reaction $\text{RH} + \dot{\text{O}}\text{H} \rightarrow \dot{\text{R}} + \text{H}_2\text{O}$ is initiated at room temperature, at which the continuously formed peroxy radicals would have lifespan long enough to be accumulated and consequently detected. Moreover, based on determined molecular structures, direct addition of sCI, i.e., CH₂OO, into other radicals is proposed as another possible RO $\dot{\text{O}}$ formation mechanism.

In summary, the species characterization further expands our knowledge on the chemical pool of this room-temperature oxidation initiated by the ozonolysis reaction, and therefore provides great insight into future model development and improvement for practical O₃ assisted combustion.

9.2 Effect of O₃ Addition on C₂H₄ Laminar Flame Dynamics

The effect of O₃ addition on non-premixed C₂H₄ lifted jet flames is investigated, using experiments, including PLIF of CH₂O, and numerical simulations. Stable, laminar lifted C₂H₄ flames are established in a co-flow geometry and a wide range of liftoff height is obtained. Numerical simulations and experimental results are in qualitative agreement. With O₃ addition in the co-flow, the change of flame liftoff height shows sensitivity on its initial value. If the initial flame liftoff height is low, the flame descends in height after O₃ addition. In contrast, with high initial flame liftoff height, the flame ascends after O₃ addition and blow-out occurs if O₃ concentration in the co-flow is too high. PLIF measurements show significant formation of CH₂O starting from the fuel nozzle exit, owing to the prompt ozonolysis reaction between C₂H₄ and O₃. Such ozonolysis reaction upstream of the flame increases both the propagation speed of the triple flame and the axial

jet velocity along the stoichiometric contour, therefore creating competing process for establishing the flame liftoff height. The flame propagates to an upstream position, owing to the increase of triple flame speed while the increase in jet velocity pushes the flame downstream instead. The initial flame liftoff height determines the residence time for the ozonolysis reaction, therefore affecting the magnitude of change of the triple flame speed and jet velocity along the stoichiometric contour; thus, the initial liftoff height determines which process dominates and the final location of the flame after O_3 addition.

9.3 Future Recommendations

The foremost recommendation to future work is the continuing development of more accurate kinetic model to the O_3 initiated C_2H_4 oxidation, especially in the low-temperature region. The current kinetic model over-simplifies the ozonolysis reaction by four parallel channels as R20a to R20d, where the sCI proved with production yield near 50% is excluded. This simplification might be acceptable at elevated temperatures, however, at low temperatures, the abundantly produced sCI has lifespan long enough to undergo many bimolecular reactions, which has been experimentally demonstrated in Chapter 6 and 7 of this dissertation. Recently, thanks to the contribution by Welz et al. [53], many kinetic studies of sCI bimolecular reactions were carried out, and the corresponding reaction rate parameters were measured. These results could be of great help in the future. Compared with USC Mech II [70], the HP Mech [67, 68] shows relatively higher accuracy in products prediction in low temperatures, and therefore is suggested to be the base mechanism for future model development. By quantitatively measuring the temporal profile of products and intermediates in the flow reactor at certain temperatures, the developed kinetic model could be validated and improved.

Inspired by the characterization of multiple peroxy radicals in Chapter 7, the second recommendation to future work is the theoretical study on possible reaction pathway between sCI and other radicals. Although many studies were reported on bimolecular reactions between sCI and compounds in the atmosphere, such as H₂O, NO_x, SO₂, and alcohols, sparse investigation was conducted on the reaction path between sCI and radicals in theory. Much more organic peroxy radicals can be directly produced through sCI if this mechanism is kinetically feasible, which could potentially influence the chemistry of O₃ assisted low-temperature oxidation and combustion. Up to now, the possible kinetic role of sCI in combustion is still unclear.

The third recommendation to future work is to investigate the effect of O₃ initiated low-temperature oxidation on dynamics of turbulent flames, which is more common in practical applications. A much stronger entanglement between O₃ chemistry and the flow field can be expected. On the other hand, while the presented lifted flame experiment in this dissertation is carried out at room temperature and atmospheric pressure, other experimental conditions can be adopted. For example, in sub-atmospheric pressures, the mixing between fuel jet and oxidizer co-flow could be significantly enhanced, meanwhile, the product yield of ozonolysis reaction is altered. The combined effect might result in different phenomenon.

APPENDIX A. DIMENSIONAL DRAWINGS OF COMPONENTS IN THE FAST-MIXING FLOW REACTOR SYSTEM

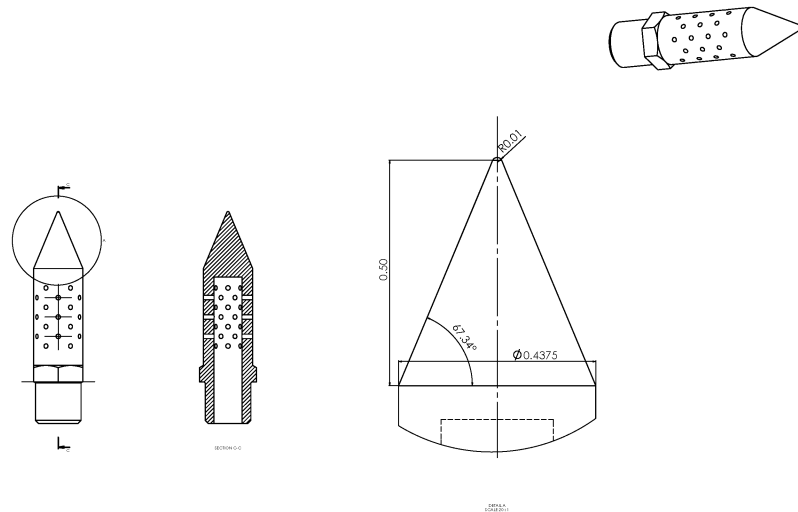


Figure A.1. The nosecone welded to the muffler fuel injector (unit in inch).

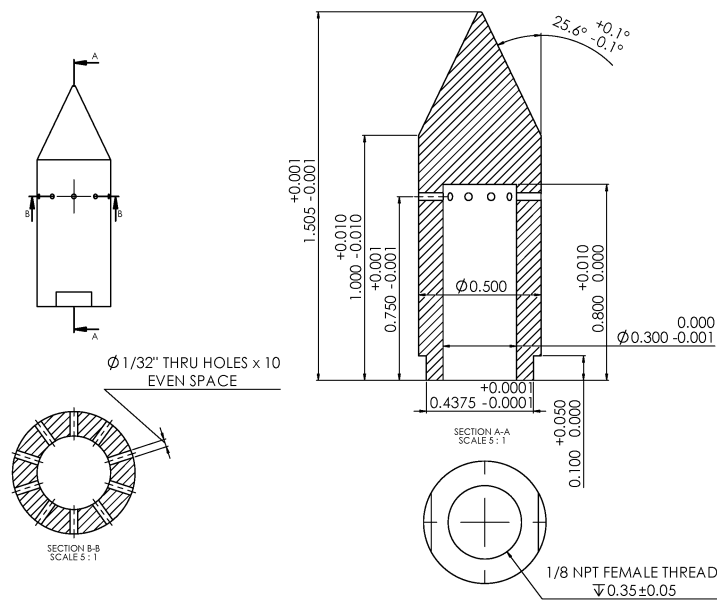


Figure A.2. Alternative fuel injector design of single row fuel outlets (unit in inch).

25mm OD STRAIGHT REACTOR 13.18 DIVERGENCE ANGLE

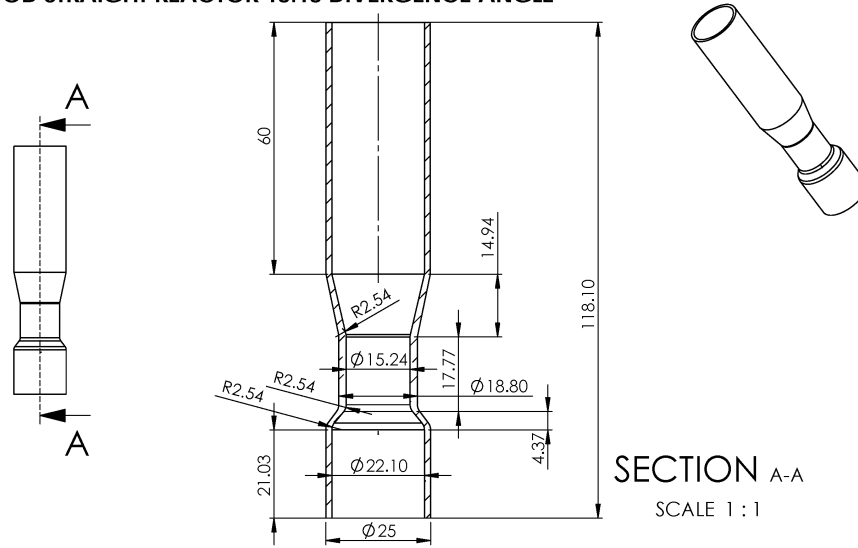


Figure A.3. Quartz flow reactor with C-D section design (unit in mm).

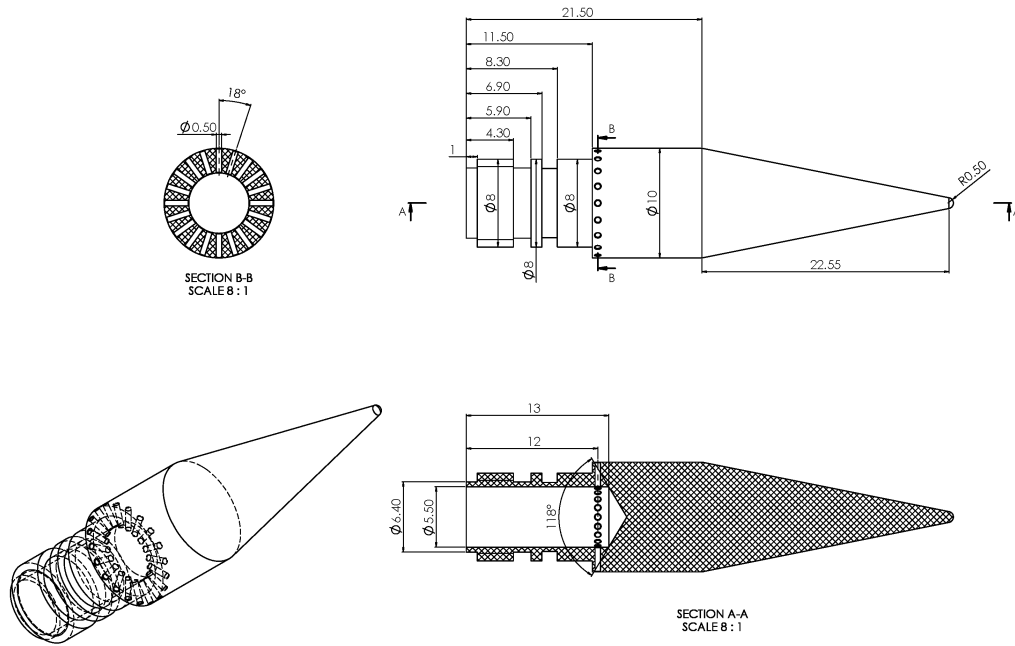


Figure A.4. The design of 20-outlets fuel injector, head part (unit in mm).

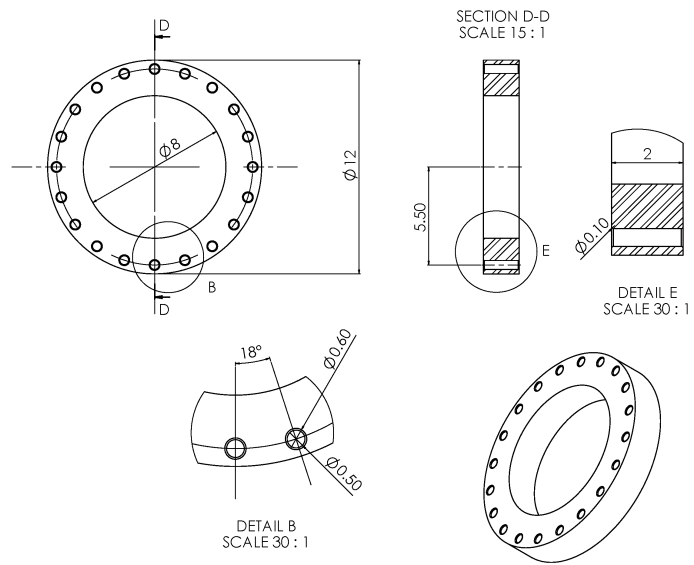


Figure A.5. The design of 20-outlets fuel injector, support ring (unit in mm).

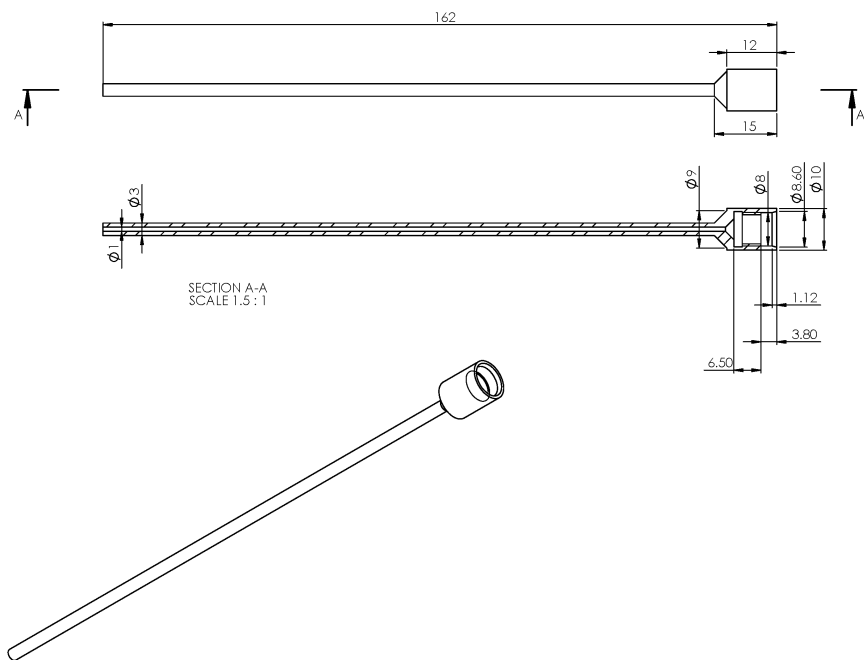


Figure A.6. The design of 20-outlets fuel injector, fuel inlet (unit in mm).

REFERENCES

- [1] D.M. Van Wie, S.M. D'Alessio, M.E. White, Hypersonic airbreathing propulsion, Johns Hopkins APL technical digest 26 (2005) 430-437.
- [2] W. Sun, X. Gao, B. Wu, T. Ombrello, The effect of ozone addition on combustion: Kinetics and dynamics, *Progress in Energy and Combustion Science* 73 (2019) 1-25.
- [3] H. Nishida, T. Tachibana, Homogeneous charge compression ignition of natural gas/air mixture with ozone addition, *Journal of propulsion and power* 22 (2006) 151-157.
- [4] A. Mohammadi, H. Kawanabe, T. Ishiyama, M. Shioji, A. Komada, Study on combustion control in natural-gas PCCI engines with ozone addition into intake gas, Report No. 0148-7191, SAE Technical Paper, 2006.
- [5] F. Foucher, P. Higelin, C. Mounaïm-Rousselle, P. Dagaut, Influence of ozone on the combustion of n-heptane in a HCCI engine, *Proceedings of the Combustion Institute* 34 (2013) 3005-3012.
- [6] I. Ekoto, F. Foucher, Mechanisms of enhanced reactivity with ozone addition for advanced compression ignition, *SAE International Journal of Fuels and Lubricants* 11 (2018) 443-457.
- [7] S. Biswas, I. Ekoto, Detailed Investigation into the Effect of Ozone Addition on Spark Assisted Compression Ignition Engine Performance and Emissions Characteristics, SAE International, 2019.
- [8] T. Ombrello, S.H. Won, Y. Ju, S. Williams, Flame propagation enhancement by plasma excitation of oxygen. Part I: Effects of O₃, *Combustion and flame* 157 (2010) 1906-1915.
- [9] F. Halter, P. Higelin, P. Dagaut, Experimental and detailed kinetic modeling study of the effect of ozone on the combustion of methane, *Energy & Fuels* 25 (2011) 2909-2916.
- [10] Z.H. Wang, L. Yang, B. Li, Z.S. Li, Z.W. Sun, M. Aldén, K.F. Cen, A.A. Konnov, Investigation of combustion enhancement by ozone additive in CH₄/air flames using direct laminar burning velocity measurements and kinetic simulations, *Combustion and Flame* 159 (2012) 120-129.
- [11] X. Liang, Z. Wang, W. Weng, Z. Zhou, Z. Huang, J. Zhou, K. Cen, Study of ozone-enhanced combustion in H₂/CO/N₂/air premixed flames by laminar burning velocity measurements and kinetic modeling, *International Journal of Hydrogen Energy* 38 (2013) 1177-1188.
- [12] X. Gao, Y. Zhang, S. Adusumilli, J. Seitzman, W. Sun, T. Ombrello, C. Carter, The effect of ozone addition on laminar flame speed, *Combustion and Flame* 162 (2015) 3914-3924.

- [13] T.M. Vu, S.H. Won, T. Ombrello, M.S. Cha, Stability enhancement of ozone-assisted laminar premixed Bunsen flames in nitrogen co-flow, *Combustion and Flame* 161 (2014) 917–926.
- [14] A. Ehn, J. Zhu, P. Petersson, Z. Li, M. Aldén, C. Fureby, T. Hurtig, N. Zettervall, A. Larsson, J. Larfeldt, Plasma assisted combustion: Effects of O₃ on large scale turbulent combustion studied with laser diagnostics and Large Eddy Simulations, *Proceedings of the Combustion Institute* 35 (2015) 3487-3495.
- [15] Y. Zhang, M. Zhu, Z. Zhang, R. Shang, D. Zhang, Ozone effect on the flammability limit and near-limit combustion of syngas/air flames with N₂, CO₂, and H₂O dilutions, *Fuel* 186 (2016) 414-421.
- [16] X. Gao, B. Wu, W. Sun, T. Ombrello, C. Carter, Ozonolysis activated autoignition in non-premixed coflow, *Journal of Physics D: Applied Physics* 52 (2019) 105201.
- [17] X. Gao, W. Sun, T. Ombrello, C. Carter, The Effect of Ozonolysis Activated Autoignition on Jet Flame Dynamics, 55th AIAA Aerospace Sciences Meeting, (2017) AIAA 2017-1776.
- [18] Y. Ju, W. Sun, Plasma assisted combustion: Dynamics and chemistry, *Progress in Energy and Combustion Science* 48 (2015) 21-83.
- [19] M.E. Gluckstein, Combustion with ozone-modification of flame speeds C₂ hydrocarbon-air mixtures, *Umr*, (1955).
- [20] M. Pinchak, T. Ombrello, C. Carter, E. Gutmark, V. Katta, The Effect of Hydrodynamic Stretch on the Flame Propagation Enhancement of Ethylene by Addition of Ozone, *Philosophical Transactions of the Royal Society A* 373 (2015) 20140339.
- [21] X. Gao, B. Wu, W. Sun, T. Ombrello, C. Carter, The effects of ozonolysis activated autoignition on non-premixed jet flames, 55th AIAA Aerospace Sciences Meeting, Gaylord Palms, Kissimmee, Florida, 2018.
- [22] X. Gao, S. Yang, B. Wu, W. Sun. The effects of ozonolysis activated autoignition on non-premixed jet flame dynamics: a numerical and experimental study. In: editor^editors. 53rd AIAA/SAE/ASEE Joint Propulsion Conference; 2017. p. 4774.
- [23] X. Gao, The effects of ozone addition on flame propagation and stabilization, Georgia Institute of Technology, 2017.
- [24] X. Gao, J. Zhai, W. Sun, T. Ombrello, C. Carter. The Effect of Ozone Addition on Autoignition and Flame Stabilization. In: editor^editors. 54th AIAA Aerospace Sciences Meeting; 2016. p. 0960.
- [25] C. Schönbein, Ueber die langsame Verbrennung des Aethers, *Ber. Verh. Nat. Ges. Basel* 7 (1847) 4-6.

- [26] C. Schönbein, Ueber die Erzeugnisse der langsamen Verbrennung des Aethers, *J. Prakt. Chem* 105 (1868) 232-239.
- [27] R. Criegee, G. Wenner, Die ozonisierung des 9, 10 - oktalins, *Justus Liebigs Annalen der Chemie* 564 (1949) 9-15.
- [28] R. Huisgen, Kinetics and mechanism of 1, 3 - dipolar cycloadditions, *Angewandte Chemie International Edition in English* 2 (1963) 633-645.
- [29] C. Gillies, J. Gillies, R. Suenram, F.J. Lovas, E. Kraka, D. Cremer, Van der Waals complexes in 1, 3-dipolar cycloaddition reactions: Ozone-ethylene, *Journal of the American Chemical Society* 113 (1991) 2412-2421.
- [30] L. Nord, Ozone complexes in solid nitrogen, *Journal of Molecular Structure* 96 (1983) 37-44.
- [31] J. Gillies, C.W. Gillies, R. Suenram, F. Lovas, W. Stahl, The microwave spectrum and molecular structure of the ethylene-ozone van der Waals complex, *Journal of the American Chemical Society* 111 (1989) 3073-3074.
- [32] R. Criegee, The course of ozonization of unsaturated compounds, *Rec. Chem. Prog* 18 (1957) 111-120.
- [33] L.A. Hull, Hisatsun.Ic, J.P. Heicklen, Low-Temperature Infrared Studies of Simple Alkene-Ozone Reactions, *Abstr Pap Am Chem S*, (1972) 139-&.
- [34] C.K. Kohlmiller, L. Andrews, Infrared-Spectrum of the Primary Ozonide of Ethylene in Solid Xenon, *Journal of the American Chemical Society* 103 (1981) 2578-2583.
- [35] H. Kühne, H.H. Günthard, Spectroscopic study of the ozone-ethylene reaction. Matrix-infrared spectra of three isotopic ethylene ozonides, *The Journal of Physical Chemistry* 80 (1976) 1238-1247.
- [36] M. Hawkins, C.K. Kohlmiller, L. Andrews, Matrix Infrared-Spectra and Photolysis and Pyrolysis of Isotopic Secondary Ozonides of Ethylene, *Journal of Physical Chemistry* 86 (1982) 3154-3166.
- [37] P.S. Bailey, J.A. Thompson, B.A. Shoulders, Structure of the initial ozone-olefin adduct, *Journal of the American Chemical Society* 88 (1966) 4098-4099.
- [38] H.E. O'Neal, C. Blumstein, A new mechanism for gas phase ozone-olefin reactions, *Int J Chem Kinet* 5 (1973) 397-413.
- [39] L.B. Harding, W.A. Goddard III, Mechanisms of gas-phase and liquid-phase ozonolysis, *Journal of the American Chemical Society* 100 (1978) 7180-7188.

- [40] M. Pfeifle, Y.T. Ma, A.W. Jasper, L.B. Harding, W.L. Hase, S.J. Klippenstein, Nascent energy distribution of the Criegee intermediate CH₂OO from direct dynamics calculations of primary ozonide dissociation, *J Chem Phys* 148 (2018).
- [41] J.M. Anglada, R. Crehuet, J.M. Bofill, The Ozonolysis of Ethylene: A Theoretical Study of the Gas - Phase Reaction Mechanism, *Chemistry - A European Journal* 5 (1999) 1809-1822.
- [42] T.L. Nguyen, H. Lee, D.A. Matthews, M.C. McCarthy, J.F. Stanton, Stabilization of the simplest Criegee intermediate from the reaction between ozone and ethylene: A high-level quantum chemical and kinetic analysis of ozonolysis, *The Journal of Physical Chemistry A* 119 (2015) 5524-5533.
- [43] M.F. Hendrickx, C. Vinckier, 1, 3-Cycloaddition of ozone to ethylene, benzene, and phenol: a comparative ab initio study, *The Journal of Physical Chemistry A* 107 (2003) 7574-7580.
- [44] R. Gutbrod, R.N. Schindler, E. Kraka, D. Cremer, Formation of OH radicals in the gas phase ozonolysis of alkenes: the unexpected role of carbonyl oxides, *Chemical Physics Letters* 252 (1996) 221-229.
- [45] R.I. Martinez, R.E. Huie, J.T. Herron, Mass spectrometric detection of dioxirane, H₂COO, and its decomposition products, H₂ and CO, from the reaction of ozone with ethylene, *Chemical Physics Letters* 51 (1977) 457-459.
- [46] F. Lovas, R. Suenram, Identification of dioxirane (H₂COO) in ozone-olefin reactions via microwave spectroscopy, *Chemical Physics Letters* 51 (1977) 453-456.
- [47] K.E. Leather, M.R. McGillen, M.C. Cooke, S.R. Utembe, A.T. Archibald, M.E. Jenkin, R.G. Derwent, D.E. Shallcross, C.J. Percival, Acid-yield measurements of the gas-phase ozonolysis of ethene as a function of humidity using Chemical Ionisation Mass Spectrometry (CIMS), *Atmospheric Chemistry and Physics* 12 (2012) 469-479.
- [48] M.S. Alam, M. Camredon, A.R. Rickard, T. Carr, K.P. Wyche, K.E. Hornsby, P.S. Monks, W.J. Bloss, Total radical yields from tropospheric ethene ozonolysis, *Physical Chemistry Chemical Physics* 13 (2011) 11002-11015.
- [49] S.E. Paulson, J.D. Fenske, A.D. Sen, T.W. Callahan, A novel small-ratio relative-rate technique for measuring OH formation yields from the reactions of O₃ with alkenes in the gas phase, and its application to the reactions of ethene and propene, *The Journal of Physical Chemistry A* 103 (1999) 2050-2059.
- [50] R. Atkinson, S.M. Aschmann, J. Arey, B. Shorees, Formation of OH radicals in the gas phase reactions of O₃ with a series of terpenes, *Journal of Geophysical Research: Atmospheres* 97 (1992) 6065-6073.

- [51] D. Mihelcic, M. Heitlinger, D. Kley, P. Müsgen, A. Volz-Thomas, Formation of hydroxyl and hydroperoxy radicals in the gas-phase ozonolysis of ethene, *Chemical Physics Letters* 301 (1999) 559-564.
- [52] J.M. Beames, F. Liu, L. Lu, M.I. Lester, Ultraviolet Spectrum and Photochemistry of the Simplest Criegee Intermediate CH₂OO, *Journal of the American Chemical Society* 134 (2012) 20045-20048.
- [53] O. Welz, J.D. Savee, D.L. Osborn, S.S. Vasu, C.J. Percival, D.E. Shallcross, C.A. Taatjes, Direct kinetic measurements of Criegee intermediate (CH₂OO) formed by reaction of CH₂I with O₂, *Science* 335 (2012) 204-207.
- [54] C.C. Womack, M.-A. Martin-Drumel, G.G. Brown, R.W. Field, M.C. McCarthy, Observation of the simplest Criegee intermediate CH₂OO in the gas-phase ozonolysis of ethylene, *Science advances* 1 (2015) e1400105.
- [55] T. Berndt, H. Herrmann, T. Kurtén, Direct probing of Criegee intermediates from gas-phase ozonolysis using chemical ionization mass spectrometry, *Journal of the American Chemical Society* 139 (2017) 13387-13392.
- [56] C.A. Taatjes, Criegee Intermediates: What Direct Production and Detection Can Teach Us About Reactions of Carbonyl Oxides, *Annu Rev Phys Chem* 68 (2017) 183-207.
- [57] D.L. Osborn, C.A. Taatjes, The physical chemistry of Criegee intermediates in the gas phase, *Int Rev Phys Chem* 34 (2015) 309-360.
- [58] P. Neeb, O. Horie, G.K. Moortgat, Gas - phase ozonolysis of ethene in the presence of hydroxylic compounds, *Int J Chem Kinet* 28 (1996) 721-730.
- [59] P. Neeb, O. Horie, G.K. Moortgat, The ethene– ozone reaction in the gas phase, *The Journal of Physical Chemistry A* 102 (1998) 6778-6785.
- [60] F. Su, J.G. Calvert, J.H. Shaw, A FT IR spectroscopic study of the ozone-ethene reaction mechanism in oxygen-rich mixtures, *The Journal of Physical Chemistry* 84 (1980) 239-246.
- [61] S. Hatakeyama, H. Kobayashi, H. Akimoto, Gas-phase oxidation of sulfur dioxide in the ozone-olefin reactions, *The Journal of Physical Chemistry* 88 (1984) 4736-4739.
- [62] O. Horie, G. Moortgat, Decomposition pathways of the excited Criegee intermediates in the ozonolysis of simple alkenes, *Atmospheric Environment. Part A. General Topics* 25 (1991) 1881-1896.
- [63] R. Ponec, G. Yuzhakov, Y. Haas, U. Samuni, Theoretical analysis of the stereoselectivity in the ozonolysis of olefins. Evidence for a modified criegee mechanism, *The Journal of organic chemistry* 62 (1997) 2757-2762.

- [64] H. Niki, P. Maker, C. Savage, L. Breitenbach, A FT IR study of a transitory product in the gas-phase ozone-ethylene reaction, *The Journal of Physical Chemistry* 85 (1981) 1024-1027.
- [65] A.C. Rousso, N. Hansen, A.W. Jasper, Y. Ju, Low-Temperature Oxidation of Ethylene by Ozone in a Jet-Stirred Reactor, *The Journal of Physical Chemistry A* 122 (2018) 8674-8685.
- [66] A. Rousso, N. Hansen, A. Jasper, Y. Ju, Identification of the Criegee intermediate reaction network in ethylene ozonolysis: Impact on energy conversion strategies and atmospheric chemistry, *Physical Chemistry Chemical Physics*, (2019).
- [67] X. Shen, X. Yang, J. Santner, J. Sun, Y. Ju, Experimental and kinetic studies of acetylene flames at elevated pressures, *Proceedings of the Combustion Institute* 35 (2015) 721-728.
- [68] H. Zhao, J. Fu, F.M. Haas, Y. Ju, Effect of prompt dissociation of formyl radical on 1, 3, 5-trioxane and CH₂O laminar flame speeds with CO₂ dilution at elevated pressure, *Combustion and Flame* 183 (2017) 253-260.
- [69] G.P. Smith, D.M. Golden, M. Frenklach, N.W. Moriarty, B. Eiteneer, M. Goldenberg, C.T. Bowman, R.K. Hanson, S. Song, W. Gardiner Jr, GRI-Mech 3.0, 1999, URL http://www.me.berkeley.edu/gri_mech, (2011).
- [70] H. Wang, X. You, A.V. Joshi, S.G. Davis, A. Laskin, F. Egolfopoulos, C.K. Law, USC Mech Version II. High-Temperature Combustion Reaction Model of H₂/CO/C₁-C₄ Compounds, (2007).
- [71] F.L. Dryer, F.M. Haas, J. Santner, T.I. Farouk, M. Chaos, Interpreting chemical kinetics from complex reaction–advection–diffusion systems: Modeling of flow reactors and related experiments, *Progress in energy and combustion science* 44 (2014) 19-39.
- [72] I. ANSYS, ANSYS fluent user's guide, release 19.0, Equation, (2018).
- [73] V. Gorshelev, A. Serdyuchenko, M. Weber, W. Chehade, J.P. Burrows, High spectral resolution ozone absorption cross-sections – Part 1: Measurements, data analysis and comparison with previous measurements around 293 K, *Atmos. Meas. Tech.* 7 (2014) 609-624.
- [74] K. Chance, J. Orphal, Revised ultraviolet absorption cross sections of H₂CO for the HITRAN database, *Journal of Quantitative Spectroscopy and Radiative Transfer* 112 (2011) 1509-1510.
- [75] J.B. Jeffries, C. Schulz, D.W. Mattison, M.A. Oehlschlaeger, W.G. Bessler, T. Lee, D.F. Davidson, R.K. Hanson, UV absorption of CO₂ for temperature diagnostics of hydrocarbon combustion applications, *Proceedings of the Combustion Institute* 30 (2005) 1591-1599.

- [76] J.A. Schmidt, M.S. Johnson, R. Schinke, Carbon dioxide photolysis from 150 to 210 nm: Singlet and triplet channel dynamics, UV-spectrum, and isotope effects, *Proceedings of the National Academy of Sciences* 110 (2013) 17691.
- [77] Z. Zhou, X. Du, J. Yang, Y. Wang, C. Li, S. Wei, L. Du, Y. Li, F. Qi, Q. Wang, The vacuum ultraviolet beamline/endstations at NSRL dedicated to combustion research, *Journal of synchrotron radiation* 23 (2016) 1035-1045.
- [78] Ö. Savas, S. Gollahalli, Stability of lifted laminar round gas-jet flame, *Journal of Fluid Mechanics* 165 (1986) 297-318.
- [79] S. Chung, B. Lee, On the characteristics of laminar lifted flames in a nonpremixed jet, *Combustion and Flame* 86 (1991) 62-72.
- [80] B. Lee, S. Chung, Stabilization of lifted tribrachial flames in a laminar nonpremixed jet, *Combustion and Flame* 109 (1997) 163-172.
- [81] Y.-C. Chen, R.W. Bilger, Stabilization mechanisms of lifted laminar flames in axisymmetric jet flows, *Combustion and Flame* 122 (2000) 377-399.
- [82] S. Ghosal, L. Vervisch, Stability diagram for lift-off and blowout of a round jet laminar diffusion flame, *Combustion and Flame* 124 (2001) 646-655.
- [83] S. Chung, Stabilization, propagation and instability of tribrachial triple flames, *Proceedings of the Combustion Institute* 31 (2007) 877-892.
- [84] J. Boulanger, L. Vervisch, J. Reveillon, S. Ghosal, Effects of heat release in laminar diffusion flames lifted on round jets, *Combustion & Flame* 134 (2017) 355-368.
- [85] T. Ombrello, S.H. Won, Y. Ju, S. Williams, Flame propagation enhancement by plasma excitation of oxygen. Part II: Effects of O₂(a¹Δg), *Combustion and Flame* 157 (2010) 1916-1928.
- [86] J.D. McClurkin, D.E. Maier, K.E. Ileleji, Half-life time of ozone as a function of air movement and conditions in a sealed container, *Journal of Stored Products Research* 55 (2013) 41-47.
- [87] W.B. DeMore, S.P. Sander, D. Golden, R.F. Hampson, M.J. Kurylo, C.J. Howard, A. Ravishankara, C. Kolb, M. Molina, *Chemical Kinetics and Photochemical Data for Use in Stratospheric Modeling*. Evaluation No. 12, (1997).
- [88] R. Atkinson, D. Baulch, R. Cox, R. Hampson Jr, J. Kerr, M. Rossi, J. Troe, Evaluated kinetic, photochemical and heterogeneous data for atmospheric chemistry: Supplement V. IUPAC Subcommittee on Gas Kinetic Data Evaluation for Atmospheric Chemistry, *Journal of Physical and Chemical Reference Data* 26 (1997) 521-1011.

- [89] J. Treacy, M.E. Hag, D. O'Farrell, H. Sidebottom, Reactions of ozone with unsaturated organic compounds, *Berichte der Bunsengesellschaft für physikalische Chemie* 96 (1992) 422-427.
- [90] A. Bahta, R. Simonaitis, J. Heicklen, Reactions of ozone with olefins: Ethylene, allene, 1, 3 - butadiene, and trans - 1, 3 - pentadiene, *Int J Chem Kinet* 16 (1984) 1227-1246.
- [91] R. Wegener, T. Brauers, R. Koppmann, S. Rodríguez Bares, F. Rohrer, R. Tillmann, A. Wahner, A. Hansel, A. Wisthaler, Simulation chamber investigation of the reactions of ozone with short - chained alkenes, *Journal of Geophysical Research: Atmospheres* 112 (2007).
- [92] H.T. Wang, Y.J. Zhang, M.U. Yu-Jing, Temperature dependence of the absolute rate constant for the reaction of ozone with dimethyl sulfide, *Journal of Environmental Sciences* 19 (2007) 641-643.
- [93] R. Søndergaard, O.J. Nielsen, M.D. Hurley, T.J. Wallington, R. Singh, Atmospheric chemistry of trans-CF₃CHCHF: Kinetics of the gas-phase reactions with Cl atoms, OH radicals, and O₃, *Chemical Physics Letters* 443 (2007) 199-204.
- [94] R. Atkinson, S.M. Aschmann, D.R. Fitz, A.M. Winer, J.N. Pitts, Rate constants for the gas - phase reactions of O₃ with selected organics at 296 K, *Int J Chem Kinet* 14 (1982) 13-18.
- [95] R. Atkinson, Gas-phase tropospheric chemistry of organic compounds: a review, *Atmospheric Environment* 41 (2007) 200-240.
- [96] W. Thomas, F. Zabel, K. Becker, E. Fink. A mechanistic study on the ozonolysis of ethene. In: editor^editors. *Proceedings of the 1st European Symposium on Physico-Chemical Behaviour of Atmospheric Pollutants; 1993.* p. 207-212.
- [97] T.A. Cool, J. Wang, K. Nakajima, C.A. Taatjes, A. McIlroy, Photoionization cross sections for reaction intermediates in hydrocarbon combustion, *International Journal of Mass Spectrometry* 247 (2005) 18-27.
- [98] B. Albrecht, M. Allan, E. Haselbach, L. Neuhaus, P.A. Carrupt, Molecular-Ions of Transient Species - Vinyl-Alcohol Cation, *Helv Chim Acta* 67 (1984) 216-219.
- [99] J.-F. Müller, Z. Liu, V.S. Nguyen, T. Stavrou, J.N. Harvey, J. Peeters, The reaction of methyl peroxy and hydroxyl radicals as a major source of atmospheric methanol, *Nature communications* 7 (2016) 13213.
- [100] R.L. Caravan, M.A.H. Khan, J. Zador, L. Sheps, I.O. Antonov, B. Rotavera, K. Ramasesha, K. Au, M.W. Chen, D. Rosch, D.L. Osborn, C. Fittschen, C. Schoemaeker, M. Duncianu, A. Grira, S. Dusanter, A. Tomas, C.J. Percival, D.E. Shallcross, C.A. Taatjes, The reaction of hydroxyl and methylperoxy radicals is not a major source of atmospheric methanol, *Nature Communications* 9 (2018).

- [101] T.A. Cool, K. Nakajima, T.A. Mostefaoui, F. Qi, A. McIlroy, P.R. Westmoreland, M.E. Law, L. Poisson, D.S. Peterka, M. Ahmed, Selective detection of isomers with photoionization mass spectrometry for studies of hydrocarbon flame chemistry, *The Journal of chemical physics* 119 (2003) 8356-8365.
- [102] C.A. Taatjes, N. Hansen, A. McIlroy, J.A. Miller, J.P. Senosiain, S.J. Klippenstein, F. Qi, L. Sheng, Y. Zhang, T.A. Cool, Enols are common intermediates in hydrocarbon oxidation, *Science* 308 (2005) 1887-1889.
- [103] R. Zhu, J. Park, M.-C. Lin, Ab initio kinetic study on the low-energy paths of the HO+ C₂H₄ reaction, *Chemical physics letters* 408 (2005) 25-30.
- [104] B. Yang, J. Wang, T.A. Cool, N. Hansen, S. Skeen, D.L. Osborn, Absolute photoionization cross-sections of some combustion intermediates, *International Journal of Mass Spectrometry* 309 (2012) 118-128.
- [105] G. da Silva, J.W. Bozzelli, Role of the α -hydroxyethylperoxy radical in the reactions of acetaldehyde and vinyl alcohol with HO₂, *Chemical Physics Letters* 483 (2009) 25-29.
- [106] H.-B. XIE, Y.-H. DING, C.-C. SUN, Radical-molecule reactions HCO/HOC+ C₂H₄: a mechanistic study, *Journal of Theoretical and Computational Chemistry* 4 (2005) 1029-1055.
- [107] N. Genossar, J.P. Porterfield, J.H. Baraban, Decomposition of the simplest ketohydroperoxide in the ozonolysis of ethylene, *Physical Chemistry Chemical Physics* 22 (2020) 16949-16955.
- [108] H. Niki, P.D. Maker, C.M. Savage, L.P. Breitenbach, Fourier-Transform Infrared Studies of the Self-Reaction of CH₃O₂ Radicals, *Journal of Physical Chemistry* 85 (1981) 877-881.
- [109] F. Battin-Leclerc, Detailed chemical kinetic models for the low-temperature combustion of hydrocarbons with application to gasoline and diesel fuel surrogates, *Progress in Energy and Combustion Science* 34 (2008) 440-498.
- [110] J. Zádor, C.A. Taatjes, R.X. Fernandes, Kinetics of elementary reactions in low-temperature autoignition chemistry, *Progress in energy and combustion science* 37 (2011) 371-421.
- [111] Z.D. Wang, O. Herbinet, N. Hansen, F. Battin-Leclerc, Exploring hydroperoxides in combustion: History, recent advances and perspectives, *Progress in Energy and Combustion Science* 73 (2019) 132-181.
- [112] S. Grimme, S. Ehrlich, L. Goerigk, Effect of the damping function in dispersion corrected density functional theory, *J. Comput. Chem.* 32 (2011) 1456-1465.

- [113] S. Grimme, M. Steinmetz, Effects of London dispersion correction in density functional theory on the structures of organic molecules in the gas phase, *Phys. Chem. Chem. Phys.* 15 (2013) 16031-16042.
- [114] C. Riplinger, B. Sandhoefer, A. Hansen, F. Neese, Natural triple excitations in local coupled cluster calculations with pair natural orbitals, *J. Chem. Phys.* 139 (2013) 134101.
- [115] C. Riplinger, F. Neese, An efficient and near linear scaling pair natural orbital based local coupled cluster method, *J. Chem. Phys.* 138 (2013) 034106.
- [116] D.G. Liakos, F. Neese, Is It Possible To Obtain Coupled Cluster Quality Energies at near Density Functional Theory Cost? Domain-Based Local Pair Natural Orbital Coupled Cluster vs Modern Density Functional Theory, *J. Chem. Theory Comput.* 11 (2015) 4054-4063.
- [117] E. Paulechka, A. Kazakov, Efficient DLPNO-CCSD(T)-Based Estimation of Formation Enthalpies for C-, H-, O-, and N-Containing Closed-Shell Compounds Validated Against Critically Evaluated Experimental Data, *J. Phys. Chem. A* 121 (2017) 4379-4387.
- [118] Y. Minenkov, E. Chermak, L. Cavallo, Accuracy of DLPNO-CCSD(T) method for noncovalent bond dissociation enthalpies from coinage metal cation complexes, *J. Chem. Theory Comput.* 11 (2015) 4664-4676.
- [119] N. Hyttinen, O. Kupiainen-Maatta, M.P. Rissanen, M. Muuronen, M. Ehn, T. Kurten, Modeling the Charging of Highly Oxidized Cyclohexene Ozonolysis Products Using Nitrate-Based Chemical Ionization, *J. Phys. Chem. A* 119 (2015) 6339-6345.
- [120] S. Iyer, F. Lopez-Hilfiker, B.H. Lee, J.A. Thornton, T. Kurten, Modeling the Detection of Organic and Inorganic Compounds Using Iodide-Based Chemical Ionization, *J. Phys. Chem. A* 120 (2016) 576-587.
- [121] Dereli Busra , Ortuno Manuel A. , C.C. J., Accurate Ionization Energies for Mononuclear Copper Complexes Remain a Challenge for Density Functional Theory, *ChemPhysChem* 19 (2018) 959–966.
- [122] P.M. Mayer, C.J. Parkinson, D.M. Smith, L. Radom, An assessment of theoretical procedures for the calculation of reliable free radical thermochemistry: A recommended new procedure, *J. Chem. Phys.* 108 (1998) 604-615.
- [123] B. Chan, L. Radom, Frequency Scale Factors for Some Double-Hybrid Density Functional Theory Procedures: Accurate Thermochemical Components for High-Level Composite Protocols, *J. Chem. Theory Comput.* 12 (2016) 3774-3780.
- [124] M.J. Frisch, G.W. Trucks, H.B. Schlegel, G.E. Scuseria, M.A. Robb, J.R. Cheeseman, G. Scalmani, V. Barone, B. Mennucci, G.A. Petersson, H. Nakatsuji, M. Caricato, X. Li, H.P. Hratchian, A.F. Izmaylov, J. Bloino, G. Zheng, J.L. Sonnenberg, M. Hada, M. Ehara, K. Toyota, F. Fukuda, J. Hasegawa, M. Ishida, T. Nakajima, Y. Honda,

O. Kitao, H. Nakai, T. Vreven, J.A. Montgomery J.r., J.E. Peralta, F. Ogliaro, M. Bearpark, J.J. Heyd, E. Brothers, K.N. Kudin, V.N. Staroverov, R. Kobayashi, J. Normand, K. Raghavachari, A. Rendell, J.C. Burant, S.S. Iyengar, J. Tomasi, M. Cossi, N. Rega, J.M. Millam, M. Klene, J.E. Knox, J.B. Cross, V. Bakken, C. Adamo, J. Jaramillo, R. Gomperts, R.E. Stratmann, O. Yazyev, A.J. Austin, R. Cammi, C. Pomelli, J.W. Ochterski, R.L. Martin, K. Morokuma, V.G. Zakrzewski, G.A. Voth, P. Salvador, J.J. Dannenberg, S. Dapprich, A.D. Daniels, Ö. Farkas, J.B. Foresman, J.V. Ortiz, J. Cioslowski, D.J. Fox, Gaussian 09, Revision D.01, Gaussian, Inc., Wallingford CT, 2009.

[125] F. Neese, The ORCA program system, *Wiley Interdisciplinary Reviews: Computational Molecular Science* 2 (2012) 73-78.

[126] F. Neese, Software update: the ORCA program system, version 4.0, *Wiley Interdisciplinary Reviews: Computational Molecular Science* 8 (2018) e1327.

[127] G. Meloni, P. Zou, S.J. Klippenstein, M. Ahmed, S.R. Leone, C.A. Taatjes, D.L. Osborn, Energy-resolved photoionization of alkylperoxy radicals and the stability of their cations, *Journal of the American Chemical Society* 128 (2006) 13559-13567.

[128] X. Li, A.W. Jasper, J. Zádor, J.A. Miller, S.J. Klippenstein, Theoretical kinetics of O+ C2H4, *Proceedings of the Combustion Institute* 36 (2017) 219-227.

[129] D. Baulch, C.T. Bowman, C.J. Cobos, R. Cox, T. Just, J. Kerr, M. Pilling, D. Stocker, J. Troe, W. Tsang, Evaluated kinetic data for combustion modeling: supplement II, *Journal of physical and chemical reference data* 34 (2005) 757-1397.

[130] R. Lesclaux, P. Roussel, B. Veyret, C. Pouchan, Gas-phase reactivity of the formyl radical with unsaturated hydrocarbons: an experimental and theoretical study, *Journal of the American Chemical Society* 108 (1986) 3872-3879.

[131] V. Saheb, A. Nazari, The reaction of OH radical with the Criegee intermediate propanone oxide: Theoretical investigations, *Computational and Theoretical Chemistry* 1175 (2020) 112726.

[132] G. Meloni, T.M. Selby, F. Goulay, S.R. Leone, D.L. Osborn, C.A. Taatjes, Photoionization of 1-alkenylperoxy and alkylperoxy radicals and a general rule for the stability of their cations, *Journal of the American Chemical Society* 129 (2007) 14019-14025.

[133] A. Mebel, E. Diau, M.-C. Lin, K. Morokuma, Ab initio and RRKM calculations for multichannel rate constants of the C2H3+ O2 reaction, *Journal of the American Chemical Society* 118 (1996) 9759-9771.

[134] L. Vereecken, J. Peeters, Theoretical investigation of the role of intramolecular hydrogen bonding in β -hydroxyethoxy and β -hydroxyethylperoxy radicals in the tropospheric oxidation of ethene, *The Journal of Physical Chemistry A* 103 (1999) 1768-1775.

- [135] R. Atkinson, Kinetics and mechanisms of the gas-phase reactions of the hydroxyl radical with organic compounds under atmospheric conditions, *Chemical Reviews* 86 (1986) 69-201.
- [136] J. Warnatz, Rate coefficients in the C/H/O system, *Combustion chemistry*, Springer 1984, pp. 197-360.
- [137] R. Atkinson, D.L. Baulch, R.A. Cox, J.N. Crowley, R.F. Hampson, Jr., J.A. Kerr, M.J. Rossi, J. Troe, Summary of Evaluated Kinetic and Photochemical Data for Atmospheric Chemistry, IUPAC Subcommittee on Gas Kinetic Data Evaluation for Atmospheric Chemistry Web Version December 2001 (2001).
- [138] C.C. Schubert, S. Schubert, R.N. Pease, The Oxidation of Lower Paraffin Hydrocarbons. I. Room Temperature Reaction of Methane, Propane, n-Butane and Isobutane with Ozonized Oxygen, *Journal of the American Chemical Society* 78 (1956) 2044-2048.
- [139] L. Vereecken, H. Harder, A. Novelli, The reaction of Criegee intermediates with NO, RO₂, and SO₂, and their fate in the atmosphere, *Physical Chemistry Chemical Physics* 14 (2012) 14682-14695.
- [140] J.M. Anglada, S. Olivella, A. Sole, The reaction of formaldehyde carbonyl oxide with the methyl peroxy radical and its relevance in the chemistry of the atmosphere, *Physical Chemistry Chemical Physics* 15 (2013) 18921-18933.
- [141] B. Wu, M. Hastings, W. Sun, T. Ombrello, C. Carter, Dynamics of laminar ethylene lifted flame with ozone addition, *Proceedings of the Combustion Institute* 38 (2021) 6773-6780.
- [142] X. Gao, S. Yang, W. Sun, A global pathway selection algorithm for the reduction of detailed chemical kinetic mechanisms, *Combustion and Flame* 167 (2016) 238-247.
- [143] R.J. Kee, F.M. Rupley, J.A. Miller, Chemkin-II: A Fortran chemical kinetics package for the analysis of gas-phase chemical kinetics, Sandia National Labs., Livermore, CA (USA), 1989.
- [144] Y. Xue, Y. Ju, Studies on the liftoff properties of dimethyl ether jet diffusion flames, *Combustion science and technology* 178 (2006) 2219-2247.
- [145] L. Landau. New exact solution of the Navier-Stokes equations. In: editor^editors. *Doklady Akad. Nauk SSSR*; 1944. p. 311-314.
- [146] H.B. Squire, The round laminar jet, *The Quarterly Journal of Mechanics and Applied Mathematics* 4 (1951) 321-329.